CONSTRUCTION SETTLEMENT MONITORING AND THERMAL ACTIONS MONITORING OF SUPERTALL STRUCTURES

SU JIAZHAN

Ph.D

The Hong Kong Polytechnic University

2015

The Hong Kong Polytechnic University

Department of Civil and Environmental Engineering

CONSTRUCTION SETTLEMENT MONITORING AND THERMAL ACTIONS MONITORING OF SUPERTALL STRUCTURES

SU Jiazhan

A Thesis Submitted in partial fulfilment of the requirements for the

Degree of **Doctor of Philosophy**

July 2015

CERTIFICATE OF ORIGINALITY

I hereby declare that this thesis is my own work and that, to the best of my knowledge and belief, it reproduces no material previously published or written, nor material that has been accepted for the award of any other degree or diploma, except where due acknowledgement has been made in the text.

________________________ (Signed)

SU Jiazhan (Name of student)

To my family

for their love and support

ABSTRACT

Recent decades many supertall buildings over 600 m have been and are being constructed for serving the needs of society and economic development. Numerical analysis and scaled laboratory experiments have been conducted in structural design. However, the actual external loading and environmental parameters of the supertall structures are different from those employed in the numerical models and laboratory experiments. Moreover, the structural system during the construction can be more critical than the service, because the structural configuration and boundary conditions during the construction stage are significantly different from those during the service stage. The structural performance under the real construction and service conditions has not been fully understood due to the storage of first-hand information, which poses challenges for the safety and serviceability of these structures in the construction and service phases. The sophisticated long-term structural health monitoring systems in the 632 m high Shanghai Tower and the 600 m high Canton Tower serve as the test-beds for this PhD research.

The first part of the thesis proposes an integrated construction settlement monitoring method integrating the Kalman Filtering approach and the finite element forward construction stage analysis, and applies it to the Shanghai Tower. With the Kalman Filtering method, the modeling errors and the measurement noise are filtered out. The updated results consider both the construction load effects and various uncertainties. Consequently, the results are more realistic and accurate for studying the floors' pre-determined height of supertall buildings.

The densely distributed thermal sensors in the Canton Tower are used to monitor the

temperature actions of this supertall structure. Based on the long-term monitoring data of the Canton Tower over seven years from 2008 to 2014 during the construction and service stages of the structure, the temperature difference between the inner and outer tubes, and the temperature difference between different facades of structure are investigated.

The last part of the thesis integrates field monitoring and numerical simulation to study the temperature actions of the Canton Tower, including temperature-induced displacement and stresses. The simulated results are verified through a comparison with the measurements. The temperature model can be used as the reference in design and construction of similar supertall structures in future. Moreover, the results are compared with the typhoon-induced counterparts.

The present study offers the first-hand investigation on the structural settlement during the construction stage and thermal actions during the service stage. It will assist practitioners to better understand the structural performance in the real world. With more such monitoring exercises implemented in more practical high-rise structures, the accumulated experience will improve the relevant design/construction standards.

LIST OF PUBLICATIONS

Journal Papers:

Su, J.Z., Xia, Y., Xu, Y.L., Zhao, X. and Zhang, Q.L., (2014), "Settlement monitoring of a supertall buildings using the Kalman filter technique and forward construction stage analysis", *Advances in Structural Engineering*, **17**(6), 881-893.

Gao, J., **Su, J.Z.**, Xia, Y. and Chen, B.C., (2014), "Experimental study of concrete-filled steel tubular arches with corrugated steel webs", *Advanced Steel Construction*, **10**(1), 99-115.

Su, J.Z., Xia, Y., Chen, L., Zhao, X., Zhang, Q.L., Xu, Y.L., Ding, J.M., Xiong, H.B., Ma, R.J., Lv, X.L. and Chen, A.R., (2013), "Long-term structural performance monitoring system for the Shanghai Tower", *Journal of Civil Structural Health Monitoring*, **3**(1), 49-61.

Gao, J., Chen, B.C. and **Su, J.Z.**, (2012), "Experiment on a concrete filled steel tubular arch with corrugated steel webs subjected to spatial loading", *Applied Mechanics and Materials*, 37-42.

Su, J.Z., Xia, Y., Ni, Y.Q., Zhou, L.R. and Su, C., (2015), "Field monitoring and numerical simulation on thermal actions of a supertall structure", *Structural Control and Health Monitoring*, Under review.

Conference Papers:

Su, J.Z., Xia, Y. and Zhang, P., (2014), "Temperature distribution of a supertall structure based on long-term field monitoring", *Proceeding of the 5th Workshop on Civil Engineering Monitoring and Control for Teachers and Students from Mainland, Hong Kong, Macao and Taiwan Universities*., Xi'an, China, 21-24, August.

Su, J.Z., Xia, Y., Xu, Y.L. and Zhou, X.Q., (2014), "Temperature distribution of Shanghai Tower", *Proceedings of the 6th World Conference on Structural control and Monitoring*, Barcelona, Spain, 15-17, July.

Su, J.Z., Xia, Y. and Xu, Y.L., (2013). "Application of Kalman filtering technique to the construction settlement monitoring of supertall buildings", *Proceedings of the 6th International Conference on Structural Health Monitoring of Intelligent Infrastructure*, Hong Kong, 9-11, December.

Su, J.Z., Xia, Y., Chen, L., Zhao, X., Zhang, Q.L. and Xu, Y.L., (2012), "Performance monitoring of the tallest building in China", *Proceedings of the 4th Asia-Pacific Young Researchers & Graduates Symposium*, Hong Kong, December 4-5, 87-94.

Xia, Y., Weng, S., **Su, J.Z.** and Xu, Y.L., (2011), "Temperature effect on variation of structural frequencies: from laboratory testing to field monitoring", *Proceedings of the 6th International Workshop on Advanced Smart Materials and Smart Structures Technology*, Dalian, China.

Gao, J., **Su, J.Z.** and Chen, B.C., (2010), "Experimental study on in-plane mechanical behaviour of CFST-CSW arch", *Proceedings of the 6th International Conference on Arch Bridges*, Fuzhou, China, 11-13, October.

ACKNOWLEDGMENTS

First and foremost, I would like to express my deepest gratitude to Associate Professor Yong Xia, my supervisor, for his valuable guidance, extensive discussion, patient training and constant encouragement as well as providing me with the unique opportunity to pursue my PhD degree. He has walked me through all the stages in completion of this thesis. I have been impressed by his creative thinking, hard-working, always try-to-be-perfect attitude and high responsibility to students. All of these will keep benefiting my future professional life. It is a great honor to study under his supervision. I wish all of the best for him in life and work.

I would also like to express my sincere gratitude to Chair Professor You-lin Xu, for his kindly support and inspiration on my research, and for his kindly encouragement during my study in HK PolyU.

The financial supports from The Hong Kong Polytechnic University are gratefully acknowledged. Best regards to staff in the university Library, Research Office, Human Resources Office, PolyU Technology and Consultancy Co. Ltd., and General Office of Department of Civil and Environmental Engineering for their kind help.

I want to express my especial thanks to my master supervisor Prof. Bao-chun Chen, and co-supervisor Prof. Qing-xiong Wu of the College of Civil Engineering of Fuzhou University. They recommended and encouraged me to pursue my PhD degree.

I am grateful to all technicians in Tongji University for their kind assistance in the experimental work.

Over the past few years, I benefited from the generosity of many fellow students and staffs. To list them all here would not be possible. I am especially grateful to our group members, Dr. Shun Weng, Lin-ren Zhou, Mr. Peng Zhang, Hai-quan Jing, Wei-li Luo, Ping-he Ni, for their discussions and constructive comments. A very special thank you goes to Dr. Zhi-wei Chen, Liang Hu, Xiao-hua Zhang, Zhao-hui Chen, Chao Li, Qin Huang and Mrs. Shu-qin Ye for their consistent friendship, encouragement, and experience sharing, which have enriched my life in Hong Kong. The cheerful days spent with them will always remind me of happiness and living hopefully. I will always put them on my heart, wish them a bright future.

This dissertation would not have been possible without understanding and great support of my family during the past years.

TABLE OF CONTENTS

Page

LIST OF FIGURES

LIST OF TABLES

LIST OF SYMBOLS

Symbol	Description
Chapter Two	
x, y, z	Cartesian coordinates
T	Temperature
t	Time
k	Isotropic thermal conductivity coefficient of the material
ρ	Density of the material
c	Specific heat of the material
Γ	Boundary surface
n	Normal to the surface
$q(t)$	Boundary heat input or loss per unit area
h	Heat transfer coefficient
h_c	Convection heat transfer coefficient
h_r	Irradiation heat transfer coefficient
T_a	Air temperature
$\max T_a(t)$	Maximum air temperature in a day
$\min T_a(t)$	Minimum air temperature in a day
T_{ave}	Daily average temperature
T_{dif}	Daily temperature difference
T_s	Structural surface temperature
T^*	Equivalent air temperature
v	Wind speed
ε	Emissivity coefficient of the structure surface

N	Day number counted from 1 January
I_{SC}	Extraterrestrial solar constant
t_s	Solar hour of the location
t_{noon}	Baseline solar hour of the location being the time of day when the sun is highest in the sky
t_{bj}	Hour number of Beijing
t_d	Hour difference
L	Longitude (north positive) of the location
ψ	Solar altitude
δ	Solar declination
ω	Solar hour angle
γ_s	Azimuth angle
γ	Surface azimuth angle
β	Surface tilt angle
θ	Solar incidence angle
I_D	Direct radiation energy reaching the earth's surface
I_{i0}	Diffuse solar radiation energy reaching the earth's surface
I_{r0}	Reflected solar radiation energy reaching the earth's surface
I_d	Direct solar radiation on the structural surface
I_i	Diffuse solar radiation on the structural surface
I_r	Reflected solar radiation on the structural surface
q_s	The rate of heat absorbed by the structural surface because of solar radiation
k_a	Ratio of atmospheric pressure to pressure at sea level
t_u	Turbidity factor
m	Air mass factor
r_e	Reflected coefficient of ground

Chapter Four

$X(k)$	Discrete time state at time k
$A(k)$	State transition model
$B(k)$	Control input model
$H(k)$	Measurement model
$U(k)$	Control vector
$Z(k)$	Measurement
$W(k)$	Process error vector
$V(k)$	Measurement noise vector
$R(k)$, $Q(k)$	Noise covariance matric
$\hat{X}(k,k-1)$	Predicted state estimate
$\hat{X}(k,k)$	Posteriori state estimate at time k
$P(k, k-1)$	Predicted estimate covariance matrix
$P(k, k)$	Posteriori error covariance matrix
$\tilde{y}(k)$	Measurement residual
$K(k)$	Kalman gain

Chapter Five

T_{tw}	Air temperature at the tower top
T_{gr}	Air temperature at the ground
a	The slope factor
b	The intercept
T_e	Effective temperature of the component
A	Area of cross-section
A_i	Subarea of cross-section
$\overline{T}_i$	Average temperature of subarea

Chapter Six

σ	Stress
ε	Measured total strain
E	Young's modulus of material
α_T	Thermal coefficient of linear expansion of the material
A_s A_c	Area of steel and concrete
E_s E_c	Young's modulus of steel and concrete
ε_s ε_c	Measured total strain of steel and concrete
α_s α_c	Thermal coefficient of linear expansion of steel and concrete

LIST OF ABBREVIATIONS

CFT	Concrete Filled Tube
DOFs	Degrees of Freedom
FE	Finite Element
GPS	Global Positioning System
RC	Reinforced Concrete
RTK	Real-time Kinematic
SHM	Structural Health Monitoring

CHAPTER ONE

INTRODUCTION

1.1 Background

Numerous supertall buildings have been built across the world in past decades to meet the economic and social needs of communities, especially in Asia. Although numerical analysis and scaled laboratory experiments have been conducted during the design stage, the actual loading and environment of the supertall structures are different from the numerical models and laboratory conditions. Their performance under the real construction and service condition has not been well understood because of the storage of first-hand information, which poses challenges for the safety and serviceability of these structures during the construction and service stages.

The construction stage of a complex supertall building is critical because imperfections during the construction stage lead to additional stress and permanent deformation to the structure in-service (Xia *et al*. 2011a). For supertall structures, the vertical displacement (or settlement) of the foundation and superstructure have been a primary concern of structural safety condition during the construction stage since the structural system, material properties, and loadings are time varying and totally different from those in the service phase (Yang *et al.* 2012). The changing loadings and environmental factors make the construction positioning very difficult and may cause the constructed structure deviate from the design target. Differential deformation of main components in a tall building may also cause structural and non-structural deficiencies.

In the current practice of supertall buildings, to minimize the effect of differential deformation on structural and members, the deformation development is controlled using an empirical value of pre-determined geometric position in the next construction stage, which is predicted via the finite element (FE) construction stage analysis following the real construction sequence (Fan *et al.* 2013). However, the current construction stage analysis neither timely adjusts the geometric position when the actual construction state deviates from the design one, nor considers various uncertainties, such as measurement noise and modeling errors.

Some supertall structures place main components on or outside the curtain wall line. The radiation and daily temperature fluctuation have a significant effect on the overall deflection and stresses of these large-scale structures, as well as structural vibration characteristics, because of the indeterminacy and non-uniform distribution of temperature (Malla *et al.* 1988; Salawu 1997; Xia *et al.* 2011b). For a supertall structure, the temperature-induced daily movement may be similar to or even larger than the typhoon-induced motion (Xia *et al.* 2014). Excessive movement and thermal stresses may cause damage to structures, especially for concrete structures and composite structures (Salawu 1997; Yi *et al.* 2010; Yi *et al.* 2013b). Failure to understand temperature effects may result in false alarms or genuine structural damage going undetected (Giraldo *et al.* 2006; Xia *et al.* 2006). The specification of the structural temperature distribution becomes essential to investigate the structural thermal effects. However, the Chinese national standard (GB 50009-2012 2012) specifies the uniform temperature change only but no clause on difference of temperature between different members. One possible reason is that there is no such real temperature data for tall buildings in China.

The sophisticated long-term structural health monitoring (SHM) systems in the 632 m high Shanghai Tower and the 600 m high Canton Tower serve as the test-beds for this research. They provide researchers an opportunity to gain a comprehensive understanding of the structural performance when subjected to various types of loadings during and after construction.

1.2 Research Objectives

The main objectives of the PhD study are as follows:

(1) To improve the precision of the construction settlement monitoring of supertall buildings. A construction settlement monitoring method combining the Kalman Filtering approach and the FE forward construction stage analysis will be proposed, and then be applied to the 632 m tall Shanghai Tower.

(2) To investigate the temperature distribution of supertall buildings under thermal loading. A series of thermal sensors have been installed on the 600 m tall Canton Tower. The temperature distribution of the structure will be analyzed using the long-term monitoring data over seven years from 2008 to 2014 at both the construction and service stages. The results can be used as the reference for structural design, construction, and safety evaluation of supertall structures.

(3) To investigate the strain/stress and displacement responses under thermal loading. A series of strain sensors have been installed on the Canton Tower to measure the thermal-induced strain/stress of the main structural components. A global positioning system (GPS) was also been installed to monitor the temperature-induced displacement of the building top.

1.3 Thesis Organization

This thesis comprises following seven chapters.

Chapter One introduces the research background and objectives of the study.

Chapter Two presents an extensive literature review on relevant topics. SHM of tall building structures is surveyed first. The transient heat-transfer analysis and the associated thermodynamic models are then briefed, followed by a review of thermal responses of building structures.

Chapter Three describes the structural configuration and SHM systems of two supertall buildings, the 632 m tall Shanghai Tower and the 600 m tall Canton Tower.

The Kalman Filtering technique and the FE forward construction stage analysis are integrated for predicting construction settlement of supertall buildings in Chapter Four. The integrated approach will be applied to the long-term structural performance monitoring of the Shanghai Tower.

In Chapter Five, the temperature distribution of the Canton Tower is studied using the real-time field monitoring data during and after construction. The temperature action on the structure is then investigated in Chapter Six. In particular, the temperature-induced horizontal displacement at the tower top and stresses at different levels are obtained. The results are also compared with those caused by strong typhoons.

The last chapter summarizes the main results of this study. Some recommendations for future research are also provided.

CHAPTER TWO

LITERATURE REVIEW

2.1 Introduction

Many supertall structures over hundreds of meters high have been constructed during recent decades. Those over 600 m tall that have been and are being constructed are listed in Table 2.1. The 828 m tall Burj Khalifa in Dubai, United Arab Emirates, is the tallest structure in the world. In mainland China, the tallest building is currently the Shanghai Tower, with a total height of 632 m, as of May 2015.

With the increasing complexity of modern building structures, the life-cycle safety of these building structures and their structural performance under natural and/or man-made hazards such as typhoons, earthquakes and fires, during construction and service stages are the main concerns of the designer, contractor, and client. The recently developed SHM technology offers an excellent approach to measure the loading environment and responses, and provides real-time information on extreme events that may affect structural serviceability or safety (Aktan *et al.* 2000; Lynch *et al.* 2004; Spencer *et al.* 2004; Sumitro and Wang 2005; Brownjohn and Pan 2008).

The significance of implementing SHM for long-span bridges has been recognized by engineering societies. Numerous case studies and operations of SHM have been successfully and widely applied to bridge structures in Japan, North America, Mainland China and Hong Kong (Pines and Aktan 2002; Wu 2003; Wong 2004; Ko and Ni 2005; Brownjohn 2007; Wong 2007; Ou and Li 2010; Ni *et al.* 2011a). However, residential and commercial structures have gained relatively little attention in comparison, especially for supertall buildings. One major reason is that bridges are invested and administrated by government or public authorities while supertall buildings by private sectors, who may be reluctant to pay investment on research. Nevertheless, the success gained in bridge structures has promoted the applications of the SHM technology to high-rise structures in recent years.

This chapter will focus on the SHM for building structures. The construction monitoring, wind monitoring, seismic monitoring, and overall performance monitoring will be surveyed. The transient heat-transfer analysis and the associated thermodynamic model for obtaining the temperature distribution of a structure will also be reviewed. Temperature-induced responses, containing the strain/stress and displacement responses of building structures will be examined in the final part of the chapter.

Table 2.1 Some supertall structures over 600 m in the world

No.	Building Name	City (Country)	Height (m)	Floors	Completed	Material
1	Burj Khalifa	Dubai (UAE)	828	163	2010	Steel/concrete
2	Canton Tower	Guangzhou (CN)	600	–	2010	Composite
3	Tokyo Sky Tree	Tokyo (JP)	634	–	2012	Steel
4	Makkah Royal Clock Tower Hotel	Mecca (SA)	601	120	2012	Steel/concrete
5	Shanghai Tower	Shanghai (CN)	632	128	2015	Composite
6	Ping'an Finance Center	Shenzhen (CN)	600	118	2016	Composite
7	Wuhan Greenland Center	Wuhan (CN)	606	125	2017	Composite
8	Kingdom Tower	Jeddah (SA)	≥ 1000	167	2018	Concrete

2.2 SHM for Building Structures

2.2.1 Components of SHM System

A typical SHM system usually consists of an in-situ data acquisition by sensors and adequate computational models, regardless of their functions and objectives.

The sensory system is responsible for collecting raw data from various sensors. The monitored parameters can be categorized into three types: loadings (structural temperature, wind pressure, and earthquake), structural responses (settlement, inclination, displacement, strain, and acceleration), and environmental factors (ambient temperature, humidity, solar radiation, air pressure, and corrosion).

For instance, a pioneering SHM practice that integrates in-construction and in-service monitoring have been exercised on the Canton Tower (previously the Guangzhou New TV Tower) of 600 m high, which has more than 800 sensors of 16 types (Ni *et al.* 2008). All these sensors were selected to capture the static and dynamic properties of the structure. The sensors were installed at crucial locations according to the FE analysis results of the partial structures at different construction stages and the entire structure. In addition, the accuracy of the measurement for specific structural responses can be improved by combining multiple types of sensors and data. For example, a video camera, GPS, and total station were deployed to measure the horizontal displacement at the top of the structure at various stages of construction for cross-calibration (Ni *et al.* 2009a). The GPS, accelerometers, and a series of inclinometers were also combined to achieve a reliable measurement of static and dynamic displacement.

The data acquisition and transmission system is indispensable to SHM systems for large-scale structures, and plays a significant role in assuring the quality of the acquired data. It usually consists of several stand-alone sub-stations which are distributed at different locations of the structure to collect signals from surrounding sensors. The real-time data acquired from the sensors are transmitted from the sub-stations to the site monitoring center in either wired or wireless manner.

Some sophisticated long-term SHM systems deployed on long-span bridges and supertall structures contain the data processing and control system and the structural health (or performance) evaluation system (Ni *et al.* 2009b; Wong and Ni 2009; Ni and Wong 2012; Su *et al.* 2013).

The data processing and control system is composed of a high-performance computer system and data processing software, and is devised to control sub-stations for data acquisition and pre-processing, data transmission and filing, and data management and displaying.

The structural health (or performance) evaluation system is composed of a condition evaluation system and a structural performance and safety assessment system. The condition evaluation system is mainly utilized to evaluate the structural condition promptly through comparisons of the static and dynamic measurement data with design parameters, FE model analysis results, and pre-determined threshold values. The functions of the structural performance and safety assessment system include, but are not limited to, construction stage analysis, structural analysis, parameter sensitivity analysis, structural identification, FE model modification, and warning, aiming to provide reliable information regarding the integrity of the structure after the occurrence of extreme events such as strong typhoons and earthquake.

Beyond that, individual SHM system comprises the data management system, and the inspection and maintenance system (Ni *et al.* 2009b). The data management system includes a database system for non-spatial temporal data management and the web-based geographic information system software for spatial data management. The inspection and maintenance system aims to inspect and maintain sensors by a laptop-computer-aided portable system.

Based on the components and functions of the SHM system, the potential benefits of an SHM exercise can be summarized as follows but not limited to (Ko and Ni 2005; Brownjohn and Pan 2008; Ni *et al.* 2008; Xia *et al.* 2011a): (1) validate the theoretical assumptions and parameters used in structural design, analysis and laboratory testing; (2) examine the correctness of the design and design specifications for future similar structures; (3) provide real information of the structures after disasters and extreme events to make cost-effective decisions regarding maintenance and management; (4) improve understanding the structural loading and response mechanisms; (5) inspect safety of the construction activities and ensure the constructed structure satisfy the design requirement as closely as possible; and (6) obtain massive amounts of in situ data for cutting-edge research in structural engineering, such as new structural types and smart material applications. A good designed and operated SHM system can benefit not only the researchers, but also the designers, contractors, and clients of the structures.

Actually, SHM has become a popular research topic and gained tremendously attention in civil engineering community in recent years (Chang *et al.* 2003; Van der Auweraer and Peeters 2003). Nevertheless, there are still many challenges at present to make full use of the above benefits of an SHM system. It requires well-coordinated interdisciplinary research between civil engineering, mechanical engineering, and electrical as well as computer engineering for full adaptation of innovation technologies, which cover related and overlapping subjects of sensing, communication, information presentation and data mining, data management and storage, diagnostic methods, system identification, and so on.

2.2.2 Construction Monitoring of Supertall Buildings

The structural system during the construction can be more critical than the service because the structural configuration and boundary conditions in the construction phase are greatly different from those in the service phase. In addition, the imperfections during the construction stage will lead to additional stress and permanent deformation in the service stage (Xia *et al.* 2011a). Therefore, an accurate real-time construction stage analysis including constructed structural behaviors, external loadings, and environmental parameters needs to be investigated for evaluating structural integrity, serviceability, and reliability.

For supertall structures, the vertical displacement responses (or settlement) of the foundation and superstructure have been a primary concern of structural condition at different construction stages since the structural system, material properties, loads and actions in the construction phase are time varying and totally different from those in the service phase (Yang *et al.* 2012).

The changing loadings and environmental factors make the construction positioning very difficult and may make the constructed structure deviate from the design. Differential shortening of core walls and columns in a tall building can cause structural and non-structural deficiencies (Bast *et al.* 2003; Jayasinghe and Jayasena 2004).

In the current practice of supertall buildings, to minimize the effect of differential settlement on structural and members, the settlement development is controlled using an empirical value of pre-determined height in the next construction stage for making sure the member's elevation meets the design requirements via the FE construction stage analysis following the real construction sequence (Fintel *et al.* 1987; Fan *et al.* 2013).

Construction stage analysis for a supertall building can be classified into forward analysis and backward analysis, according to the analysis sequence. Forward analysis follows the real construction sequence. Backward analysis, however, regards the state of the finally completed structure as the initial state and then eliminates the elements and loads in reverse sequence to the real construction one.

However, accurately predicting the amount of settlement is very difficult due to the idealization of the material properties and the assumptions in the analytical models (Park 2003; Moragaspitiya *et al.* 2010; Park *et al.* 2013). Moreover, the construction stage analysis can neither timely adjust the geometric position accurately when the actual construction state deviates from the design one, nor consider various uncertainties associated with civil structures (including measurement noise and modeling errors). Civil structures, especially concrete structures have significant modeling errors and measurement noise (Aktan *et al.* 2003; Bergmeister *et al.* 2003; Yi *et al.* 2012). These uncertainties should be investigated and taken into consideration in the settlement prediction.

Static and /or dynamic strain monitoring of main structural components is essential for construction of building structures. The measured strain can be transferred into the corresponding stress for assessing the material resistance and the safety margin of the structural components. Strain monitoring of large-scale structures by using electrical strain gauges, vibrating-wire strain gauges, or fiber optical strain sensors has been widely executed.

Fuhr *et al.* (1992) installed fiber optic and conventional sensors embedded into the concrete superstructure of the Stafford Building. The sensors monitored stresses incurred during the construction phase and concrete curing as well as vibration and internal crack.

Xia *et al.* (2011a) analyzed the strain and stress in Canton Tower during the construction stage. The shrinkage and creep models for concrete based on field experiments has been established and compared with American Concrete Institute (ACI) formulae. The measured principal stresses of critical components during a long-distance earthquake, typhoons, and construction activities were compared. Moreover, the stress development of the tower throughout the entire construction stage was investigated through FE numerical analysis and field monitoring.

As part of the long-term SHM system, 224 vibrating-wire strain gauges have been installed on the 245 m tall New Headquarters of Shenzhen Stock Exchange to measure the strain responses of key structural components during the construction (Ye *et al.* 2012). The structure has a 162 × 98 × 24 m suspension at the height of 36 m above the ground. A wireless strain monitoring system by integrating local tethered data acquisition and long-range wireless data transmission was developed for real-time strain monitoring and visualization. The system monitored the demolition process of the temporary scaffolds of the suspension part in real-time, providing a safe, controlled, and efficient construction.

Glisic *et al.* (2013) implemented a large-scale lifetime building monitoring program on a high-rise building in Singapore, and collected ten-year local and global strain data using long-gauge fiber optic sensors from construction, upon completion of each new story and the roof, and after the construction. Long-term behavior of the building throughout every stage of life could be followed and evaluated based on the measured results.

2.2.3 Wind Monitoring of High-rise Buildings

Wind loading is one of critical loads on a tall building located in coastal cities which are frequently subjected to typhoons or hurricanes. Wind pressure fluctuations in the windward and leeward faces due to the fluctuation in wind velocity and its interaction with the building result in along-wind motion of the building. High-rise buildings are prone to large dynamic wind-induced responses due to low natural frequencies and small structural damping. Therefore, wind effect is one major concern in design of high-rise buildings.

Monitoring of high-rise structures under strong winds usually focuses on measuring wind speed and wind direction by anemometers, wind pressure by pressure sensors, and wind-induced structural response by accelerometers. The full-scale monitoring exercises during monsoons and typhoons provide a reliable approach to verify the codes adopted in wind-resistant design of high-rise structures and to validate the wind-tunnel testing results.

Dalgliesh and Rainer (1978) measured the wind-induced movements of the Bank of Commerce Building in Toronto, Canada, as one part of a long-term project to assess the validity of wind tunnel experiments in the design. Littler and Ellis (1990) measured the response of a tall building at Hume Point, London to wind loading. After initiating a five-year full-scale monitoring program on an 800-foot (245.7 m) steel-framed building in Boston (Durgin and Gilbert 1994), an extensive monitoring program continued to collect the wind velocity up to 100 feet above the rooftop, pressures and accelerations at a number of locations (Brown 2003). Abdelrazaq *et al.* (2005) carried out a full-scale monitoring for a 73-storey 264 m high tower located in Seoul, Korea, including strain gages, accelerometers and an anemometer, to compare the in-situ dynamic properties and wind-induced response with the design predictions and to enhance the understanding of composite tall building systems.

In Japan, Ohkuma *et al.* (1991) presented the field measurement results of wind pressure and wind-induced acceleration of an 18-storey building with a height of 68 m, and compared the measurement results with the predicted acceleration. Ohtake *et al.* (1992) and Tamura *et al.* (1996) respectively recorded the wind-induced responses of the 125 m high Chiba Port Tower and the 77.6 m high Tokyo International Airport Tower to investigate the effectiveness of the tuned dampers installed in both towers in reducing the wind-induced responses.

Balendra *et al.* (2003) conducted the full-scale measurement of the wind-induced responses of several typical high-rise buildings in Singapore and recommended an empirical forecast model for vibration periods of these buildings. In addition, the relation between the wind speed and acceleration of the buildings was studied based on the wind tunnel force balance model test and field measurement results.

A long-term monitoring program comprising accelerometers, anemometers and vibrating wire strain gauges was established for the 280 m high 65-storey Republic Plaza in Singapore, to monitor the structural dynamic responses and track structural performance during and after construction (Brownjohn *et al.* 1998). And then, in order to investigate the static and dynamic responses of the building under wind loadings, this monitoring program was updated progressively from 1996 until the system was shut down in 2005. A set of modal parameters of the completed structure were obtained to validate the FE model (Brownjohn and Pan 2001).

The acceleration responses of the 70-storey (370 m high) Bank of China Building in Hong Kong to two strong typhoons were measured (Li *et al.* 2000). The field measurement results were compared with the wind tunnel test counterparts to study wind-induced structural response characteristics.

Similar full-scale measurement of acceleration responses programs have been made on a number of high-rise buildings (tower) in mainland China. Fu *et al.* (2008) installed accelerometers and anemometers on the 80-storey (391 m high) China International Trust and Investment (CITIC) Plaza Tower in Guangzhou to record the wind speed, wind direction and acceleration responses. Li and his colleagues have conducted field measurement of wind effects on the 63-storey (197 m high) Guangdong International Building (Li *et al.* 2004b), the 79-storey (384 m high) Di Wang Tower in Shenzhen (Li *et al.* 2004c), and the 88-storey (421 m high) Jin Mao Building in Shanghai (Li *et al.* 2007b). Based on the field measurement data, the amplitude-dependent damping has been identified and compared with the wind tunnel test results (Li *et al.* 2003; Li *et al.* 2006a; Li and Wu 2007).

The lateral displacement of high-rise structures subjected to strong winds also concerns the designers. However, for a long period, the accurate direct measurement of the lateral displacement is difficult. The displacement is usually obtained by a double integral of acceleration responses (Park *et al.* 2002; Quan *et al.* 2005; Xie and Gu 2009). The main problem is that the method has difficulty in capturing the static or quasi-static displacement of the structure, although baseline correction can be employed.

In contrast, the GPS with real-time kinematic (RTK) technology can measure both static and dynamic displacement responses with a rate of 20 Hz and an accuracy of sub-centimeter to millimeter level. It provides a great opportunity to monitor the displacement of high-rise buildings in real-time under strong winds (Celebi and Sanli 2002; Kijewski-Correa *et al.* 2006a, 2006b; Casciati and Fuggini 2009; Yi and Li 2009; Yi *et al.* 2013a). As early as in 1995, measurement of structural vibrations in the Calgary Tower, Canada, with approximately 160 m above ground level, using GPS receivers in differential mode has been conducted (Lovse *et al.* 1995).

To achieve an accurate measurement, two GPS receivers are usually employed, one located in a stable position as the reference station and the other on the structure to measure its movement. Chen *et al.* (2001) installed two GPS receivers on the 384 m tall Di Wang Building in Shenzhen, China, with one set on the top of the building and the other on a reference station on the ground nearby. The results shown that GPS multi-path errors had to be removed such that GPS can be successfully applied for monitoring structural vibrations.

Ogaja *et al.* (2000, 2001) studied the suitability of using GPS for monitoring the displacement and the frequency of the wind-induced dynamic properties of the 280 m high 66-storey Republic Plaza Building. The study was based on the high precision GPS-RTK technique. The feasibility of applying interdisciplinary and GPS-based methods for the dynamic properties monitoring of high-rise buildings was discussed. The continuous time series of RTK solutions have been analyzed to identify the changes in the movement pattern of this building using a wavelet-based technique (Ogaja *et al.* 2003).

Tamura and Yoshida demonstrated the efficiency of GPS-RTK in measuring the displacement of a 108 m high steel tower and studied the feasibility of hybrid use of FEM analysis and GPS-RTK for detecting the integrity of structures during strong winds (Tamura *et al.* 2002; Yoshida *et al.* 2003).

Breuer *et al.* (2002) has evaluated the ability of GPS to measure small movement of the Stuttgart TV tower and the industrial chimney of Opole power station subject to weak winds. The results demonstrated the advantage of using GPS over conventional monitoring using accelerometers and the displacement of the structure can be measured reliably in real-time with sufficient accuracy (Nickitopoulou *et al.* 2006).

A unique monitoring program was systematically developed by a research team from University of Notre Dame (Kijewski-Correa and Kareem 2003; Kijewski-Correa *et al.* 2005), to monitor the full-scale response of some representative tall building structures and compare their actual performance with the predictions from wind tunnel testing and FE models used in their design. A high precision GPS was employed for tracking static and dynamic displacements of the monitored building, as well as the implementation of information technologies to mine, process and disseminate the collected data (Kijewski-Correa and Pirnia 2007). The initiatives of such research encouraged the use of SHM for civil engineering structures, which expand the existing databases of full-scale dynamic properties of tall buildings to further advance the state-of-the-art in tall building design.

A GPS-based SHM system has been devised for a 242 m high commercial building. Wind speed, wind direction and displacement responses were simultaneously and continuously measured under strong wind conditions. The identified results of the responses agreed well with the computed results by the FE method (Li *et al.* 2007a).

As mentioned above, building displacement measurements against wind loads using GPS have been reported frequently. Park *et al.* (2008) reported a mixed simultaneously measurement approach for serviceability assessment of high-rise buildings against wind loads, in which GPS was used to measure the horizontal displacement and accelerometers to measure the horizontal acceleration. The wind-induced responses of a 66-storey high-rise building subject to the yellow dust storm, including relative lateral displacement, acceleration records, and torsional displacements at the top of building, have been measured by the monitoring system. Based on the field measurement, it has concluded that the complete motion history of a high-rise building can be monitored by GPS.

The high-rise buildings which have been deployed with wind monitoring systems are listed in Table 2.2. Most of the instrumentation systems for strong winds have successfully recorded wind loadings and wind-induced responses of the structures during strong winds. The exercises are useful for verifying the wind tunnel testing and FE analysis results and for understanding dynamic behavior of the buildings.

Table 2.2 Some high-rise buildings (more than 200 m high) instrumented for wind monitoring

Building	Location	Height	Sensors
A commercial building	China	242 m 54-storey	GPS
A steel framed building	Boston, USA	245.7 m 57-storey	Anemometer; Accelerometer; Pressure transducers
Tower Plaza III	Seoul, Korea	264 m 73-storey	Anemometer; Accelerometer
Republic Plaza	Singapore	280 m 65-storey	Anemometer; Accelerometer; GPS; Strain Gauge
Bank of China Building	Hong Kong, China	370 m 70-storey	Anemometer; Accelerometer
Di Wang Tower	Shenzhen, China	384 m 79-storey	Anemometer; Accelerometer; GPS
CITIC Plaza Tower	Guangzhou, China	391 m 80-storey	Anemometer; Accelerometer
Jin Mao Tower	Shanghai, China	421 m 88-storey	Anemometer; Accelerometer

2.2.4 Seismic Monitoring of High-rise Buildings

The main purpose of the seismic monitoring system for high-rise buildings is to enhance the understanding of the behavior and potential for damage of structures under earthquakes, which can be achieved by integrating the measurement of transmitted ground motions and structural responses. The measurement would be compared with the post-earthquake structural performance to evaluate current design and construction practices for minimizing damage to buildings during future earthquakes (Celebi 2002).

Originally, understanding of low-amplitude dynamic response of structures has been assembled by full-scale experiments, with examples drawn mainly from the field of earthquake and wind excitations (Hudson 1977; Jeary and Ellis 1981). However, they were just to know the building response during a typical loading event. In order to understand large amplitude response during the ultimate loading event, a long-term monitoring was required. In California, the California Strong Motion Instrumentation Program has installed ground response stations to about 160 buildings (Huang and Shakal 2001). These stations have modern digital recording and communication system to transmit the recorded data to a central facility within a few minutes after a shaking occurs. The program aims to provide information on ground motions and to improve structure design based on the feedback of structural health subject to these ground motions.

The 1995 Hyogo-Ken Nanbu (Kobe) Earthquake in Japan caused significant motivation of applying SHM to civil and building structures. Japan is prone to earthquakes. The urgent needs in development of sophisticated health monitoring systems were enhanced as tools to minimize costs and time through the knowledge of actual damage status (Mita 1999).

A 31-storey office building located in Tokyo was instrumented with three-axis (one vertical and two lateral directions) accelerometers at the center of the basement to observe earthquake motion. In this building, the seismic responses during more than ten earthquakes of different magnitudes have been recorded since March 1991. The vibration properties of this high-rise building have been investigated using seismic responses (Satake and Yokota 1996).

An integrated system comprising of RTK-GPS and accelerometers has been conducted for assessing full-scale structural responses on a 108 m high steel tower located in Tokyo by exploiting the complementary characteristics of GPS system and accelerometers. The seismic and wind-induced responses of the tower measured from GPS, accelerometer sensors, anemometer, and strain gauge were analyzed (Tamura *et al.* 2002; Li *et al.* 2006b).

An acceleration-based evaluation approach has been implemented to the 60 m tall 14-storey Nikken Sekkei Tokyo Building located in Tokyo to monitor the seismic responses during a number of earthquakes (Qian and Mita 2006). These applications of SHM provided an ideal opportunity for an integrated approach of SHM involving novel sensors, communications, and embedded systems as well as data management and mining (Lynch 2005).

In USA, several tall buildings in the areas where earthquake happens frequently have been installed with seismic instrumentations to record the ground motions and seismic responses for assessing anti-seismic design procedures and inferring seismic damage.

A set of strong-motion-induced acceleration responses has been recorded from the 60-storey Transamerica Building - a landmark of San Francisco, during the Loma Prieta earthquake on 17 October 1989. The building was instrumented with synchronized accelerometers and strong-motion accelerographs deployed throughout the structure and connected to a central recording system. The acquired acceleration records allowed studying the behavior of this unique structure (Celebi and Safak 1991).

Another seismic instrumented building, the 30-storey reinforced concrete (RC) framed Pacific Park Plaza Building located in San Francisco, has been monitored during the same earthquake as well. This building was instrumented with 21 channels of synchronized uniaxial accelerometers that connected to a central recording system. The response characteristics of the building were compared with those from forced and ambient vibration tests (Celebi and Safak 1992; Safak and Celebi 1992).

Other buildings with similar seismic instrument systems include the 47-storey moment resisting framed and eccentrically braced Embarcadero Building in San Francisco, with six digital seismic accelerographs of a total of 18 channels (Celebi 1993), and the 42-storey steel-frame Chevron Building in San Francisco, with a set of 14 accelerometers (Safak 1993).

The UCLA Factor Building, a 15-storey steel moment-resisting frame was instrumented with an embedded 72-channel accelerometer network by the US Geological Survey, following the 1994 Northridge earthquake. The sensor network was deployed throughout the building and was continuously recording building vibrations. It was upgraded by installing state-of-the-art data-logging equipment and fiber-optic network cables to continuously record data via the Internet in real time in December 2003. In February 2005, a 330-foot-deep borehole seismometer was embedded about 160 feet away from the building. The instrumentation provided in and around this building made it one of the most densely permanently instrumented buildings in North America (Skolnik *et al.* 2006; Kohler *et al.* 2007).

In Singapore, a dual-rover GPS was installed and integrated with the existing long-term monitoring system for Republic Plaza in Singapore (Brownjohn 2005; Brownjohn and Pan 2008). One purpose of this monitoring system was to capture ground vibrations caused by large earthquakes occurring at least 400 km from Singapore. The correlation of the time history responses between the recorded ground motions at the building site and the simulated seismic response of the building has been analyzed (Pan *et al.* 2004; Brownjohn and Pan 2009).

In Taiwan, a considerable number of tall buildings have been instrumented with vibration monitoring systems for measuring ground motion and seismic responses. They experienced moderate structural damage during the 1999 Taiwan Chi-Chi earthquake (Lin *et al.* 2005).

Li *et al.* (2004) used the GPS to record seismic movements of a 108 m high steel tower in Tokyo during a magnitude 7.0 earthquake. The GPS receiver on the earth may also be used as a seismometer to observe predominantly horizontal components of surface seismic waves generated by large earthquakes since the GPS satellites are not affected by earthquakes (Larson 2009; Shi *et al.* 2010).

The high-rise buildings which have been deployed with seismic monitoring systems are listed in Table 2.3. The measured seismic response data from the instrumented buildings has been utilized for vibration-based structural condition and integrity assessment.

Table 2.3 Some high-rise buildings instrumented for seismic monitoring

Building	Location	Height	Sensors
Pacific Park Plaza Building	San Francisco, USA	30-storey	Accelerometer
An office building	Tokyo, Japan	31-storey	Accelerometer
Chevron Building	San Francisco, USA	42-storey	Accelerometer
Embarcadero Building	San Francisco, USA	47-storey	Accelerometer
Transamerica Building	San Francisco, USA	60-storey	Accelerometer
Republic Plaza	Singapore	280 m 65-storey	Accelerometer; GPS; Strain Gauge

2.2.5 Overall Performance Monitoring of Supertall Buildings

Several modern supertall buildings of more than 500 m high have been built recently or are being constructed in China and United Arab Emirates. In practice, systematic construction monitoring for supertall structures is still rare, compared with numerous case studies and successful implementation in bridge engineering (Shahawy and Arockiasamy 1996; Sohn *et al.* 2004; Lin *et al.* 2005), although numerical methods have been developed to predict the load distribution of building structures during construction (Stivaros and Halvorsen 1990; Fang *et al.* 2001; Nunez and Boroschek 2010).

Until recently, an extensive SHM program has been executed for understanding the structural and foundation system behaviors of the 828 m tall Burj Khalifa in Dubai, United Arab Emirates, during the construction and service stages (Abdelrazaq 2011). This program was conducted to monitor the strain of vertical elements, the foundation settlement, the wall and column vertical shortening due to elastic, shrinkage and creep effects, as well as the lateral displacement of the tower under the dead load resulting from immediate elastic and long term creep effects in real time during construction.

Choi *et al.* (2013) presented a practical wireless sensing system for monitoring column shortening in high-rise buildings under construction. The proposed system has been applied to the actual 66-storey and 72-storey high-rise residential buildings. This monitoring system successful collected real-time data of the shortening of vertical members using a web-based management program. It enabled the construction managers to collect and investigate monitoring data in real-time, which could facilitate prompt actions to correct the differential shortening in construction and thus result in more precise construction.

Another structural performance monitoring system was designed for Tianjin Goldin Finance 117 Tower which is being constructed in Tianjin, China, with 117-storey approximately 597 m. The aim of this monitoring system is to provide real-time information of structural performance under daily conditions as well as extreme events, and to evaluate structural safety, reliability, durability, and serviceability through comparison of the field collected data with the design parameters (Zhang 2013).

The 600 m tall Canton Tower and 632 m tall Shanghai Tower have been instrumented with an SHM system integrating the in-construction and in-service monitoring, which will be detailed in Chapter Three (Ni *et al.* 2009b; Su *et al.* 2013).

Design and implementation of such an integrated monitoring system have many benefits. For embedment-type sensors, such as embedded strain gauges, temperature sensors and corrosion sensors inside concrete, it is necessary to install them in synchronism with the construction progress. These sensors are able to track the complete historic change in the parameters from the onset of construction and thus achieve life-cycle monitoring of the structure. For example, the integrated monitoring system enables the measurement of cumulative strain rather than dynamic strain, which is necessary for evaluating the real safety index of structural components and the impact of extreme events (such as earthquake, strong winds, fire, man-made disasters) on the structural performance. In addition, the structural FE model can be updated stage by stage using the measured data at different construction stages. The construction accuracy can be improved by extracting the environmental effect and adjusting the newly constructed structural portions.

2.3 Heat Transfer Analysis of Structures

2.3.1 Heat Transfer Equations and Boundary Conditions

Heat conduction in a solid is governed by the Fourier partial differential equation. Temperature T of a point in a structure at any time t can be expressed by a three-dimensional heat flow equation as (Whitaker 1977):

$$k\left(\frac{\partial^2 T}{\partial x^2}+\frac{\partial^2 T}{\partial y^2}+\frac{\partial^2 T}{\partial z^2}\right)=\rho c\frac{\partial T}{\partial t} \tag{2.1}$$

where x, y, and z are Cartesian coordinates, k, ρ, c are the isotropic thermal conductivity coefficient, density and the specific heat of the material, respectively. Equation (2.1) can be simplified into a two-dimensional or even one-dimensional temperature field when variation of the temperature in one or two directions is assumed negligible (Elbadry and Ghali 1983; Fu *et al.* 1990). The corresponding equation becomes

$$k\left(\frac{\partial^2 T}{\partial x^2}+\frac{\partial^2 T}{\partial y^2}\right)=\rho c\frac{\partial T}{\partial t} \tag{2.2}$$

$$k\frac{\partial^2 T}{\partial x^2}=\rho c\frac{\partial T}{\partial t} \tag{2.3}$$

The temperature field of a structure can be obtained by solving the above Fourier partial differential equation under initial and boundary conditions. There are three kinds of thermal boundary conditions commonly encountered in the solution of the partial differential equation (Lienhard and Lienhard 2003):

i) Specified temperatures of the structural boundary

$$T\big|_{\Gamma}=T_{\Gamma} \tag{2.4}$$

where Γ is the boundary surface.

ii) Specified heat flux on the structural boundary

$$k\frac{\partial T}{\partial n}\Big|_{\Gamma}=q(t) \tag{2.5}$$

where n is normal to the surface, and $q(t)$ is the boundary heat input or loss per unit area.

iii) Heat flux is proportional to the temperature difference

$$k\frac{\partial T}{\partial n}|_{\Gamma} = h\left(T_a - T_s\right) \tag{2.6}$$

where h is heat transfer coefficient, T_a is the air temperature, and T_s is the structural surface temperature.

For a structure under solar radiation and ambient thermal environment, the boundary condition for the thermal analysis is a combination of the second and the third kinds:

$$k\frac{\partial T}{\partial n}|_{\Gamma} = q + h\left(T_a - T_s\right) \tag{2.7}$$

2.3.2 Environmental Thermal Condition

For a structure subjected to solar radiation, the thermal energy transferred between the structure surface and environment includes convection q_c, thermal irradiation q_r, and solar radiation q_s (Elbadry and Ghali 1983).

The rate of heat transfer by convection q_c is associated with the movement of the air particles and depends on the temperature difference between the air and the structural surface, this is,

$$q_c = h_c\left(T_a - T_s\right) \tag{2.8}$$

where h_c is the convection heat transfer coefficient, and is related to wind speed, surface roughness, and geometric configuration of the exposed surface (Branco and Mendes 1993; Froli *et al.* 1996). In the heat transfer problem of buildings, it is usually determined experimentally by empirical formulae (Defraeye *et al.* 2010)

$$h_c = \begin{cases} 3.7v + 6.0 & (v < 5.0m/s) \\ 7.15v^{0.78} & (v \geq 5.0m/s) \end{cases} \tag{2.9}$$

where v is the wind speed. Wind speed and wind direction have a significant influence on the convective heat transfer coefficient.

The heat transfer between the structural surface and the surrounding atmosphere due to long wave radiation, i.e. thermal irradiation, can be defined in a quasi-linear form as:

$$q_r = h_r \left(T_a - T_s \right) \tag{2.10}$$

where h_r is the irradiation heat transfer coefficient and depends on the structural material, surface temperature, and air temperature (Kreith 1973; Elbadry and Ghali 1983). For normal air temperature and concrete structural temperature, parameter h_r can be expressed by (Mirambell *et al.* 1991)

$$h_r = \varepsilon \left[4.8 + 0.075 \left(T_a - 5 \right) \right] \tag{2.11}$$

where ε ($0<\varepsilon<1$) is the emissivity coefficient of the structure surface. Once the radiation coefficient h_r and convection coefficient h_c are calculated, the heat flux by convection and thermal irradiation can be combined as an overall heat transfer coefficient

$$h = h_c + h_r \tag{2.12}$$

2.3.3 Solar Radiation

Solar radiation plays an important role for a civil engineering structure exposed in the open environment. This section examines the nature of solar radiation, the geometric relation between the sun and the earth, and the characteristics of the solar radiation reaching the surface of a structure.

2.3.3.1 Astronomical relation

The earth's orbit around the sun is elliptical, and the sun-earth distance varying ±1.7 percent over the course of the year. The extraterrestrial solar radiation at normal incidence can be calculated by the empirical formula (Rohsenow *et al.* 1985)

$$I_{SC} = 1367\left[1 + 0.033\cos\left(360^\circ \frac{N}{365}\right)\right] \tag{2.13}$$

where N is the day number counted from 1 January.

The earth revolves around the sun in an elliptical orbit which is called the ecliptic plane, while the plane containing the earth's equator is called the equatorial plane. The angle between the ecliptic plane and the equatorial plane is 23.45°. The earth-sun vector moves in the ecliptic plane, and the angle between this vector and the equatorial plane is called the solar declination δ. It is positive when the earth-sun vector points northward relative to the equatorial plane. The solar declination is expressed as

$$\delta = -23.45^\circ \cos\left(360^\circ \frac{N+10}{365.25}\right) \tag{2.14}$$

The rotation of the earth about its axis causes the day-night cycle. The sun appears to move 15 degrees per hour. It is convenient to define a solar hour angle ω as

$$\omega = \left(t_{noon} - t_s\right) \cdot 15° \tag{2.15}$$

where t_s is the solar hour of the location; t_{noon} is the baseline solar hour of the location being the time of day when the sun is highest in the sky. The solar hour angle ω is zero at solar noon and positive in the mornings and negative in the afternoon. The solar hour t_s of a location in China is determined based on the hour number of Beijing t_{bj}, the longitude L (north positive) of the concerned location, and the hour difference t_d

$$t_s = t_{bj} - \frac{120^\circ - L}{15^\circ} + t_d \tag{2.16}$$

where

$$t_d = 0.165\, sin\, 2\theta_N - 0.025\, sin\, \theta_N - 0.126\, cos\, \theta_N \tag{2.17}$$

$$\theta_N = 360^\circ \frac{N - 81}{364} \tag{2.18}$$

$$t_{noon} = 12 - \frac{120^\circ - L}{15^\circ} + t_d \tag{2.19}$$

As shown in Figure 2.1, solar altitude ψ is measured from the local horizontal plane and a line to the center of the sun. Azimuth angle γ_s is measured in the horizontal plane between a line to south and the projection of the structure-to-sun line. They can be calculated as the following equations for any time of day, date, and location:

$$sin\psi = sin\, L\, sin\,\delta + cos\, L\, cos\,\delta\, cos\,\omega \tag{2.20}$$

$$sin\,\gamma_s = \frac{cos\,\delta\, sin\,\omega}{cos\,\psi} \tag{2.21}$$

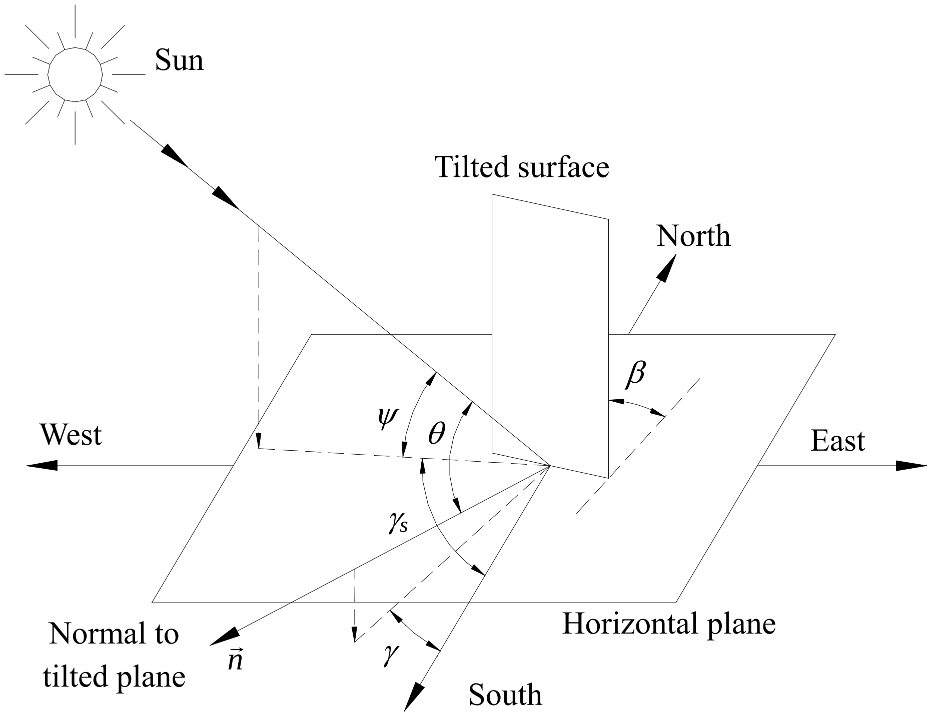

Figure 2.1 Definition of spatial position of sun and structure

The orientation of a tilted surface such as a wall can be specified in terms of surface azimuth angle γ and surface tilt angle β. Vector $\vec{n}$ is normal to the tilted surface. Surface azimuth angle γ is measured from the south with positive toward the west. Tilt angle β at which the surface is inclined from the horizontal is taken positive for the south-facing surface. Solar incidence angle θ is defined as the angle between surface normal $\vec{n}$ and a line collinear with the sun's rays. It is expressed as (See Figure 2.1)

$$\cos\theta = \cos\left(\gamma_s - \gamma\right)\cos\psi \sin\beta + \sin\psi \cos\beta \tag{2.22}$$

If the value of Equation (2.22) is negative, indicating θ > 90°, the sun's rays will not strike the surface. The Equation (2.22) can be expanded as

$$\begin{aligned}\cos\theta = {} & \sin\delta \sin L \cos\beta - \sin\delta \cos L \sin\beta \cos\gamma + \cos\delta \cos L \cos\beta \cos\omega \\ & + \cos\delta \sin L \sin\beta \cos\gamma \cos\omega + \cos\delta \sin\beta \sin\gamma \sin\omega\end{aligned} \tag{2.23}$$

2.3.3.2 Solar radiation

The rate of heat absorbed by the structural surface because of solar radiation, q_s, is

$$q_s = \alpha I \tag{2.24}$$

where I is solar radiation, and α ($0<\alpha<1$) is the absorptivity coefficient of the surface material. The solar radiation is affected by many factors such as the day of the year, the hour of the day, the latitude and the altitude of the structure, and the cloudiness of the sky (Branco *et al.* 1992). I consists of three components

$$I = I_d + I_i + I_r \tag{2.25}$$

where I_d, I_i and I_r are the direct solar radiation, diffuse solar radiation, and reflected solar radiation on the surface, respectively. Their intensities on the ground can be obtained through field measurement or simulated by empirical formulae. I_d, I_i and I_r can be determined by considering the tilt angle of the surface of the structure.

2.3.3.3 Direct solar radiation

The direct radiation depends on the solar constant I_{SC} and the absorption of the solar energy in the atmosphere. Only a fraction of the total solar radiation reaches the surface of the earth since the earth's atmosphere filters off a part of the solar radiation. The direct radiation energy reaching the earth's surface can be obtained by

$$I_D = I_{SC} 0.9^{k_a t_u m} \tag{2.26}$$

where k_a is the ratio of atmospheric pressure to pressure at sea level (See Table 2.4), t_u is the turbidity factor which is used to express the attenuation of radiation in different atmospheric conditions, and m is the air mass factor.

Table 2.4 Ratio of atmospheric pressure to pressure at sea level

Altitude (m)	0	200	400	600	800	1000	1500
k_a	1.0	0.972	0.944	0.918	0.892	0.867	0.84

The air pollution increases substantially the absorption of the solar radiation and thus the turbidity factor can be expressed as

$$t_u = A_{tu} - B_{tu}\, cos\left(360^\circ \frac{N}{365}\right) \tag{2.27}$$

Parameters A_{tu} and B_{tu} for various positions are listed in Table 2.5. The measured turbidity factor varies monthly in Guangzhou and Shanghai China as shown in Table 2.6 (SoDa 2014).

Table 2.5 Turbidity factor

Parameter	City	Village	Mountain Areas	Industrial Areas
A_{tu}	3.7	2.8	2.2	3.8
B_{tu}	0.5	0.6	0.5	0.6

Table 2.6 Turbidity factor in different months

Month	Turbidity Factor (t_u)					
	Guangzhou Altitude (m)			Shanghai Altitude (m)		
	0	250	500	0	250	500
January	3.3	3.2	3.1	2.4	2.3	2.3
February	3.4	3.3	3.2	2.6	2.5	2.5
March	4.2	4.1	4	3.1	3.0	2.9
April	4.5	4.4	4.3	3.4	3.3	3.2
May	5.1	5.0	4.8	4.2	4.1	3.9
June	5.2	5.0	4.9	4.4	4.2	4.1
July	5.3	5.2	5.0	4.8	4.6	4.5
August	5.2	5.0	4.9	4.6	4.5	4.4
September	4.6	4.5	4.3	4.1	4.0	3.8
October	4.2	4.1	4.0	3.3	3.2	3.1
November	3.6	3.5	3.4	2.9	2.8	2.7
December	3.7	3.6	3.5	2.4	2.3	2.3
Year	4.4	4.2	4.1	3.5	3.4	3.3

The air mass factor gives the relative path length of the radiation through the atmosphere, which is expressed as

$$m = \frac{1}{sin\psi} \tag{2.28}$$

The rate of the direct solar radiation upon a surface normal to the sunrays can be written as

$$I_d = I_D\, cos\,\theta = I_{SC}\, 0.9^{k_a t_u m}\, cos\,\theta \tag{2.29}$$

2.3.3.4 Diffuse solar radiation

The diffuse solar radiation describes the sunlight that is scattered or remitted by molecules and particles in the atmosphere, and still reaches the surface of the earth. It can be estimated as (Sekihara 1985)

$$I_{i0} = \frac{1}{2} \cdot \frac{1-P^m}{1-1.4\, ln\, P} I_{SC}\, sin\psi \tag{2.30}$$

where

$$P = 0.9^{k_a t_u} \tag{2.31}$$

The diffuse solar radiation on a surface with tilt angle β becomes

$$I_i = \frac{1+cos\,\beta}{2} I_{i0} \tag{2.32}$$

2.3.3.5 Reflected solar radiation

The direct and diffuse solar radiation can be reflected onto a structure surface from nearby ground or adjacent construction. This part is called as the reflected solar radiation

$$I_{r0} = r_e\left(I_d + I_{i0}\right) \tag{2.33}$$

where r_e is the reflected coefficient of ground and is usually set as 0.2 for common earth surface and 0.7 for snow covered surface.

The reflected solar radiation on a surface with a tilt angle β is

$$I_r = \frac{1-cos\,\beta}{2} I_{r0} \tag{2.34}$$

2.3.3.6 Diurnal temperature variation

For the numerical analysis of structural temperature field, the daily variation of the ambient temperature can be measured continuously and expressed as a function of the time of day

$$T_a = f\left(t\right) \tag{2.35}$$

If only the maximum and minimum temperature in a day, instead of the entire history of ambient temperature, are recorded, it is customary to assume a sinusoidal variation between the minimum temperature assumed to occur at 3:00 and the maximum value at 15:00. Consequently, the temperature at any hour, t^*, of the day can be expressed by the function

$$T_a = T_{ave} + T_{dif} \cdot \sin\left[\frac{\pi}{12}\left(t^* - 9\right)\right] \tag{2.36}$$

where

$$T_{ave} = \frac{1}{2}\left[\max T_a(t) + \min T_a(t)\right] \tag{2.37}$$

$$T_{dif} = \frac{1}{2}\left[\max T_a(t) - \min T_a(t)\right] \tag{2.38}$$

2.3.4 Integration of Boundary Conditions

From Equations (2.8), (2.10) and (2.24), the heat flux on a boundary surface is represented by

$$k\frac{\partial T}{\partial n}\Big|_{\Gamma} = \alpha I + h\left(T_a - T_s\right) \tag{2.39}$$

Equation (2.39) can be rewritten as

$$k\frac{\partial T}{\partial n}\Big|_{\Gamma} = h\left(T^* - T_s\right) \tag{2.40}$$

where

$$T^* = T_a + \frac{\alpha I}{h} \tag{2.41}$$

where temperature T^* is termed "equivalent air temperature" that accounts for both the effect of air temperature and solar radiation.

The thermal field model based on the above equations has been developed to estimate the time-dependent temperature throughout the entire structure. In the last decades, extensive studies have been conducted on temperature distribution and thermal effects on various types of bridges (Zuk 1965; Priestley 1976; Dilger *et al.* 1981; Tong *et al.* 2001; Ni *et al.* 2007; Xia *et al.* 2013). In contrast, only few investigations have been devoted to tall buildings due to the specificity of the construction site and various restrictions that hinder long-term monitoring.

2.4 Temperature-induced Responses of Building Structures

Civil structures are subject to daily, seasonal, and yearly environmental thermal effects induced by solar radiation and ambient air temperature. Since the thermal conductivity of structural component is dependent on material characteristics, the structural members that consist of different materials experience different temperature distribution. Moreover, if the part of members expose to the sunlight and the rest parts expose to the shade, even though the members have the same material, they will also have different temperature distributions.

It is widely recognized that the radiation and daily temperature fluctuation have a significant influence on the overall deflection and stresses of high-rise structures and long-span bridges, as well as structural vibration characteristics, because of the indeterminacy and non-uniform distribution of temperature (Kennedy and Soliman 1987; Malla *et al.* 1988; Smith and Coull 1991; Salawu 1997; Xia *et al.* 2011b).

As temperature change may cause damage to concrete structures and composite structures, attention has been given to thermal responses of structures for a relatively long time. In the early stage, there were very few data of temperatures and thermal responses for structures, researchers mainly predicted the responses through numerical techniques. Among these, temperature effects on tall steel framed buildings have been analyzed since the 1970s (Khan and Nassetta 1970; McLaughlin

1970; West and Kar 1970). The proposed general equations permit the calculation of column temperature under the influence of any combination of indoor and outdoor temperatures. The analysis method for determining the member forces and joint displacements that result in steel frames from specified temperature changes in the exterior columns has been developed. A number of significant design considerations for temperature effects on tall buildings have been discussed.

In Eurocode 1 (European Committee for Standardization 2003), the temperature distribution within an individual structural element is divided into four essential components (Figure 2.2), that is, (a) a uniform temperature component ΔT_u, given by the difference between the average temperature of an element and its initial temperature; (b) two linearly varying temperature difference components about the z–z axis ΔT_{My} and about the y–y axis ΔT_{Mz}, which given by the difference between the temperatures on the outer and inner surfaces of a cross section, or on the surfaces of individual layers; and (c) a non-linear component ΔT_{E}. This non-linear temperature difference component results in a system of self-equilibrated stresses which produce no net load effect on the structure element. For different parts of a structure, their temperature difference is given by the difference of average temperatures of these parts.

However, Chinese national standard GB 50009 (GB 50009 2012) specifies the uniform temperature change only but has no clause on difference of temperature between different members. One possible reason is that there has no such real temperature data in China.

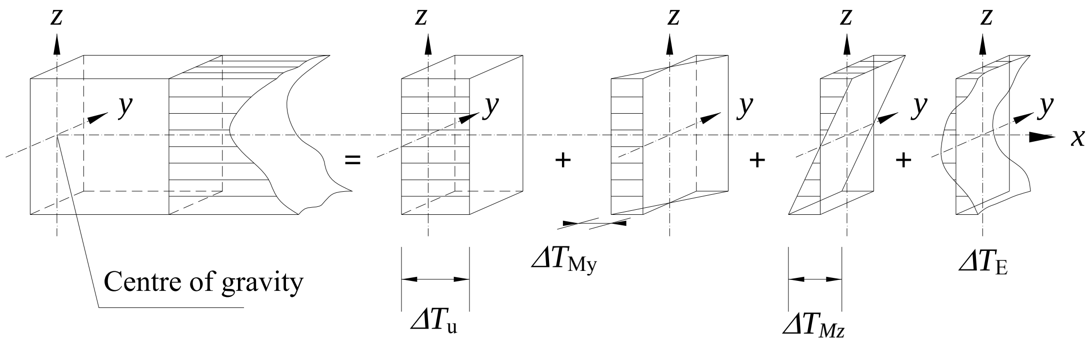

Figure 2.2 Diagrammatic representation of constituent components of a temperature profile

With the development of the SHM technology, temperature distribution and temperature-induced responses of structures have been monitored. Through the real-time temperature data and structural responses such as deformation, strain and stress obtained, the structural thermal behaviors have been understood better.

Pirner and Fischer (1999) made long-term observations of wind and temperature effects on a 198 m high TV tower that has already been in service for nearly 30 years, and applied available data to determine the service life of the antennae tower and mast. The verification of the service life of the TV tower has revealed that the stresses due to temperature changes, which were non-uniform along the circumference of the cross-section of the tower, were not negligible.

Tamura *et al.* (2002) employed a RTK-GPS measurement system to measure the deformation of a 108 m high steel tower on a fine weather day. The measurement results indicated that the top of the tower did not move until sunrise, and then to northwest direction by about 4 cm in daytime and returned to original point after sunset finally.

Seco *et al.* (2007) monitored a 30 m tall concrete building continuously to quantify statistically the relation between the environmental conditions and the building movement. The observed displacement agreed with the expected one as a function of the movement of the sun throughout the day.

Nayeri *et al.* (2008) installed a dense array of 72-channel accelerometers permanently on a 17-storey steel frame building and analyzed 50 days of recorded data. The variability of the estimated parameters due to temperature fluctuations was investigated. A strong correlation between the frequency and the air temperature was observed while the frequency variation lagged behind the temperature variation by a few hours.

Jin *et al.* (2008) studied the effect of non-uniform temperature field under sunshine on the structure supporting the reflector of the five-hundred-meter aperture spherical telescope. The results indicated that the temperature field under sunshine was quite non-uniform, with the highest local temperature difference of 11℃, which significantly influenced the fitting accuracy of the reflector shape.

Breuer *et al.* (2008) and Breuer (2010) investigated the temperature distribution of the Stuttgart TV Tower (with 212 m high) and measured the displacements caused by the combined influence of solar radiation and daily air temperature variation during different weather seasons and conditions. The temperature distribution on the external surface of the TV shaft varied with environmental conditions. The path of the tower top described an ellipse related to the position of the sun during a sunny day.

Li et al. (2009) measured the frequency variation of the Chinese National Aquatics Center, a steel spatial structure with 177 m long and 177 m wide. The temperature-induced internal force and non-uniform temperature might result in the frequency changes.

Yuen and Kuok (2010) employed the Bayesian approach to identify the modal frequencies of a 22-storey RC building for one year with the ambient vibration data. They found that explicit consideration of the ambient temperature and relative humidity is essential for long-term SHM.

An efficient temperature and displacement monitoring system has been instrumented for Shenzhen Bay Stadium during the construction phase (Teng *et al.* 2014). Thermal sensors were installed at different locations for assessing the effects of radiation on the local temperature. A total station was utilized for measuring the structural displacement during the closure phase. This structural construction monitoring system played an important role in providing scientific reference information for easier, faster and safer decision making during construction, and enhanced the safety and construction accuracy of this structure.

A small number of research works have focused on temperature effects on tall structures at the construction stage. Azkune *et al.* (2007) evaluated the influence of ambient temperature changes on the load distribution between columns and slabs of high-rise structures under construction. It was concluded that temperature variation was the determinant factor in load redistribution between any two consecutive construction steps.

Zheng *et al.* (2011) adopted an FE model to analyze the temperature difference of the Shanghai Tower. The results showed that the effect of the sunshine temperature difference on the structure was significant.

Temperature sensors were installed on an 18-floor building during the construction stage for investigating the temperature lagging between inside and outside of the concrete (Li *et al.* 2012).

Nevertheless, field study of temperature on supertall structures over 300 m is still very rare. To the best of the author's knowledge, the temperature distribution of supertall structures has not been investigated through field measurement. Moreover, in some large-scale structures especially the supertall buildings, the temperature of each differently oriented member may vary at different time because of their large size and complicated configuration. It is very difficult to establish thermal FE models to predict the detailed temperature distribution over the entire structure. The effect of temperature on structural behavior has not been fully understood.

Hundreds of temperature sensors have been installed on the 600 m tall Canton Tower, as a part of the long-term SHM system of the tube-in-tube structure (Ni *et al.* 2011b; Zhang *et al.* 2012). These provide a good opportunity for monitoring structural temperature during both the construction and service stages. The temperature distribution of the structure and its thermal-induced responses will be studied and presented in Chapters Five and Six, respectively.

2.5 Summary

This chapter reviews the applications of SHM to building structures, including the components of an SHM system, construction monitoring of supertall buildings, wind and seismic monitoring of high-rise buildings, and the overall performance monitoring of supertall buildings.

It has been demonstrated that long-term field monitoring systems deployed on high-rise structures and supertall buildings are very helpful to monitor the structural responses and to assess the structural performance during extreme events. Therefore, long-term SHM systems are highly recommended for modern supertall buildings with great height and complicated configuration.

In order to investigate the thermal actions on supertall buildings under thermal loading, the transient heat-transfer analysis and the associated thermal boundary conditions, are reviewed in this chapter, followed by a review of temperature-induced responses of building structures containing the strain/stress and displacement responses.

CHAPTER THREE

TWO SUPERTALL TEST-BEDS OF STRUCTURAL HEALTH MONITORING

3.1 Introduction

As described in Chapter Two, successful experience gained by practice and research have promoted the applications of the SHM technology from long-span bridges to high-rise structures. Majority of current supertall SHM systems has been aimed to improve understanding of loading environment and dynamic response mechanisms for strong winds and seismic ground motion. Complete systematic monitoring of supertall structures under various loading is limited. Shanghai Tower and Canton Tower are two test-beds equipped with comprehensive SHM systems.

This chapter will describe the structural systems and the SHM systems of the two highest supertall structures in China. The practical monitoring exercise provides the designer, the contractor, and the researcher with valuable real-time data in terms of structural performance.

3.2 Shanghai Tower

3.2.1 Structure System

The Shanghai Tower, nearby the 421 m tall Jin Mao Tower and the 492 m tall Shanghai World Financial Center, is the tallest structure in China and second in the world, with a structural height of 580 m and an architectural height of 632 m (see

Figure 3.1(a)). The structural construction started from November 2008 and completed in 2014. It will be put into operation in 2015.

(a) Perspective view

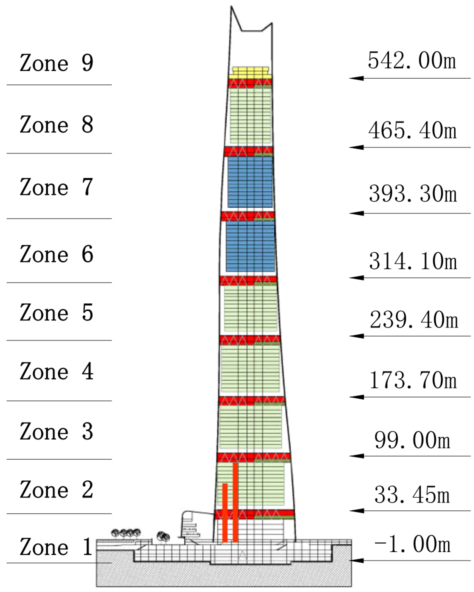

(b) Strengthening floors

Figure 3.1 Shanghai Tower

A triangular outer façade encloses the entire structure, which gradually shrinks and twists clockwise about 120° along the height of the building. The building is divided into 9 zones along the height separated by 8 independent strengthening floors as shown in Figure 3.1(b). It will serve for multi-functions, such as office space, entertainment, hotel, sky-gardens, as well as various retail and cultural functions (Ding *et al.* 2010).

The Shanghai Tower adopts the mega-frame-core-wall structural system, which comprises a core wall inner tube, an outer mega frame, and a total of 6 levels of outriggers connecting them (Figure 3.2). The outriggers are set at the top of zones 2, 4, 5, 6, 7 and 8, respectively. Post-grouting bored piles are employed for the structure foundation.

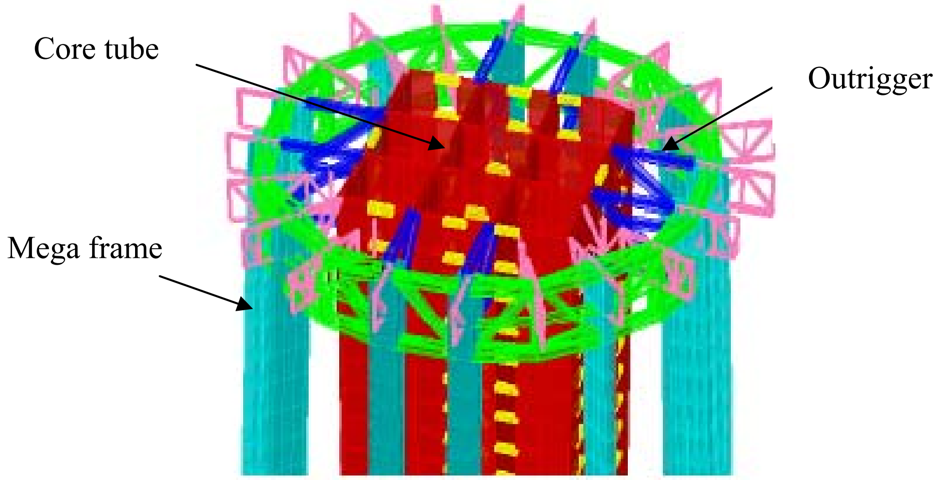

Figure 3.2 Components of the structure

3.2.1.1 The core wall inner tube

The inner core wall tube is a square with dimensions of 30 m × 30 m, divided into 9 cells at the bottom of the building. The configuration of the core wall changes along the height of the building: the four corner cells are partially removed from zone 5, and further removed to be a cross arrangement (5 cells) at zone 7 before forming a rectangle (3 cells) at the top of the tube (Figure 3.3). The thickness of the core wall varies from 1.2 m at the bottom of the building to the minimum of 0.5 m at the top. From the bottom, steel plates are imbedded in the flange walls and web walls of the core tube to form composite shear walls for reducing the wall thickness and improving the ductility. C60 grade concrete in according with the Chinese code (GB 50010 2010) is used for the core wall.

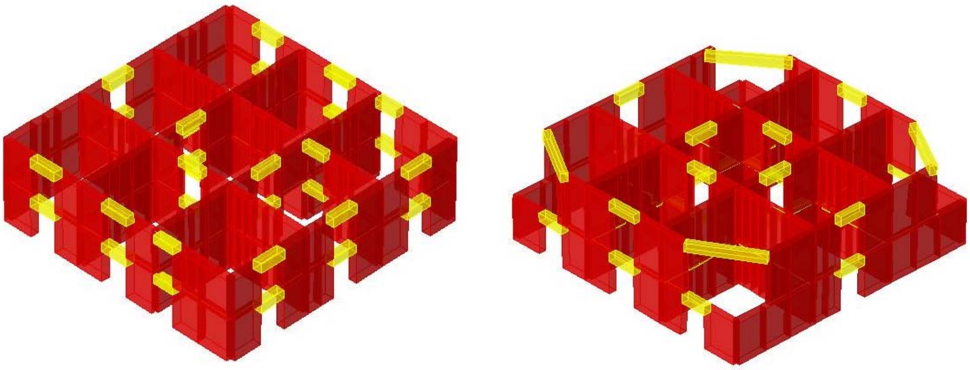

(a) Zone 1 ~ zone 4 (b) Between zone 4 and zone 5

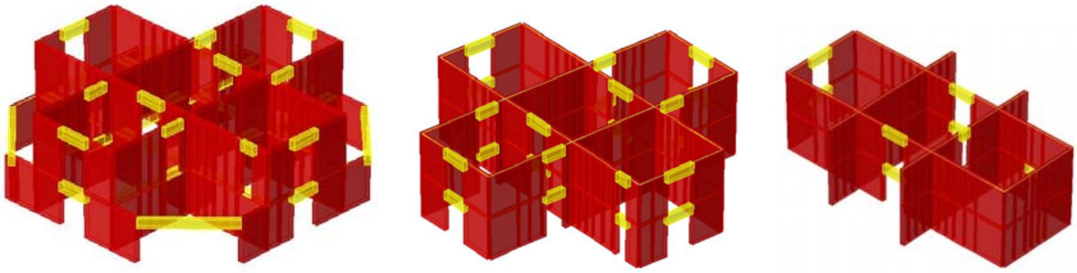

(c) Between zone 6 and zone 7 (d) Zone 7 (e) At the top

Figure 3.3 Cross section of the core tube

3.2.1.2 The outer mega frame

The mega frame consists of eight super columns, four corner columns, radial trusses, and two-storey high belt trusses (Figure 3.4). The eight super columns extend to zone 8, while the four corner columns to zone 5. The four corner columns are designed mainly for reducing the spans of the belt trusses below zone 6. All columns inclined in the vertical direction toward the center of the core tube gradually. The dimensions of the super columns decrease from 5.3 m × 4.3 m at the underground level to the minimum of 2.4 m × 1.9 m at the top of the columns. In order to support a twisting double-layer glass curtain wall system around the whole building, radial trusses are installed at the strengthening floors at each zone. A two-storey high belt truss is designed in each zone as the transferring truss to resist the vertical load of the outer tube above the zone.

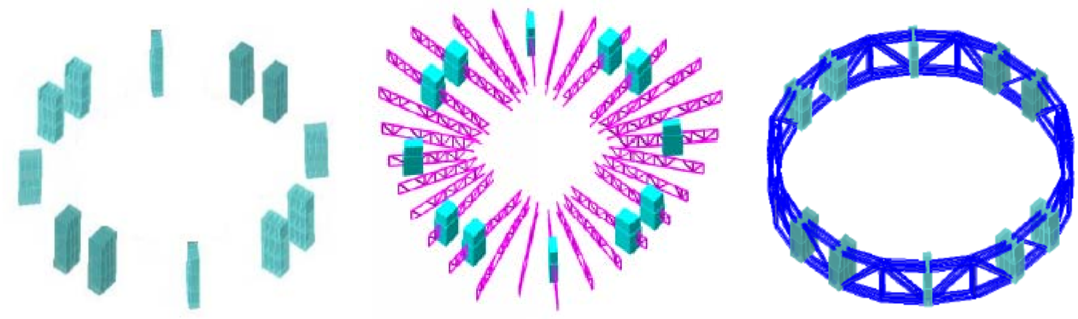

(a) Columns (b) Radial trusses (c) Belt trusses

Figure 3.4 Components of the mega frame

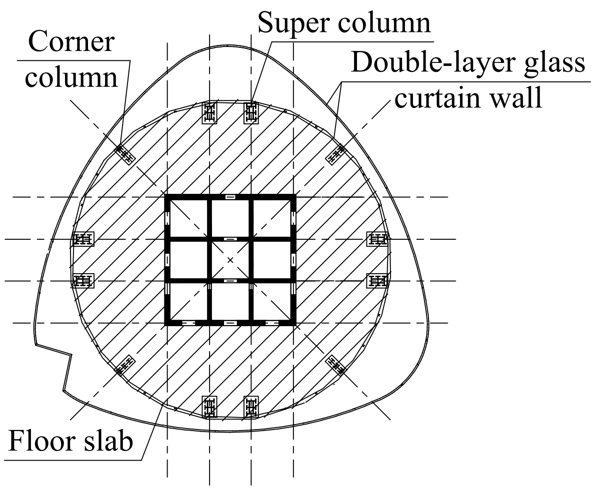

Figure 3.5 A typical floor plan of the Shanghai Tower

3.2.1.3 The floor

A typical floor plan in Zone 2 is shown in Figure 3.5. The floor is made of a composite decking with profiled steel sheet as the permanent bottom formwork for the RC slab. The inner layer glass curtain wall is set along the periphery of the floor slab, while the outer layer attaches to the radial trusses.

3.2.2 Structural Performance Monitoring System

For this complex structure, the strains and stresses at critical components, the deflection and settlement of the global structure, and the structural performance of the building under extreme loadings during the construction and service stages are the main concerns to the designer, the contractor, and the client.

A sophisticated structural performance monitoring system has been installed to monitor the performance of the building during both construction and service stages. This system will also ensure the construction error of the structure within the allowable limit specified in the design. After completion of structure, the in-construction monitoring system will be extended for the in-service monitoring.

The SHM system for Shanghai Tower has been devised in accordance with the modular design concept, which has been practiced for the Tsing Ma Suspension Bridge (Xu and Xia 2012) and the Canton Tower. The in-construction monitoring system consists of four modules: sensory system, data acquisition and transmission system, data processing and control system, and structural performance evaluation system.

The sensory system is responsible to collect the raw data from various types of sensors. As listed in Table 3.1, the sensory system consists of more than 400 sensors of 11 different types. These sensors are deployed for monitoring three categories of parameters: loadings (wind pressure, structural temperature, and earthquake), structural responses (settlement, inclination, displacement, strain, and acceleration), and environmental effects (ambient temperature and wind). Layout of the sensors is illustrated in Figure 3.6.

Table 3.1 Sensors deployed in the monitoring system

No.	Sensor Type	Monitoring Items	Number of Sensors
1	Seismograph	Earthquake motion	2
2	Anemometer	Wind speed and direction	1
3	Wind pressure sensor	Wind pressure	27
4	Accelerometer	Acceleration	71
5	Inclinometer	Inclination	40
6	Thermometer	Air and structure temperature	75
7	Strain gauge	Strain	209
8	GPS	Displacement	3
9	Total station	Displacement, leveling and settlement	2
10	Digital level	Leveling of floors	1
11	Digital video camera	Displacement	1
		Total:	**432**

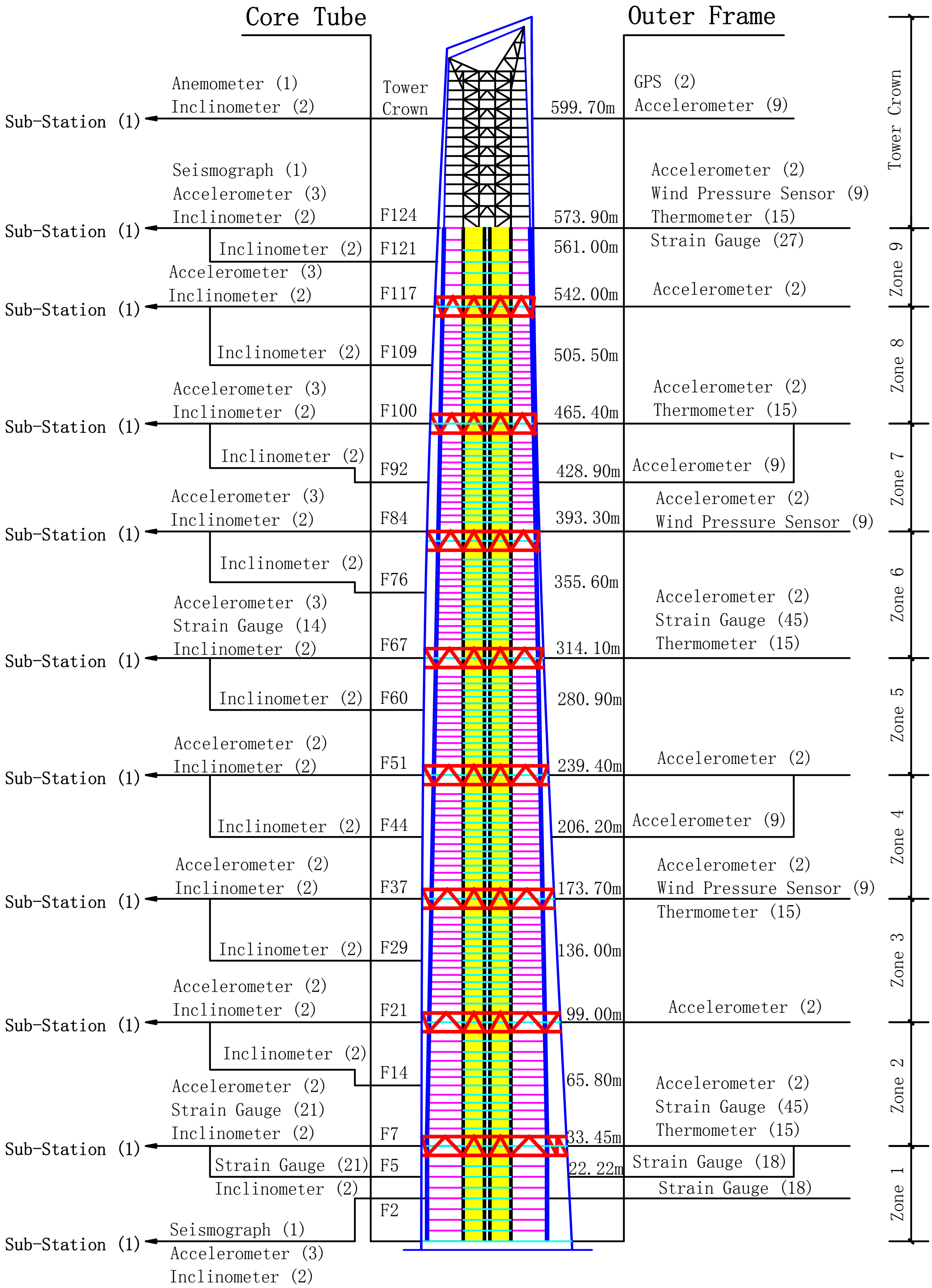

Figure 3.6 Sensor layout of the monitoring system

All these sensors were selected to capture important information about the structural static and dynamic properties, and then installed at crucial locations according to the FE analysis of the partial structures at different construction stages. In addition, by combining multiple types of sensors and data fusion, the accuracy of the measurand can be improved. For example, a video camera, GPS, and total station are deployed for the measurement of horizontal displacement at the top of the structure at various construction stages for cross-checking; a combination of GPS, accelerometers, and inclinometers is adopted to achieve a reliable measurement of static and dynamic displacement.

The data acquisition and transmission system consists of 11 stand-alone sub-stations, shown in Figure 3.6, which are distributed along cross-sections at different heights of the building to collect the signals from surrounding sensors. The real-time data acquired from the sensors are transmitted from the sub-stations to the site central control room via a wireless system during the in-construction monitoring. This wireless system will be replaced by a wired system for guaranteeing long term monitoring during the service stage.

The data processing and control system comprises a high-performance computer system and data processing software, which is located in the central control room to control the sub-stations regarding data acquisition and pre-processing, data transmission and filing, data management and displaying.

The structural performance evaluation system is composed of a condition evaluation system and a structural performance and safety assessment system. The condition evaluation system is mainly utilized to promptly evaluate the structural condition by comparing the static and dynamic measurement data with the design parameters, FE model analysis results, and pre-determined threshold values. The functions of the structural performance and safety assessment system include but not limited to construction stage analysis, structural analysis, parameter sensitivity analysis, structural identification, FE model modification, and false alarming. The basic configuration of the monitoring system is shown in Figure 3.7.

The structural performance monitoring system for the Shanghai Tower integrates both in-construction monitoring and in-service monitoring. This integrated monitoring system enables to track complete data histories from the onset of structural components. Especially for strain gauge, it is able to monitor the total strain rather than relative strain, which is necessary for evaluating the real performance index of structural components under extreme loading events. In addition, foundation settlement during the construction stage is general larger than that during the service stage. The former provides valuable reference to the latter. These reflect the merit of the integrated monitoring system which acquires the complete monitoring data from construction to service stages.

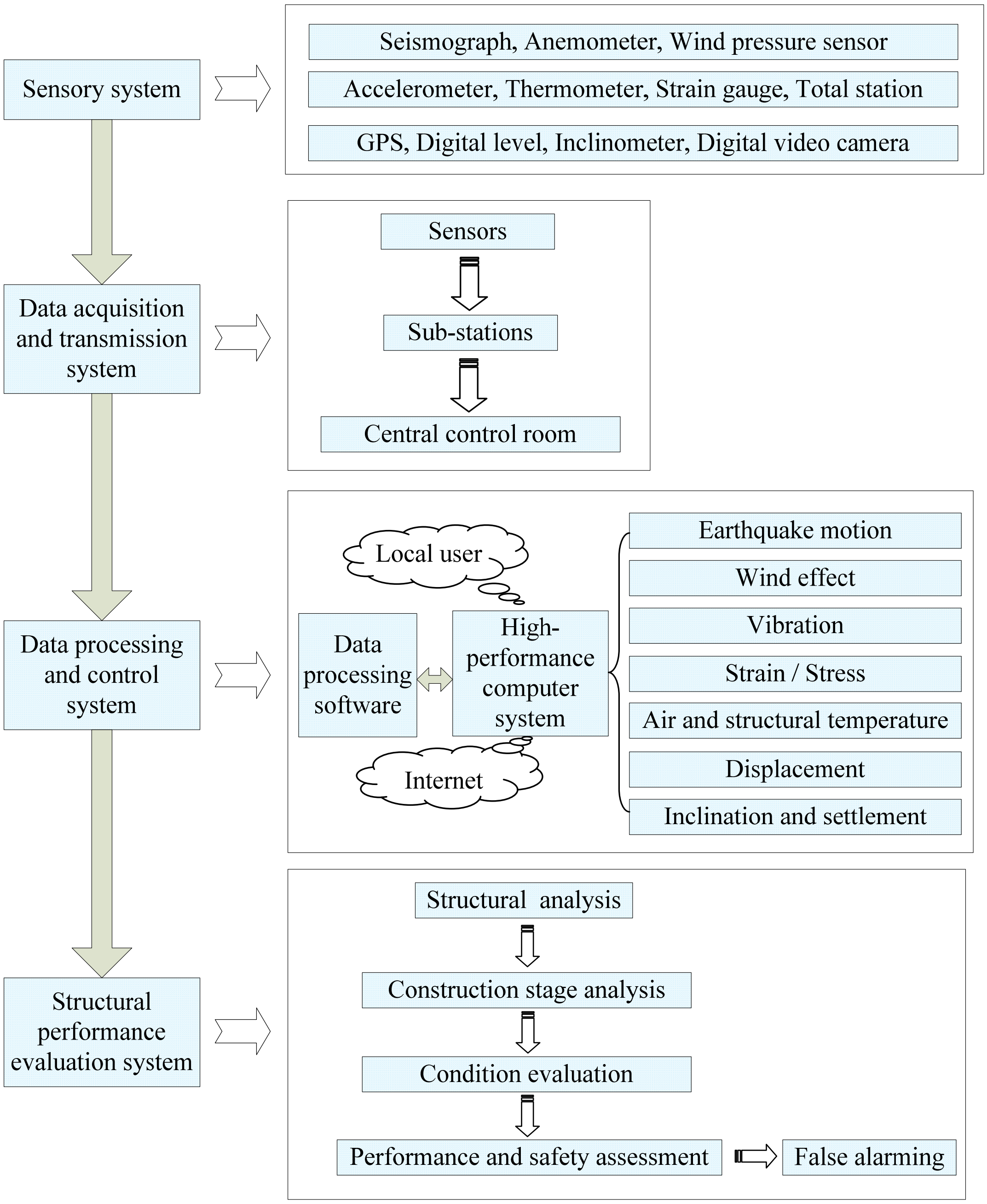

Figure 3.7 The basic configuration of the SHM system

3.3 Canton Tower

3.3.1 Structure Description

As illustrated in Figure 3.8, the Canton Tower is a typical supertall tube-in-tube structure with a total height of 600 m, consisting of a RC inner tube and a steel outer tube. 37 functional floors and four levels of connection girders link the inner tube and the outer tube together, as shown in Figure 3.8(b). These functional floors serve for various functions including TV and radio signals transmission facilities, open-air skywalk, offices, entertainment facilities, and so on.

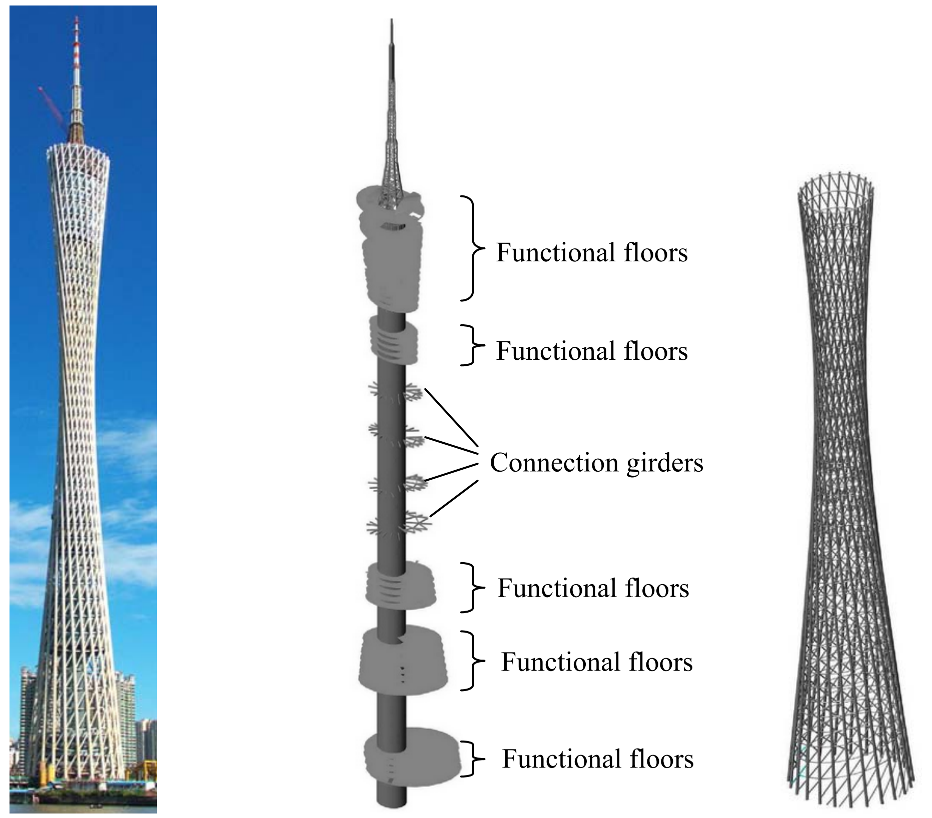

(a) Bird-view (b) Inner tube (c) Outer tube

Figure 3.8 Canton Tower

The inner tube is a RC core wall of an elliptical cross-section with a constant planar dimension of 14 m × 17 m. The thickness of the core wall varies from 1.0 m at the bottom to 0.4 m at the top. The outer structure consists of 24 concrete-filled-tube (CFT) columns uniformly spaced in an ellipse configuration and inclined in the vertical direction, which are transversely interconnected by steel ring beams and bracings (see Figure 3.9). The diameter of CFT columns decreases from 2.0 m at the bottom to 1.2 m at the top gradually. The planar ellipse decreases from 50 m × 80 m at the ground to the minimum of 20.65 m × 27.5 m at the "waist" level (280 m high) and then increases to 41 m × 55 m at the top of the tube (454 m).

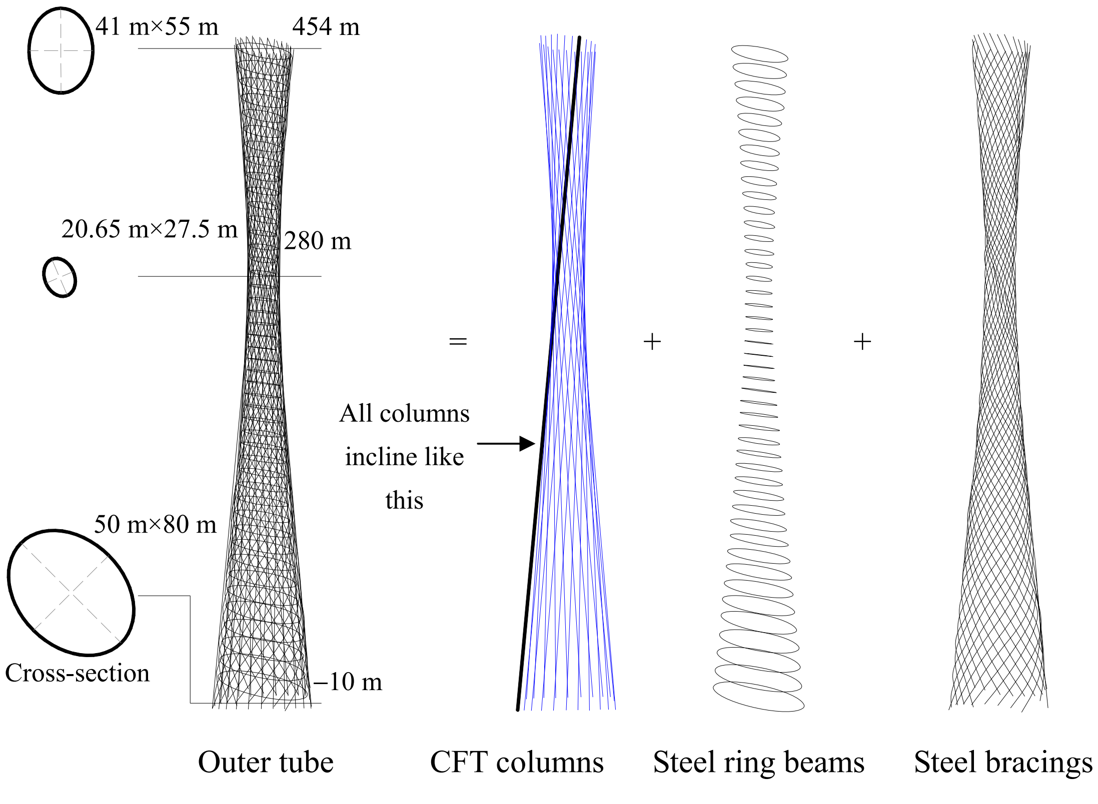

Figure 3.9 Structural components of outer tube

Figure 3.10 shows a typical functional floor plan that is made of a composite deck with profiled steel sheets at bottom as the permanent formwork for the RC slab. Radiating steel girders stretch out from the bottom of the floor and are pin connected to the corresponding CFT columns through a bolt joint in the CFT. A curtain wall is attached along the periphery of the floor slab. Along the vertical direction, only the segments of functional floors are enclosed by curtain wall enclosing, such that solar radiation cannot directly reach the inner structure of those parts. In contrast, the entire outer tube and that inner tube without functional floors are exposed to the ambient air and solar radiation directly. Therefore, the inner and outer tubes are subject to different thermal loadings.

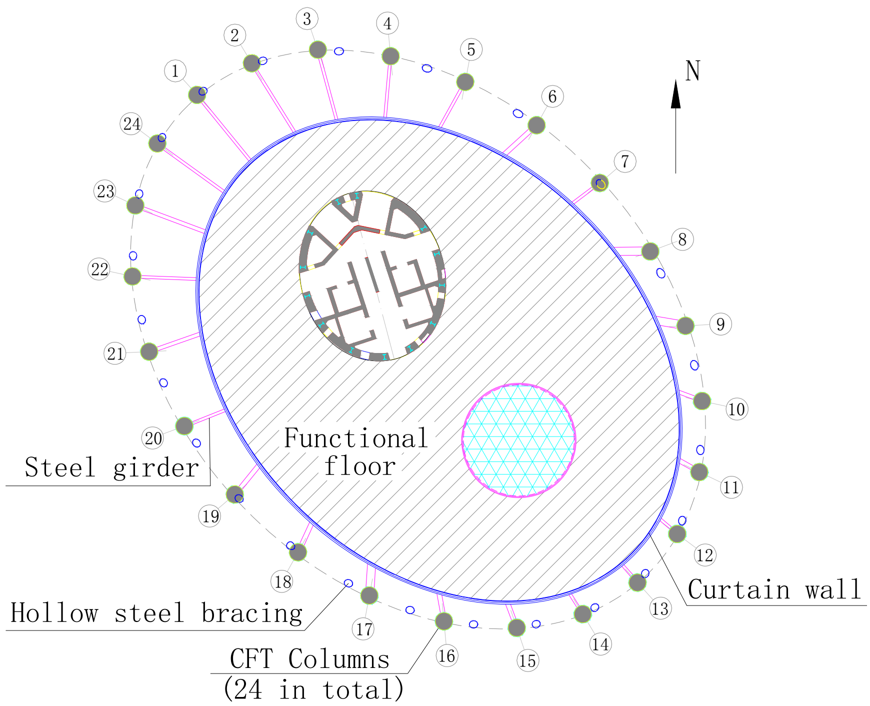

Figure 3.10 A typical functional floor plan of the Canton Tower

3.3.2 SHM System of Canton Tower

A comprehensive long-term SHM system has been implemented for integrated in-construction and in-service monitoring of Canton Tower, which was in synchronism with its construction process. The SHM system for Canton Tower has been devised with six modules (Ni *et al.* 2009b). It includes six modules: sensory system, data acquisition and transmission system, data processing and control system, data management system, structural health evaluation system, and inspection and maintenance system, as shown in Figure 3.11.

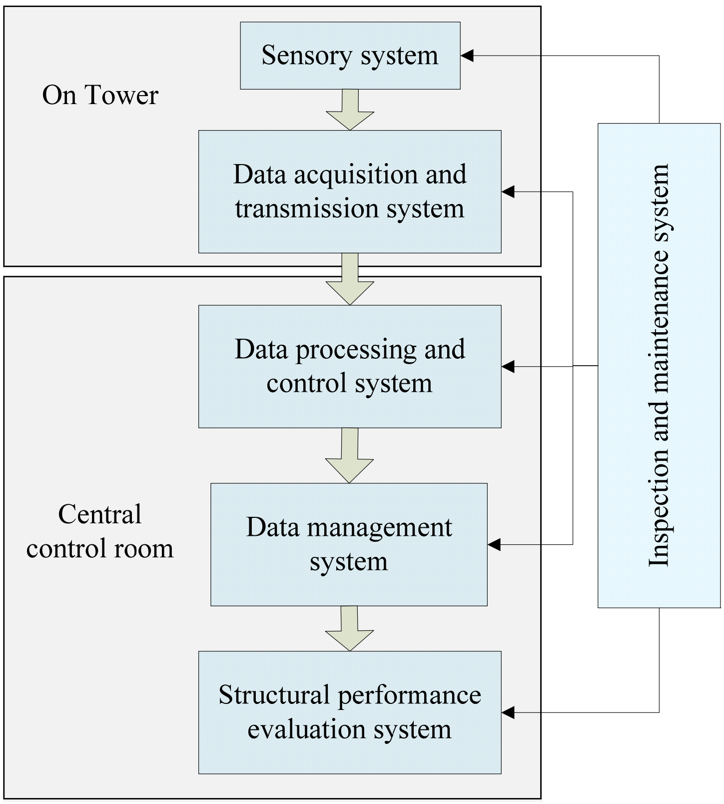

Figure 3.11 Modules of SHM system for Canton Tower

Table 3.2 Sensors deployed in SHM system for Canton Tower

No.	Sensor Type	Monitoring Items	Number of Sensors
1	Weather station	Temperature, humidity, rain, and air pressure	1
2	Anemometer	Wind speed and direction	2
3	Wind pressure sensor	Wind pressure	4
4	Tiltmeter	Inclination	2
5	Zenithal telescope	Inclination	2
6	Level sensor	Leveling of floors	2
7	Theodolite	Elevation	2
8	Total station	Displacement, leveling and settlement	1
9	GPS	Displacement	2
10	Digital video camera	Displacement	3
11	Seismograph	Earthquake motion	1
12	Corrosion sensor	Corrosion of reinforcement	3
13	Accelerometer	Acceleration	22
14	Fiber optic sensor	Strain and temperature	208
15	Vibrating wire gauge	Strain, shrinkage and creep	416
16	Thermometer	Structure temperature	172
		Total:	**843**

The sensory system consists of more than 800 sensors of 16 different types on the main tower, as listed in Table 3.2. The data acquisition and transmission system consists of 13 stand-alone sub-stations for in-construction monitoring and 6 stand-alone sub-stations for in-service monitoring. They are distributed along cross-sections at different heights of the building to collect the signals from surrounding sensors. All substations are connected together to the central data warehouse.

3.3.3 Temperature and Strain/Stress Monitoring System

The strain and temperature monitoring system is employed during the construction stage, comprising vibrating wire strain gauges and thermal sensors distributed along 12 cross-sections at different heights, as illustrated in Figure 3.12. They correspond to the concrete inner core wall at the elevations of 32.8 m, 100.4 m, 121.2 m, 173.2 m, 204.4 m, 230.4 m, 272.0 m, 303.2 m, 334.4 m, 355.2 m, 386.4 m, and 438.4 m and the corresponding ring Nos. 3, 9, 11, 17, 21, 24, 28, 32, 35, 38, 40, and 45 at the outer tubular structure.

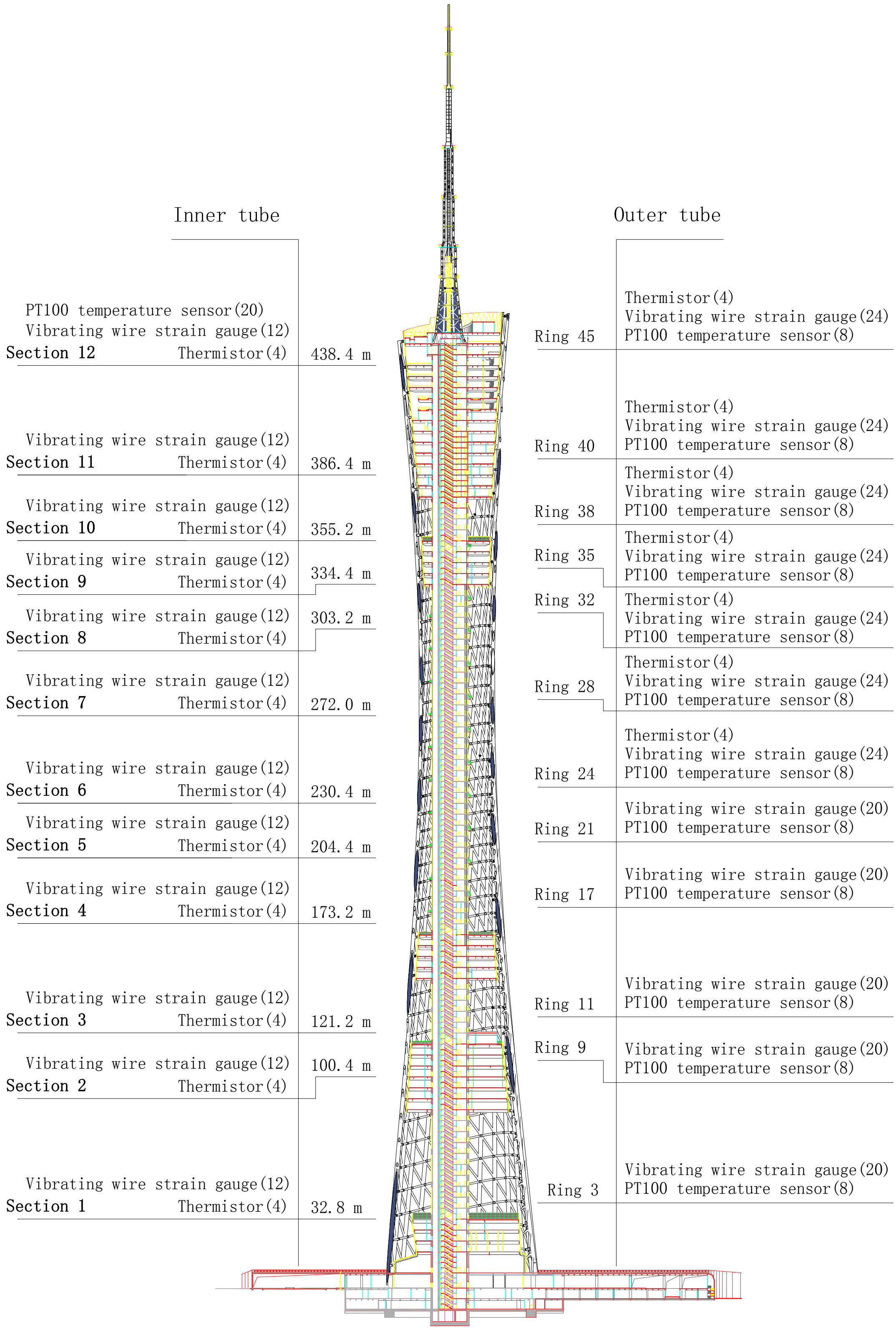

Figure 3.12 Deployment of temperature and strain sensors for Canton Tower

Four points (denoted as Point 1 to Point 4 in Figure 3.13) at each monitoring section of the inner tube are installed with a 45° strain rosette. Each rosette consists of three Geokon vibrating wire strain gauges to measure the strain and temperature of the concrete inner wall. A vibrating wire gauge consists of a thermal couple to measure temperature and a wire to measure strain through the relation between the wire tension and its vibration frequency. The positions of these four points are identical at each section along the height of the structure.

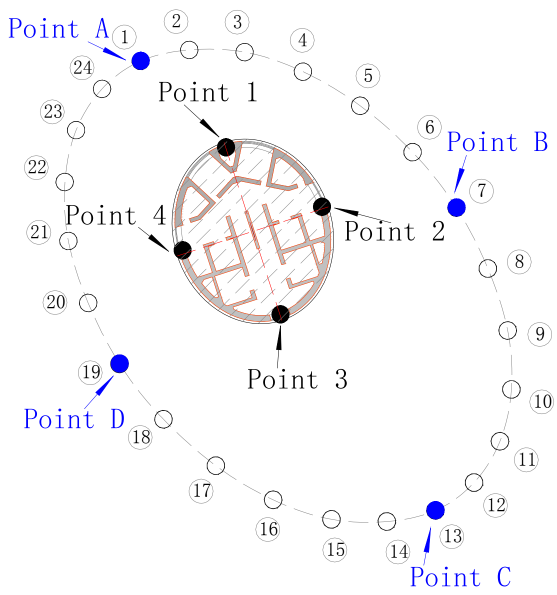

Figure 3.13 Plan position of measurement points

The sensors initially installed at Sections 1 and 2 were damaged by site labours and same number of sensors were then attached on the exterior surface of the RC core wall. All sensors at other sections were embedded at the middle of the wall thickness. The surface-type sensor is Geokon 4000 and the embedded-type is Geokon 4200 (Geokon 4000; Geokon 4200).

Another four points (denoted as Point A to Point D in Figure 3.13) at each section of the outer tube were also installed with strain and temperature sensors. Each point has five surface-type vibration wires (Geokon 4000) installed on the steel surface. In particular, three sensors (No. 3 ~ 5) are on the CFT, one on the ring bar (No. 1) and one on the brace (No. 2) (Figure 3.14). In addition, each CFT column has two PT100 temperature sensors (No. 6 ~ 7) attached on the steel surface. These two surface-type temperature sensors were installed on the exterior surface of the column, one facing to the inner tube and the other to outward. From Section 6 to Section 12, each CFT column also has one strain sensor (No. 0) (Geokon 4200) embedded inside the concrete, which was located at one-third of the radius from the surface (Figure 3.14).

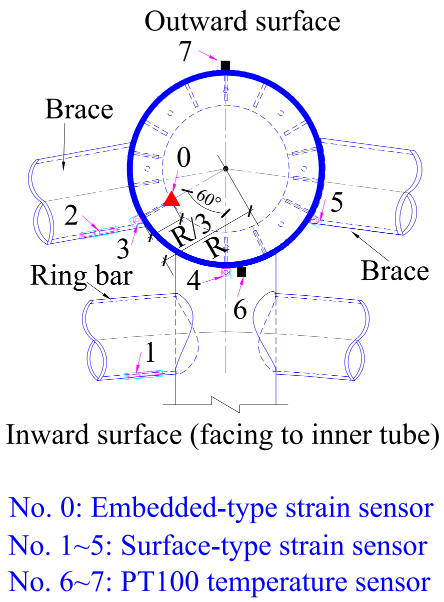

Figure 3.14 Layout of sensors on outer CFT joint

Figure 3.15 shows the installation of an embedded-type 45° strain rosette in the RC wall of the inner tube. Figure 3.15(a) is a photograph of an original Geokon 4200 strain gauge. To measure the strain of the concrete and protect sensors, the vibrating wire strain gauges were coated with concrete the day before the concrete was poured.

To minimize the shrinkage effect, the concrete coating must be the same as that used in the RC wall, as shown in Figure 3.15(b). Then, the 45° strain rosette was firmed to the rebars to measure the strain in three directions (Figure 3.15(c)). The transmission cables were protected by steel pipes embedded in the concrete floor (Figure 3.15(d)). After several days hardening, as the strain and temperature readings became stable, they can be regarded as the initial strain and temperature of the concrete.

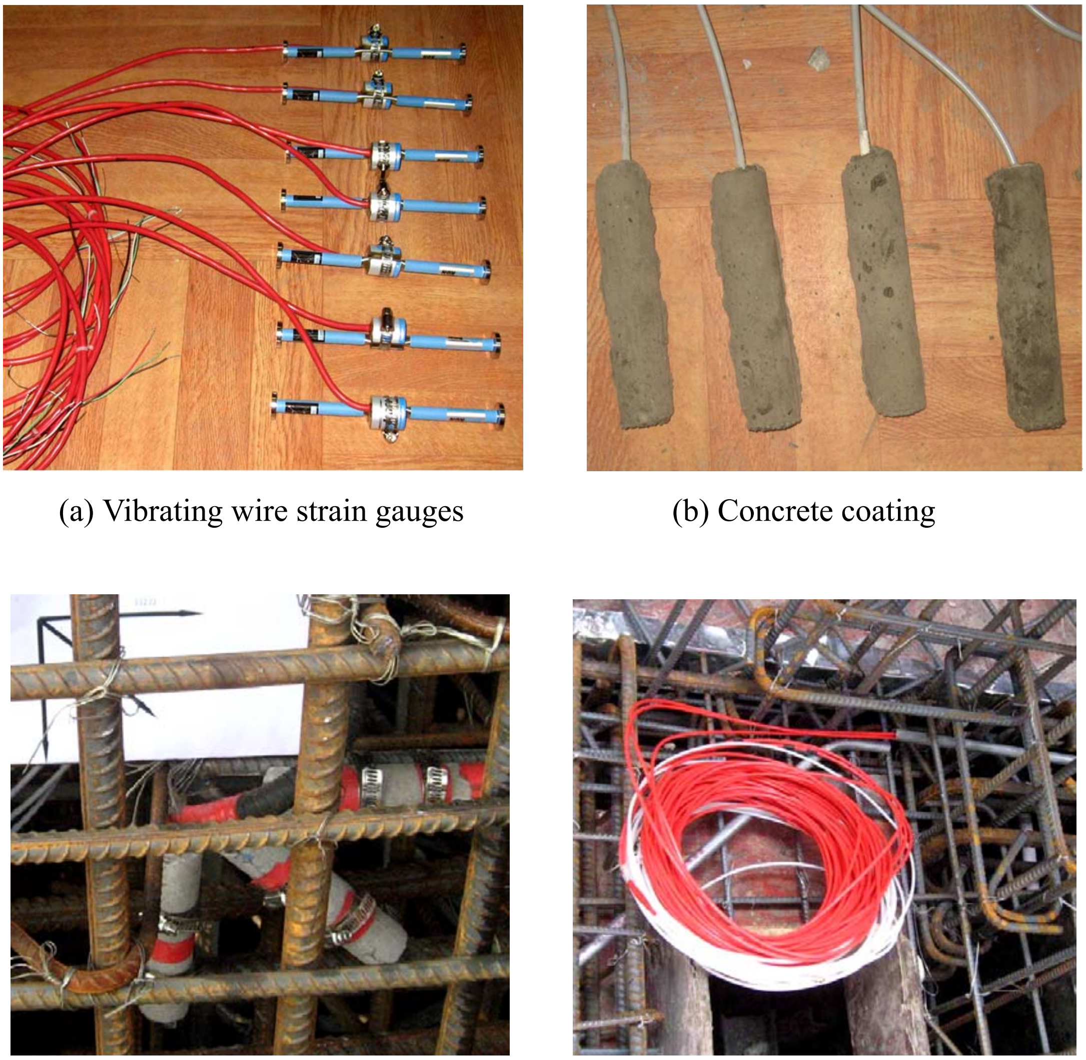

(a) Vibrating wire strain gauges (b) Concrete coating

(c) 45° strain rosette (d) Protection pipe and the transmission cable

Figure 3.15 Installation of embedded-type vibrating wire strain gauges

Figure 3.16 shows the installation of vibrating wire strain gauges and temperature sensors on outer CFT column. The embedded-type strain gauge was attached firmly to the rib plate located at one-third of the radius from the surface of the CFT column (Figure 3.16(a)). The surface-type strain gauges were installed on the mounts that had been welded on the outside surface of the CFT column in factory to avoid damaging the coating of the column (Figure 3.16(b)). These strain gauge and PT-100 temperature sensors (Figure 3.16(c)) were protected in a case, as shown in Figure 3.16(d).

(a) Vibrating wire strain gauges installed inside the CFT column

(b) Installation mounts on CFT column

(c) PT100 temperature sensor (d) Sensors installed outside the CFT column

Figure 3.16 Installation of sensors on outer CFT column

Figure 3.17 Installation of temperature sensors in the RC wall of the inner tube

Section 12 was selected to install PT100 temperature sensors into the RC wall along the thickness direction with equal spacing to measure the temperature gradient of the wall during the construction stages. These sensors were installed at Point 1 to Point 4 of the inner tube, five at each point.

Similar to the embedded-type strain gauges, these temperature sensors were wrapped in concrete (as shown in Figure 3.17) to prevent from damaging in the concrete pouring process on the construction site. The measured temperatuer and strain data will be analyzed in Chapter Five and Chapter Six, respectively.

3.3.4 Horizontal Displacement Monitoring at the Top of the Tower

A GPS system was installed to monitor the horizontal displacement of the Canton Tower. The reference station (Figure 3.18(a)) was installed above the sightseeing platform at 10.2 m near the tower. The rover station (Figure 3.18(b)) was installed on the top of the tower at approximately 460 m high. The operational effectiveness and the accuracy of this GPS-based monitoring system have been verified by Xia *et al.* (2014). The temperature-induced horizontal displacement will be presented in Chapter Six.

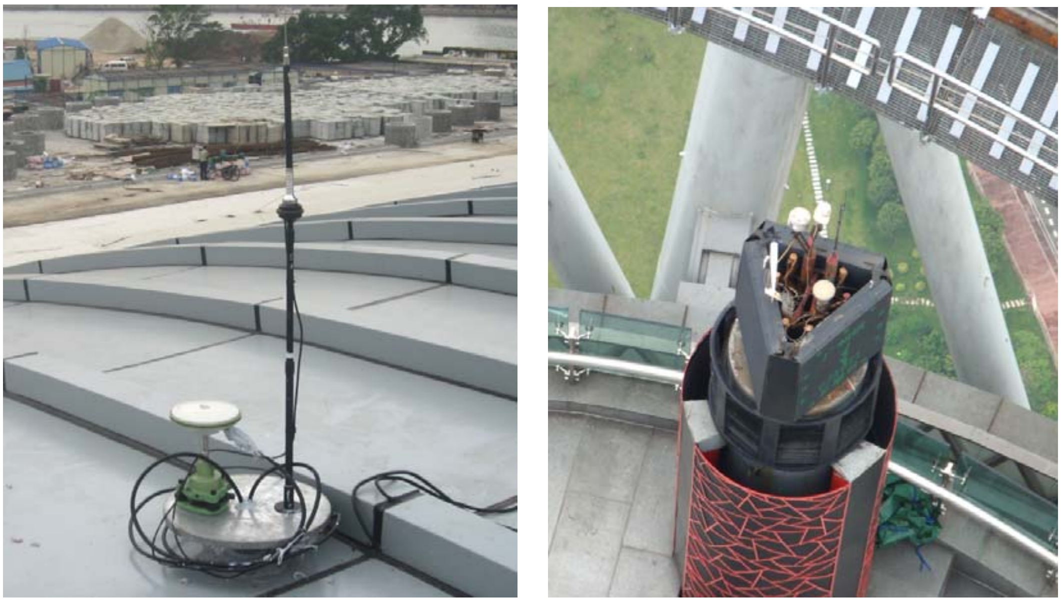

(a) Reference station (b) Rover station

Figure 3.18 GPS system installed on the tower

3.4 Summary

This chapter described the structural configuration and SHM systems of the Shanghai Tower and the Canton Tower. The temperature and strain/stress monitoring system and horizontal displacement monitoring system for the Canton Tower are also detailed.

CHAPTER FOUR

SETTLEMENT MONITORING OF SHANGHAI TOWER

4.1 Introduction

During the construction of supertall buildings, the settlement of foundations and compression deformation between upper floors will increase, resulting from the increasing dead load. The floor elevations in the final state (after the structure construction completes) need to suffice design requirement. Therefore, it is necessary to timely measure the foundation settlement, predict the settlement of upper floors, and find the difference between prediction and measurement for revising the predicted values afterward.

As the construction is progressing, the structural state changes. Consequently the settlement can be regarded as a dynamic model contaminated noise. This model can be described as a discrete Kalman Filtering model (Kalman 1960). The Kalman Filtering, also known as what is called the linear-quadratic estimation, is an algorithm that operates recursively a series of measurements corrupted by random variations and other inaccuracies, and produces a statistically optimal estimate of the system state.

The Kalman Filter technique combines a system's dynamic model and measurements to form an estimate of the system's varying quantities that is better than the estimate obtained by measurement alone (Brown and Hwang 1992). The Kalman Filter has a wide application in time series analysis such as signal processing and econometrics (Grewal and Andrews 2001).

In the field of civil structural engineering, there have been a number of applications of the Kalman Filtering method to the construction control. For example, it has been used in cable tension control of the Jiao-Ping-Du cable-stayed bridge such that the profile and internal force of the bridge are more reasonable after the cable replacement. It ensured the forces of the structure consistent with the theoretical values (Lin 1983). The Kalman Filtering technique was used for the control of the galloping related vibration in the long-span bridge tower (Alam *et al.* 1995). Chen (2010) applied the technique to reduce the negative effect of measurement noise in bridge reconstruction. These applications have verified the effectiveness of the Kalman Filter in the state control. Zhang *et al.* (2011) used the adaptive Kalman Filter to establish the dynamic monitoring model of long-span bridges, considering the wind speed, temperature, traffic flow and other external influences.

This chapter will combine the Kalman Filtering approach and the FE forward construction stage analysis to improve the precision of the construction settlement monitoring of supertall buildings.

4.2 Settlement Measurement

4.2.1 Settlement Measurement Scheme

Using the Shanghai Tower as the test-bed, a total of 15 controlling floors are selected which are located on the strengthening floors and the midst between them, as illustrated in Figure 4.1(a). A series of elevation measurement points are set at each controlling floor, and two points of them are defined as the control point for the core wall and super column, as shown in Figure 4.1(b ~ d).

A total positioning system and a digital level are employed to monitor the elevation of the foundation floor and the superstructure floors (Figure 4.2). The total positioning system has a total station (Leica TCRA1201+R1000), with the accuracy of 1 mm ± 1.5 ppm (parts-per-million). The digital level is Leica Sprinter 250m, offers 1.0 mm standard deviation for height measurement per 1 km double run using the standard 4-section aluminum barcode staff.

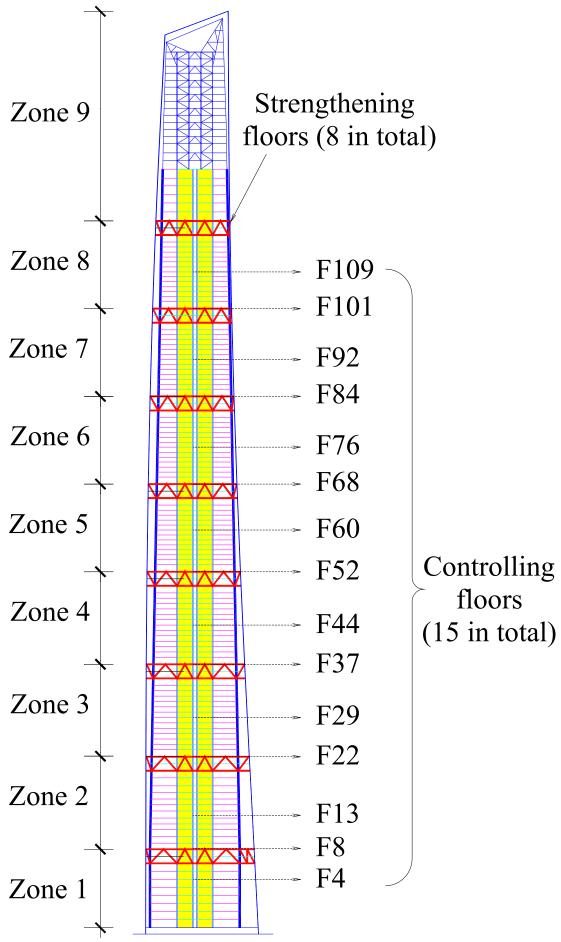

(a) Elevation of structure

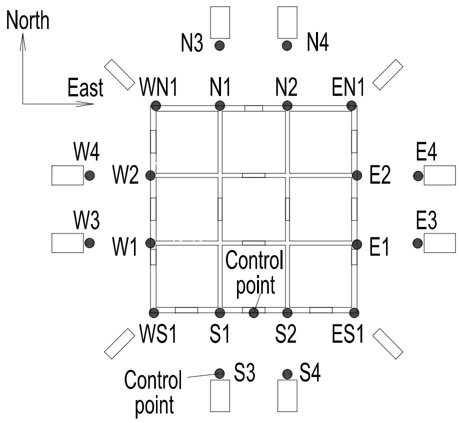

(b) Zone 1 ~ Zone 4

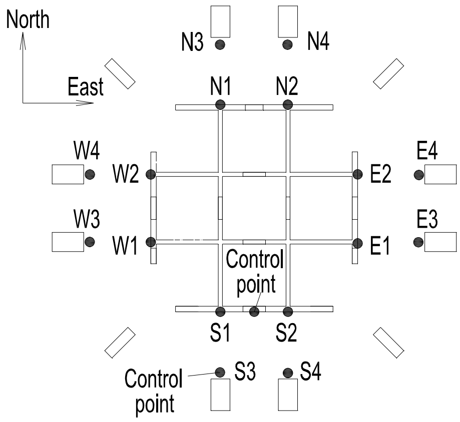

(c) Zone 5

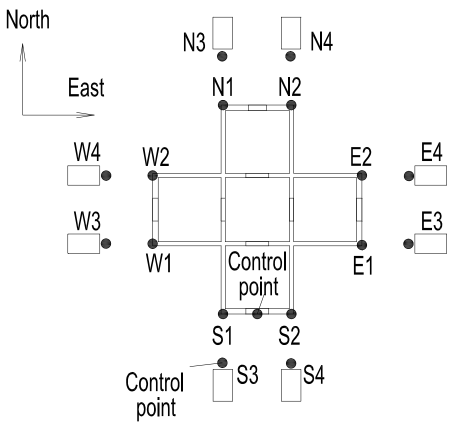

(d) Zone 6 ~ Zone 8

Figure 4.1 Controlling floors and points for settlement monitoring

The floor elevation at the control points are measured from the foundation floor, in which a total station is used as the transit station. In addition, a series of points at the monitoring floor around the core wall and super columns are selected as the reference points to measure the relative settlement and levelness of the upper floors. As a result, the real settlement of the monitoring floor can be obtained from its relative settlement plus the settlement of the foundation floor, which provides as an important reference value for evaluating the prearranged height of the floor elevation afterward.

In order to minimize the influences of environmental factors and improve the measurement precision, the measurement is carried out when the wind speed is small and temperature conditions are stable. The temperature effect on the structural vertical deformation is considered and removed from the field measurement. The vertical displacement induced by temperature variation is calculated from the FE model by considering difference between the actual temperature and the initial one (20℃).

(a) Total station (b) Digital level

Figure 4.2 Elevation measuring instrument

4.2.2 Foundation Settlement

The measured accumulative foundation settlements on the core wall and super columns during the construction stage are shown in Figure 4.3 and Figure 4.4, respectively. The settlements at different locations of the core wall are almost identical, indicating that the settlement of the core wall is uniform. Consequently, the levelness of the superstructure controlling floors can be evaluated by measuring these floors' settlement. The foundation settlement of the super columns has several millimeters difference. Nevertheless, this difference remains fairly constant during most of the construction period. Therefore, the foundation settlement of super columns is regarded uniform as well. The total foundation settlement of the core wall is larger than that of the super columns. This is because the core wall inner tube was constructed earlier than the outer mega-frame in accordance with the construction schedule. In this regard, the elevation of the core wall and super columns should be controlled separately.

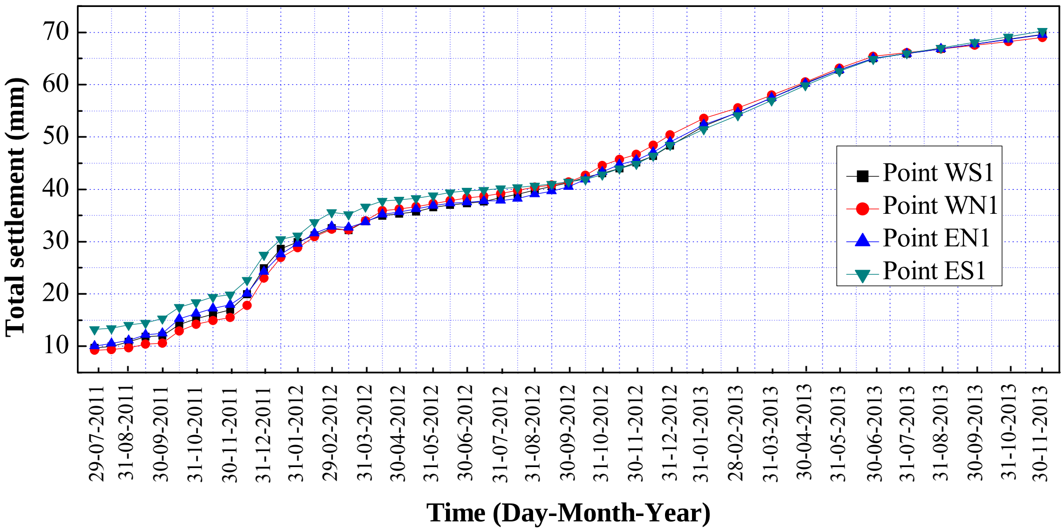

Figure 4.3 Foundation settlement of the core wall

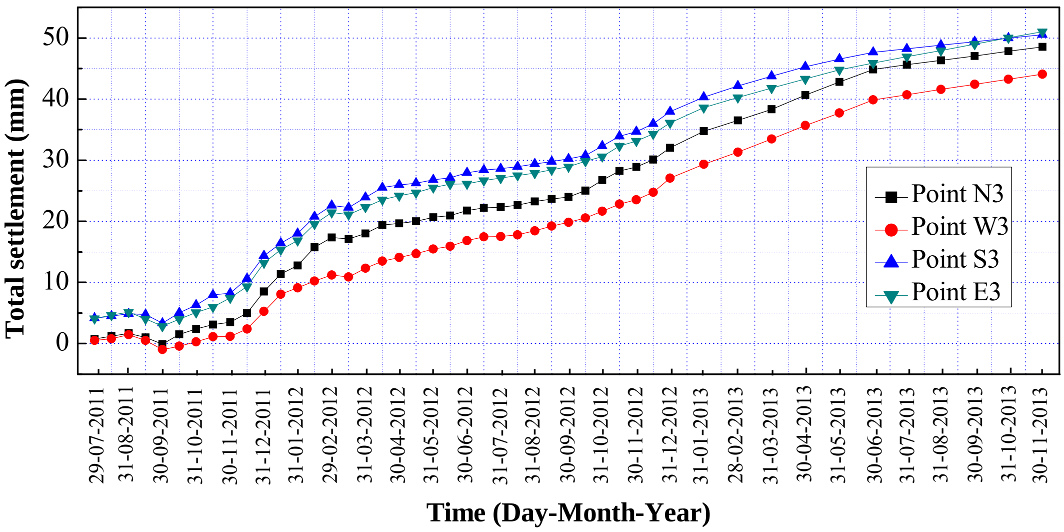

Figure 4.4 Foundation settlement of the super columns

4.2.3 Superstructure Settlement

For the settlement of the superstructure, take one controlling floor (8th floor) during one construction stage (from 5 March 2012 to 26 July 2012) as example. Table 4.1 shows the relative settlement of the measurement points on the core wall and super columns at the 8th floor during this period, in which the temperature effect on the elevation has been eliminated. The compression of the core wall and super column stays at a relatively small value and the settlement is uniform, with an average value of 6.7 mm for the core wall and 7.0 mm for the super column. The average settlement of the core wall and super column are used as the variation of the control points' elevation, and will be applied to the Kalman Filtering analysis in next section. The measured elevation of control points on the core wall and super column at each controlling floor are listed in Table 4.2.

Table 4.1 Relative settlement of the core wall and super columns at the 8th floor during 5 March to 26 July 2012

Structure	Measurement Point	Settlement (mm)	Measurement Point	Settlement (mm)
Core wall	ES1	5.9	WN1	6.8
	E1	6.4	W1	7.0
	E2	7.3	W2	6.5
	WS1	6.9	EN1	7.6
	S1	5.7	N1	7.8
	S2	6.5	N2	6.7
	Average settlement: 6.7 mm			
Super column	E3	7.0	W3	7.1
	E4	7.5	W4	7.0
	S3	5.6	N3	7.9
	S4	6.0	N4	7.9
	Average settlement: 7.0 mm			

Table 4.2 Measured elevation of control points in six controlling floors at different construction stages (Unit: m)

Structure	Floor No.	Initial Elevation	Date							
			05 Mar. 2012	26 Jul. 2012	04 Sep. 2012	08 Nov. 2012	22 Dec. 2012	15 Mar. 2013	12 May. 2013	04 Dec. 2013
Core wall	4th	17.8080	17.8074	17.8008	17.7992	17.7992	17.7973	17.7981	17.7972	17.7962
	8th	38.2864	38.2828	38.2761	38.2757	38.2751	38.2740	38.2729	38.2740	38.2737
	13th	61.8018	61.7969	61.7830	61.7824	61.7792	61.7776	61.7761	61.7771	61.7740
	22nd	104.0108	–	103.9835	103.9802	103.9771	103.9732	103.9757	103.9712	103.9699
	29th	136.4891	–	136.4811	136.4804	136.4758	136.4757	136.4759	136.4742	136.4672
	37th	174.2037	–	174.1909	174.1804	174.1763	174.1735	174.1709	174.1641	174.1557
Super column	4th	17.8080	17.8083	17.8021	17.8030	17.8030	17.8021	17.8027	17.8022	17.8012
	8th	38.2864	38.2848	38.2779	38.2788	38.2800	38.2799	38.2782	38.2794	38.2791
	13th	61.8018	61.7989	61.7853	61.7858	61.7841	61.7839	61.7832	61.7833	61.7801
	22nd	104.0108	–	103.9835	103.9819	103.9804	103.9775	103.9794	103.9746	103.9733
	29th	136.4891	–	136.4809	136.4791	136.4803	136.4811	136.4824	136.4799	136.4725
	37th	174.2037	–	–	174.1943	174.1932	174.1903	174.1880	174.1818	174.1734

4.3 Settlement Monitoring with the Kalman Filtering Technique

4.3.1 Basic Principle of Kalman Filtering Technique

The Kalman Filter technique estimates a process using a form of feedback control: the filter estimates the process state at some time and then obtains feedback in the form of measurements (for example, from sensors) (Welch and Bishop 2001). As such, the Kalman Filter can be conceptualized as two distinct phases: prediction and update. The prediction phase utilizes the state estimate from the previous time step to produce an estimate of the state at the current time step. The predicted state estimate is known as a priori state estimate because it is an estimate of the state at the current time step without including measurement information. In the update phase, the current a priori state estimate is combined with current measurement information to obtain an improved a posterior estimate.

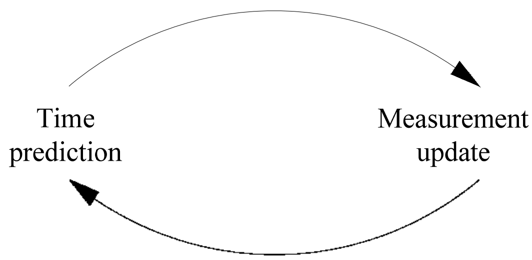

Figure 4.5 The ongoing discrete Kalman Filtering cycle

Typically, these two phases alternate, with the prediction advancing the state until the next scheduled measurement, and the update incorporating the measurement information. Indeed the final estimation algorithm resembles that of a prediction-update algorithm for solving numerical problems as shown in Figure 4.5. The time prediction projects the current state estimate ahead in time. The measurement update adjusts the projected estimate by an actual measurement at that time. However, the update would be skipped by performing multiple prediction steps when the measurement is unavailable for some reason.

The Kalman Filtering model assumes that a discrete time state at time k is evolved from state at k–1 according to

$$X(k) = A(k)X(k-1) + B(k)U(k) + W(k) \tag{4.1}$$

where $A(k)$ is the state transition model applied to the previous state $X(k–1)$; $B(k)$ is the control input model applied to the control vector $U(k)$; and $W(k)$ is the process error assumed to be drawn from a zero mean multivariate normal distribution with covariance $Q(k)$:

$$W(k) \sim N\big(0, Q(k)\big) \tag{4.2}$$

Measurement $Z(k)$ of the true state $X(k)$ at time k is made according to

$$Z(k) = H(k)X(k) + V(k) \tag{4.3}$$

where $H(k)$ is the measurement model mapping the true state system into the measurement system, and $V(k)$ is the measurement noise assumed to be zero mean Gaussian white noise with covariance $R(k)$:

$$V(k) \sim N\big(0, R(k)\big) \tag{4.4}$$

The initial state and the noise vectors at each step are all assumed to be mutually independent.

The equations for the Kalman Filtering model are divided into two groups: time update equations and measurement update equations. The time update equations are responsible for projecting forward (in time) the current state and error covariance estimates to obtain the a priori estimate for the next time step. The measurement update equations are responsible for obtaining an improved a posteriori estimate. In what follows, $\hat{X}(n,m)$ represents the estimate of *X* at time *n* given measurement at time *m*.

The state of the filter is represented by two variables: $\hat{X}(k,k)$ is the a posteriori state estimate at time *k* given measurement at time *k*; and *P*(*k*, *k*) is the a posteriori error covariance matrix, indicating a measure of the estimated accuracy of the state estimate. The equations of the predicted state estimate and predicted estimate covariance are presented as follows:

$$\hat{X}(k,k-1) = A(k)\hat{X}(k-1,k-1) + B(k)U(k) \tag{4.5}$$

$$P(k,k-1) = A(k)P(k-1,k-1)A^T(k) + Q(k) \tag{4.6}$$

For measurement update equations, the measurement residual is

$$\tilde{y}(k) = Z(k) - H(k)\hat{X}(k,k-1) \tag{4.7}$$

The updated state estimate is

$$\hat{X}(k,k) = \hat{X}(k,k-1) + K(k)\tilde{y}(k) \tag{4.8}$$

The invariants values for $\hat{X}(0,0)$ and *P*(0, 0) accurately reflect the distribution of the initial state values. The expected value of the invariants is preserved:

$$E\left[X(k)-\hat{X}(k,k)\right]=E\left[X(k)-\hat{X}(k,k-1)\right]=0 \tag{4.9}$$

$$E\left[\tilde{y}(k)\right]=0 \tag{4.10}$$

Covariance matrices reflect the covariance of estimates

$$P(k,k-1)=\operatorname{cov}\left[X(k)-\hat{X}(k,k-1)\right] \tag{4.11}$$

$$P(k,k)=\operatorname{cov}\left[X(k)-\hat{X}(k,k)\right] \tag{4.12}$$

Substituting Equation (4.8) into Equation (4.12) gives

$$P(k,k)=\operatorname{cov}\left[X(k)-\left(\hat{X}(k,k-1)+K(k)\tilde{y}(k)\right)\right] \tag{4.13}$$

Substituting $\tilde{y}(k)$ and $Z(k)$ into Equation (4.13) gives

$$P(k,k)=\operatorname{cov}\left\{X(k)-\left\{\hat{X}(k,k-1)+K(k)\left[H(k)X(k)+V(k)-H(k)\hat{X}(k,k-1)\right]\right\}\right\} \tag{4.14}$$

Since measurement error $V(k)$ is uncorrelated with other terms, Equation (4.14) can be rewritten as

$$P(k,k)=\operatorname{cov}\left\{\left[I-K(k)H(k)\right]\left[X(k)-\hat{X}(k,k-1)\right]\right\}+\operatorname{cov}\left[K(k)V(k)\right] \tag{4.15}$$

According to the properties of the vector covariance, it becomes

$$\begin{aligned}P(k,k)=&\left[I-K(k)H(k)\right]\operatorname{cov}\left[X(k)-\hat{X}(k,k-1)\right]\left[I-K(k)H(k)\right]^T\\&+K(k)\operatorname{cov}\left[V(k)\right]K(k)^T\end{aligned} \tag{4.16}$$

According to the definition of $P(k, k-1)$ and $R(k)$, the above equation can be further written as

$$P(k,k)=\left[I-K(k)H(k)\right]P(k,k-1)\left[I-K(k)H(k)\right]^{T}+K(k)R(k)K(k)^{T} \quad (4.17)$$

The Kalman Filter is a minimum mean-square error estimator. The goal of the Kalman estimator is to minimize the expected value of the square of the posteriori state estimation. That is accomplished by minimizing the trace of the posteriori estimate covariance matrix $P(k, k)$.

Therefore, the posteriori estimate covariance matrix $P(k, k)$ is minimized when its derivative with respect to the gain matrix is equal to zero.

$$\frac{\partial P(k,k)}{\partial K(k)}=-2\left[H(k)P(k,k-1)\right]^{T}+2K(k)\left[H(k)P(k,k-1)H^{T}(k)+R(k)\right]=0$$

(4.18)

Solving this for $K(k)$ yields the Kalman gain

$$K(k)=P(k,k-1)H^{T}(k)\left[H(k)P(k,k-1)H^{T}(k)+R(k)\right]^{-1} \quad (4.19)$$

Equation (4.17) for calculating the updated estimate covariance can be simplified when the Kalman gain equals the optimal value derived above

$$P(k,k)=\left[I-K(k)H(k)\right]P(k,k-1) \quad (4.20)$$

The first task during the measurement update is to compute the Kalman gain, $K(k)$. The next step is to actually measure the process and obtain $Z(k)$, and then to generate an a posteriori state estimate by incorporating the measurement as in Equation (4.8).

The final step is to obtain an a posteriori error covariance estimate via Equation (4.20).

After each time and measurement update pair, the process is repeated with the previous a posteriori estimates used to project or predict the new a priori estimates. One of the very appealing features of the Kalman Filter is that it recursively conditions the current estimate on all of the past measurements. Figure 4.6 offers a complete procedure of the technique.

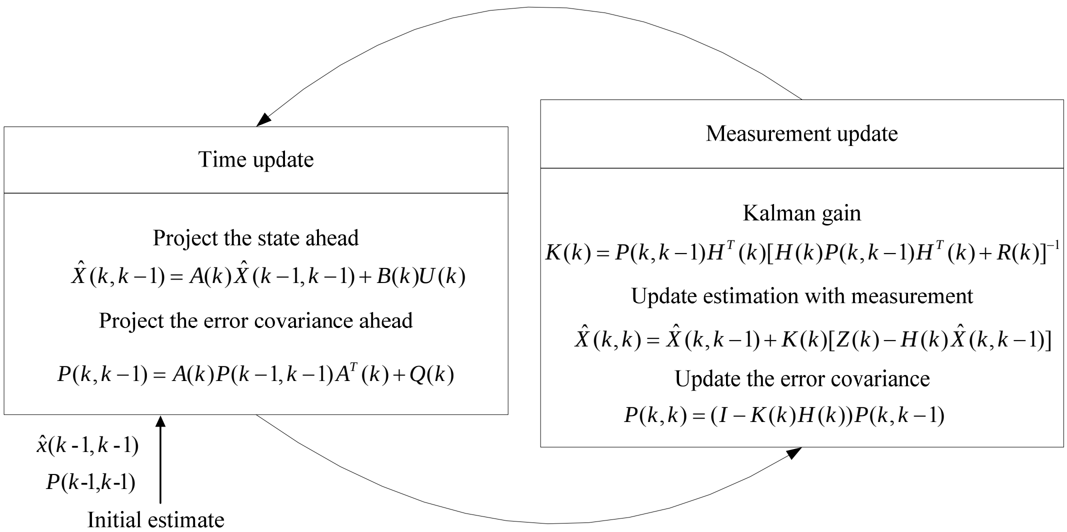

Figure 4.6 A complete procedure of the Kalman Filter

Practical implementation of the Kalman Filter is often difficult due to the difficulty in obtaining an accurate estimate of the noise covariance matrices $Q(k)$ and $R(k)$. Extensive research has been done in this field to estimate these covariances from the measurement data. One of the promising approaches is the auto-covariance least-squares technique that uses auto-covariance of routine operating data to estimate the covariance (Odelson *et al.* 2006; Rajamani and Rawlings 2009).

The Kalman Filtering technique usually needs to have a more accurate grasp of the measurement data and the characteristics of the model in order to achieve the desired results. However, the changing state of the structure is complex. Moreover, obtaining the prior value of filtering is often difficult or its characteristics vary significantly in the process, which may lead to instable filtering.

4.3.2 FE Model of Shanghai Tower

As described previously, the performance monitoring system can track the change in strain responses as well as measure the deflection of the building at different stages of construction. The corresponding FE models are constructed to predict the changing trends, compare with field measurement results, and then verify the effectiveness of the evolution of the monitoring data.

The entire FE model of the Shanghai Tower for construction stage analysis was established using a general FE analysis software package MIDAS/GEN (MIDAS GEN 2012). The entire model consists of 25,790 nodes and 55,983 elements (consisting of 8,315 wall element, 13,301 plate elements, and 34,367 beam elements), as shown in Figure 4.7(a). The enlarged details of the main structural components are shown in Figure 4.7(b ~ e). This FE model is validated with the model presented in Zhang *et al.* (2015). The stress/strain results from numerical analyses of construction process were compatible with the monitored results considering the effect of time-dependent properties of material (such as creep and shrinkage of concrete).

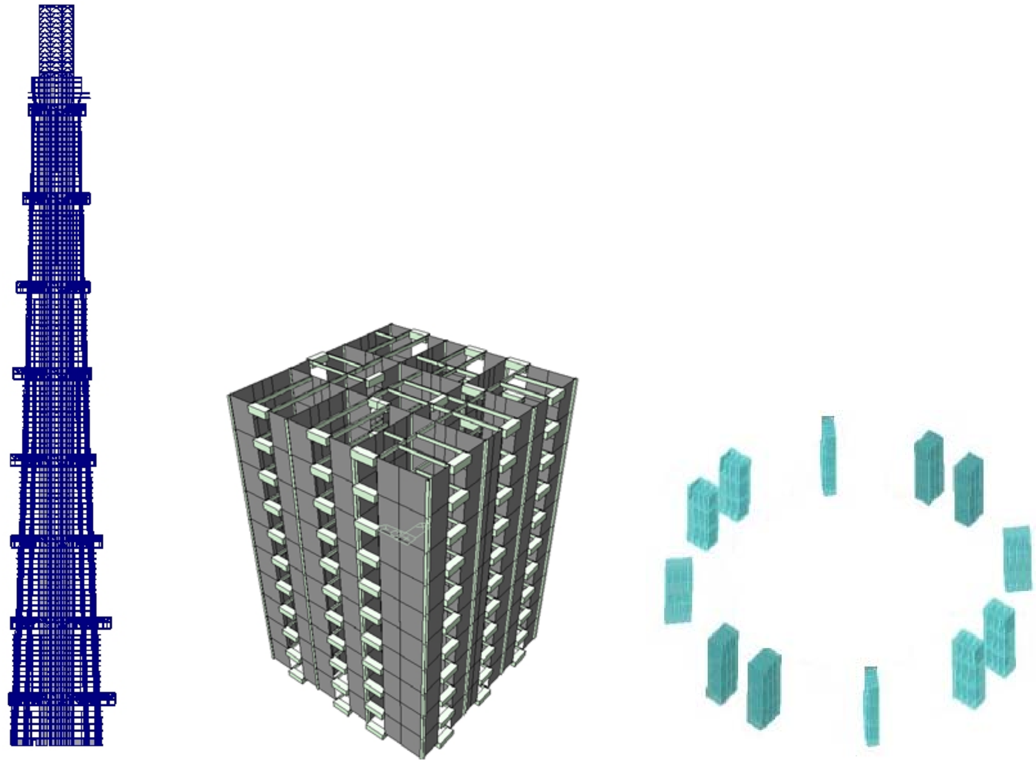

(a) Entire mode (b) Core wall (c) Columns

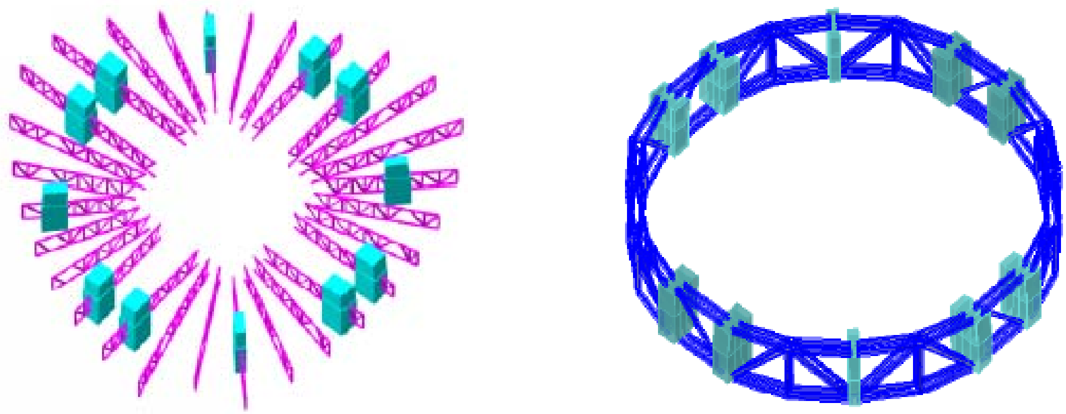

(d) Radial trusses (e) Box belt trusses

Figure 4.7 The FE model of Shanghai Tower

The core wall inner tube of the building was constructed earlier than the outer mega frame and floors according to the construction schedule. The completed core wall is higher than the outer frame, which provides a space to allow four cranes attached to the core wall to lift structural components into place. Photographs of the building at five different construction stages and their FE models according to the actual completed structural components at the time are shown in Figure 4.8 and Figure 4.9, respectively. Besides the dead load of the completed structural components, the mass of major construction facilities including cranes and the construction platform were included in the models.

(a) 2011.07.09 (b) 2011.10.18 (c) 2012.03.05

(d) 2012.05.15 (e) 2012.07.26

Figure 4.8 Photographs of the Shanghai Tower at five different construction stages

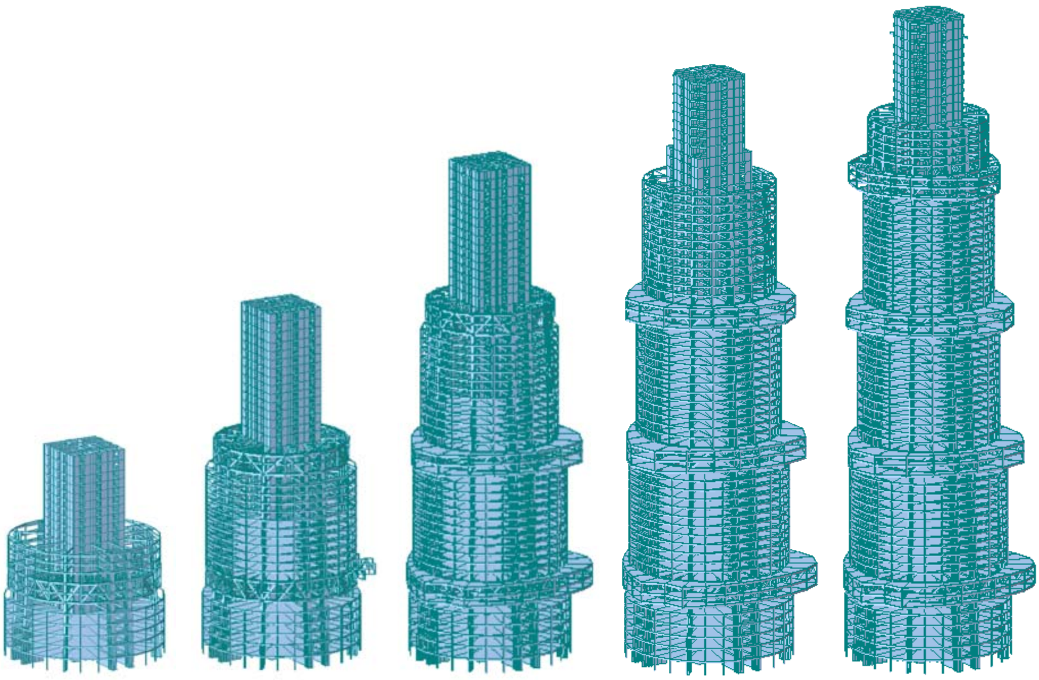

(a) 2011.07.09 (b) 2011.10.18 (c) 2012.03.05 (d) 2012.05.15 (e) 2012.07.26

Figure 4.9 FE models of Shanghai Tower at five construction stages

4.3.3 Application of the Kalman Filtering Technique to Settlement Measurements

In the filtering model, set $A(X)$, $B(X)$, and $H(X)$ as identity matrix I. The specific algorithm of filtering model based on Equations 4.1 and 4.3 is illustrated as Figure 4.10. The initial state and the noise vectors at each step are all assumed to be mutually independent. With the initial value of state variables, the predicted values will be calculated. The first task during the measurement update is to compute the Kalman gain $K(k)$. The next step is to measure the process $Z(k)$, and the posteriori state estimate is obtained by incorporating the measurement. Finally, the posteriori error covariance is estimated. After each time update and measurement update cycle, the process is repeated with the previous posteriori estimate used to project or predict the new a priori estimate.

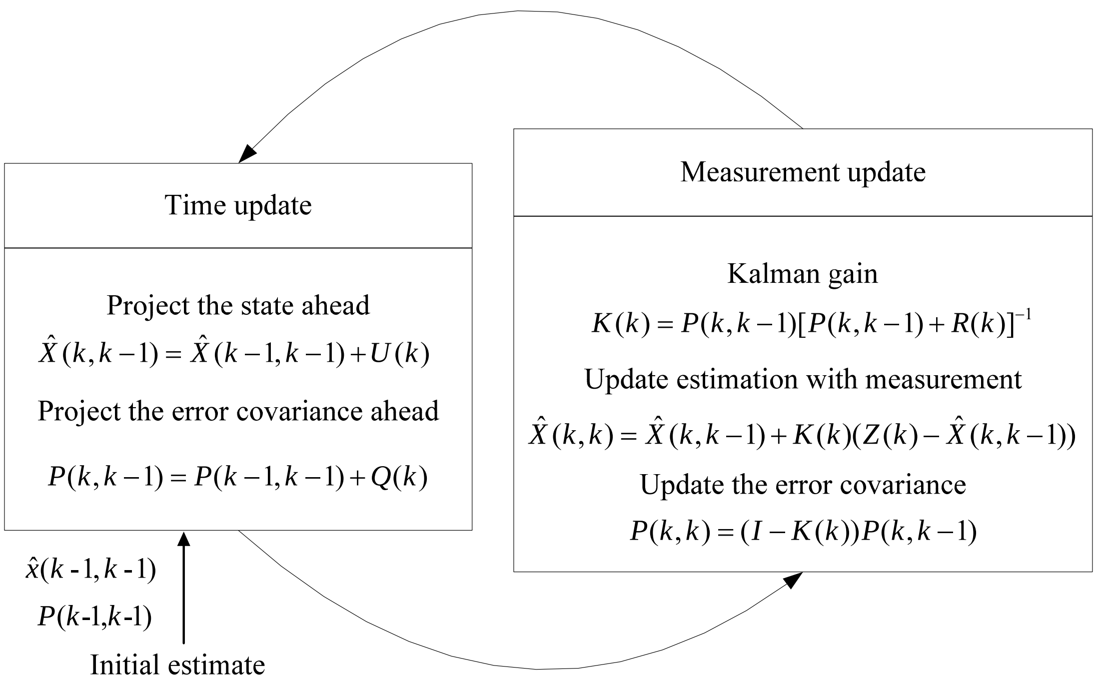

Figure 4.10 A complete implementation of the Kalman Filtering technique

Table 4.3 Calculated settlements of six controlling floors based on FE model at different construction stages (Unit: mm)

Structure	Floor No.	Date								
		18 Oct. 2011	05 Mar. 2012	26 Jul. 2012	04 Sep. 2012	08 Nov. 2012	22 Dec. 2012	15 Mar. 2013	12 May. 2013	04 Dec. 2013
Core wall	4th	–	1.7	1.6	0.5	0.6	0.4	0.8	0.5	1.0
	8th	–	3.5	5.0	0.9	1.3	0.8	1.4	0.9	2.0
	13th	–	4.9	5.6	1.3	2.1	1.2	2.3	1.5	3.2
	22nd	–	–	7.5	2.2	3.4	2.0	3.8	2.4	5.4
	29th	–	–	4.0	3.0	4.6	2.7	5.1	3.3	7.4
	37th	–	–	5.0	4.0	5.3	3.2	6.5	4.1	9.7
Super column	4th	–	2.3	2.4	0.5	0.8	0.4	0.8	0.5	1.0
	8th	–	4.3	6.3	1.0	1.5	0.8	1.5	0.9	2.0
	13th	–	6.0	7.1	1.6	2.4	1.1	2.3	1.5	3.2
	22nd	–	–	7.9	2.7	4.2	2.0	4.1	2.6	5.4
	29th	–	–	8.0	3.6	5.8	2.7	5.5	3.5	7.4
	37th	–	–	–	4.8	7.4	3.5	7.3	4.6	9.7

In Figure 4.10, control vector $U(k)$ is the relative settlement at stage k, due to the increase of the dead load during the construction stage. This settlement at each controlling floors are then calculated by comparing their elevations in the two models. The results are listed in Table 4.3 (5^{th} column). The settlements at other construction stages are similarly calculated and listed in Table 4.3.

The initial elevation of the controlling floors is calculated from the FE analysis and served as the optimal estimate $\hat{X}(0,0)$. The initial error covariance $P(0,0)$ can be obtained after measuring the elevation of initial state $Z(0)$. Here, $P(0,0)$ is assumed as zero because the initial elevation of floor has been adjusted to the optimal estimate such that $Z(0)$ equals $\hat{X}(0,0)$.

In order to achieve the optimal filter, state noise covariance $Q(k)$ and measurement noise covariance $R(k)$ need to be known for calculating the Kalman gain and the optimal estimator's error covariance. Here, $Q(k)$ is mainly induced by the concrete shrinkage and creep as well as the temperature effect. $R(k)$ depends on the accuracy of the measurement instruments, measurement method, and the height of the controlling floor. Regarding the measurement instruments, the total station has a nominal accuracy of 1.0″ and 1 mm ± 1.5 ppm, and the digital level has a nominal accuracy of 1.0 mm. Moreover, the closed traverse measure was used, and the closing error was controlled within 1 mm. Therefore, we assume that $R(0)$ and $Q(0)$ equal to 1 mm^2. A later stages ($k \geq 1$), we assume $Q(k)$ and $R(k)$ are the same as the initial values, because the simulation model and measurement methods remain unchanged.

Again take the core wall of the 8^{th} floor as example. The filtering vectors at different construction stages are listed in Table 4.4. Figure 4.11 shows the changes of the 8th controlling floor's elevation during seven construction stages. It can be seen that the measurement results and FE analysis have a certain difference, which may be caused by various uncertainties including the measurement noise and modeling errors. With the Kalman Filter, the updated values are closer to the measured values, indicating that the updated elevation is closer to the actual elevation of the constructed structure. Both the modeling errors and the measurement noise are filtered out through the filtering process. After updating the elevation of floor at the current construction stage, an estimate elevation at the next stage can be pre-determined, which is more accurate than that is calculated solely via the FE model analysis.

Table 4.4 shows that Kalman gain $K(k)$ and covariance of the updated results $P(k,k)$ converge rapidly after several stages, when $Q(k) = R(k) = 1\ \mathrm{mm}^2$. We then investigate the effect of the error covariance on the Kalman filter results, as shown in Table 4.5. When the measurement error is larger than the system error significantly, i.e., $R(k) >> Q(k)$, the Kalman gain is small. Consequently, the updated elevations are close to the numerical calculations. On the contrary, when $R(k) << Q(k)$, the Kalman gain is large and the updated elevation results approach to the measurement data. This can be verified in Figure 4.12, which shows the updated elevation of the super column at the 8th floor when different error covariances are used. Under the precondition of $P(0,0) = 0$, the Kalman gain is 0.618 when the two kinds of error are identical ($R(k) = Q(k)$), regardless $Q(k)$ and $R(k)$ are equal to 1 mm^2 (Case 3 in Table 4.5), or other values (such as 10 mm^2).

We then set $Q(k) = R(k)$ in the Kalman Filtering analysis hereinafter. Initial covariance $Q(0)$ of other controlling floors is assumed to have a linear proportion to the height of the floors, that is, upper floors have larger measurement error. So does $R(0)$.

Table 4.4 Filtering results for the core wall of the 8th floor at different construction stages

Vector	Initial Value	Date of Construction Stage							
		05 Mar. 2012	26 Jul. 2012	04 Sep. 2012	08 Nov. 2012	22 Dec. 2012	15 Mar. 2013	12 May. 2013	04 Dec. 2013
k	0	1	2	3	4	5	6	7	8
$Q(k)$ (mm^2)	1.0	1.0	1.0	1.0	1.0	1.0	1.0	1.0	1.0
$R(k)$ (mm^2)	1.0	1.0	1.0	1.0	1.0	1.0	1.0	1.0	1.0
$P(k,k\text{-}1)$ (mm^2)		1.0	1.5	1.6000	1.6154	1.6176	1.6180	1.6180	1.6180
$K(k)$		0.5	0.6	0.6154	0.6176	0.6180	0.6180	0.6180	0.6180
$P(k,k)$ (mm^2)	0	0.5	0.6	0.6154	0.6176	0.6180	0.6180	0.6180	0.6180
$U(k)$ (mm)		3.5	5.0	0.9	1.3	0.8	1.4	0.9	2.0
$Z(k)$ (m)		38.2828	38.2761	38.2757	38.2751	38.2740	38.2729	38.274	38.2737
$\hat{X}(k,k)$ (m)	38.2864	38.2829	38.2768	38.2758	38.2749	38.2740	38.2728	38.2732	38.2712
$\hat{X}(k,k-1)$ (m)		38.2829	38.2779	38.2759	38.2745	38.27410	38.2726	38.2719	38.2712

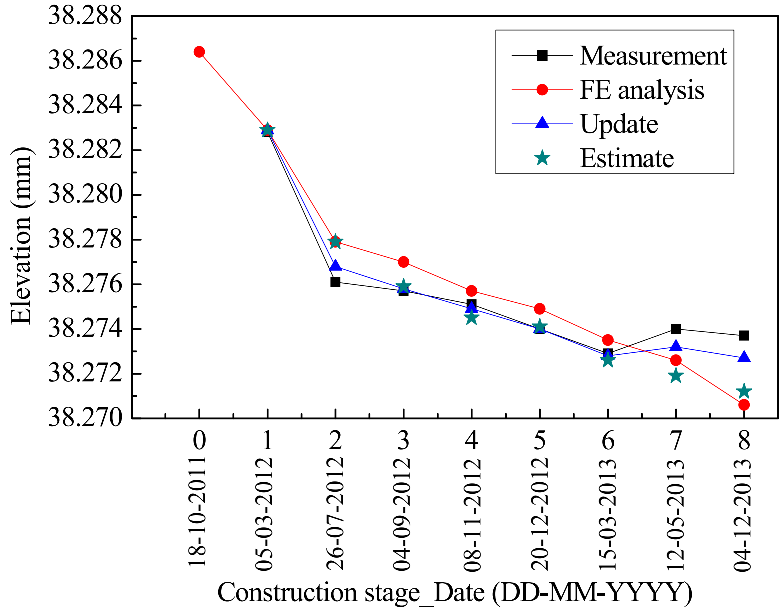

(a) Core wall

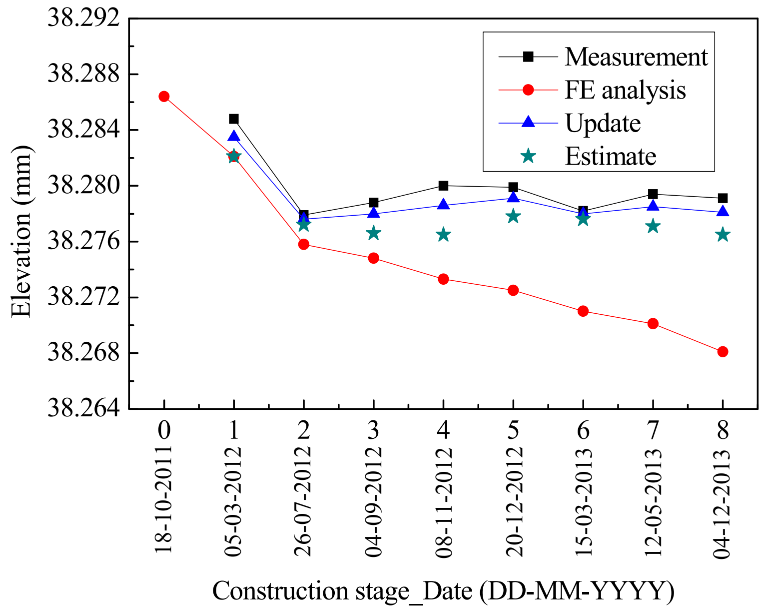

(b) Super column

Figure 4.11 Kalman filter analysis of elevation at the 8th floor

Table 4.5 Kalman gain when different covariances are used

Date		05 Mar. 2012	26 Jul. 2012	04 Sep. 2012	08 Nov. 2012	22 Dec. 2012	15 Mar. 2013	12 May. 2013	04 Dec. 2013
k		1	2	3	4	5	6	7	8
Case 1	$Q(k)$	1	1	1	1	1	1	1	1
	$R(k)$	100	100	100	100	100	100	100	100
	$K(k)$	0.0099	0.0195	0.0287	0.0372	0.0451	0.0522	0.0586	0.0642
Case 2	$Q(k)$	1	1	1	1	1	1	1	1
	$R(k)$	10	10	10	10	10	10	10	10
	$K(k)$	0.0909	0.1603	0.2065	0.2346	0.2507	0.2597	0.2645	0.2671
Case 3	$Q(k)$	1	1	1	1	1	1	1	1
	$R(k)$	1	1	1	1	1	1	1	1
	$K(k)$	0.5	0.6	0.6154	0.6176	0.6180	0.6180	0.6180	0.6180
Case 4	$Q(k)$	10	10	10	10	10	10	10	10
	$R(k)$	1	1	1	1	1	1	1	1
	$K(k)$	0.9091	0.9160	0.9161	0.9161	0.9161	0.9161	0.9161	0.9161
Case 5	$Q(k)$	100	100	100	100	100	100	100	100
	$R(k)$	1	1	1	1	1	1	1	1
	$K(k)$	0.9901	0.9902	0.9902	0.9902	0.9902	0.9902	0.9902	0.9902

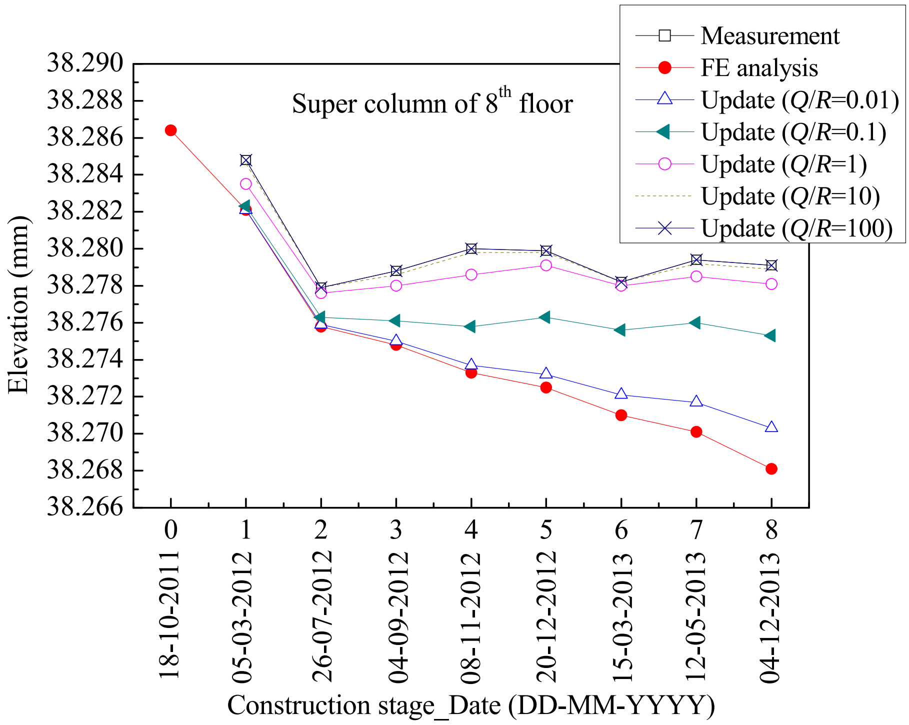

Figure 4.12 Updated elevation results when different error covariances rates are used

Using the same procedure as above, the filtering elevation of other controlling floors are calculated and plotted in Figure 4.13 ~ Figure 4.17. Analysis of each controlling floor starts from the date when the measurement was made at the first time. The filtering results similarly show that the updated results approach to the measurements in general. In some cases, for example, the elevation measurement of the 29th floor went up slightly from 8 Nov. 2012, possibly due to measurement error during the measurement operation. The present method includes the FE analysis and considers various uncertainties. The results are more realistic and accurate.

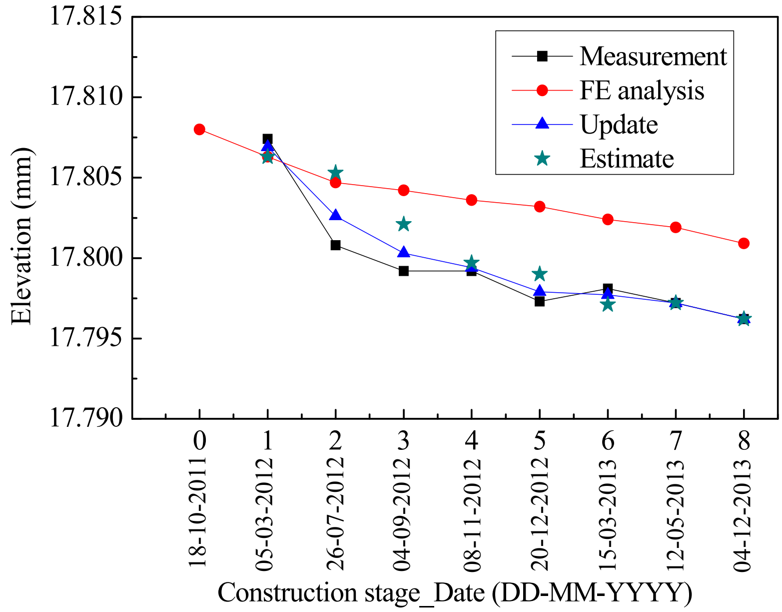

(a) Core wall

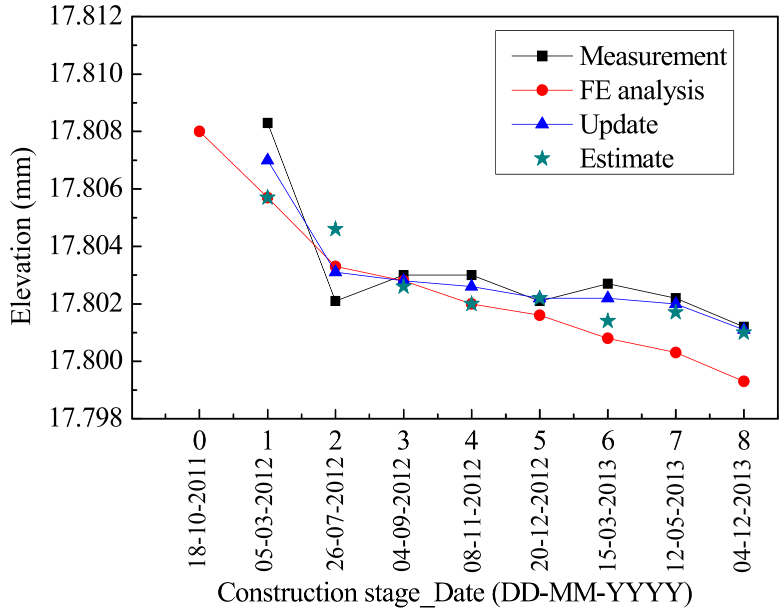

(b) Super column

Figure 4.13 Elevation of the control point at the 4th floor

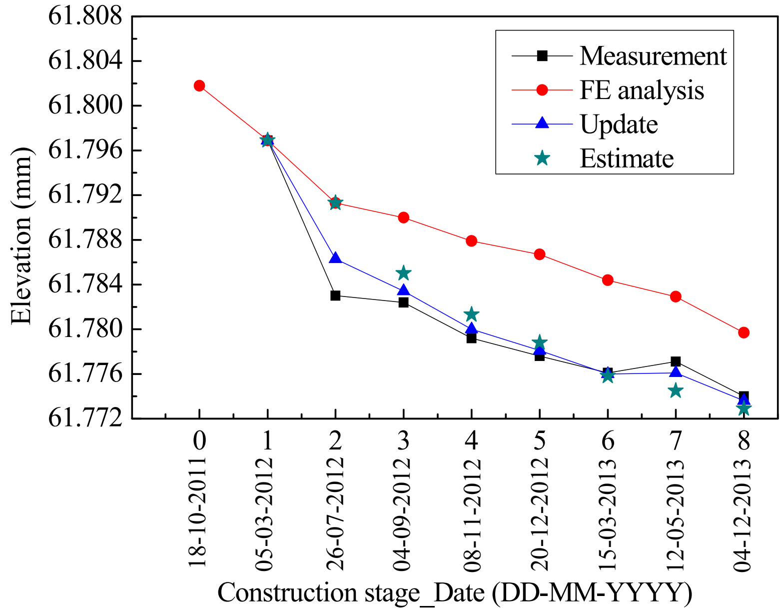

(a) Core wall

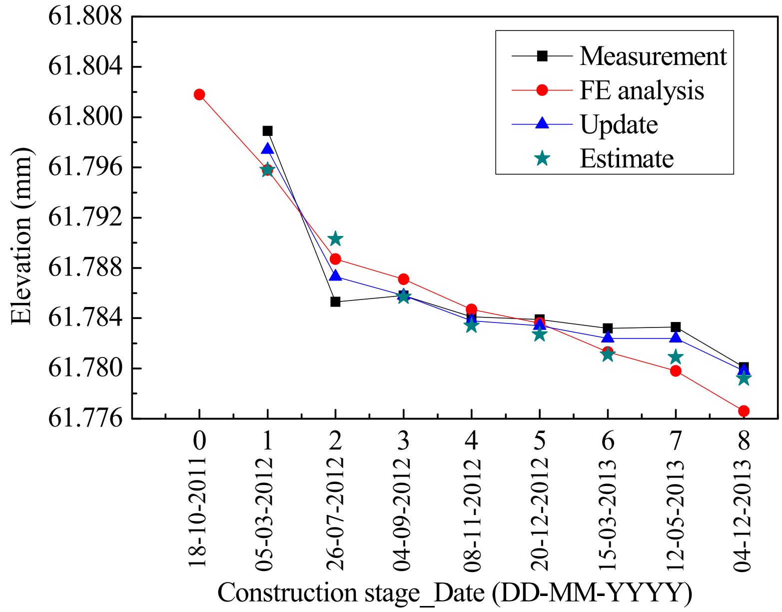

(b) Super column

Figure 4.14 Elevation of the control point at the 13th floor

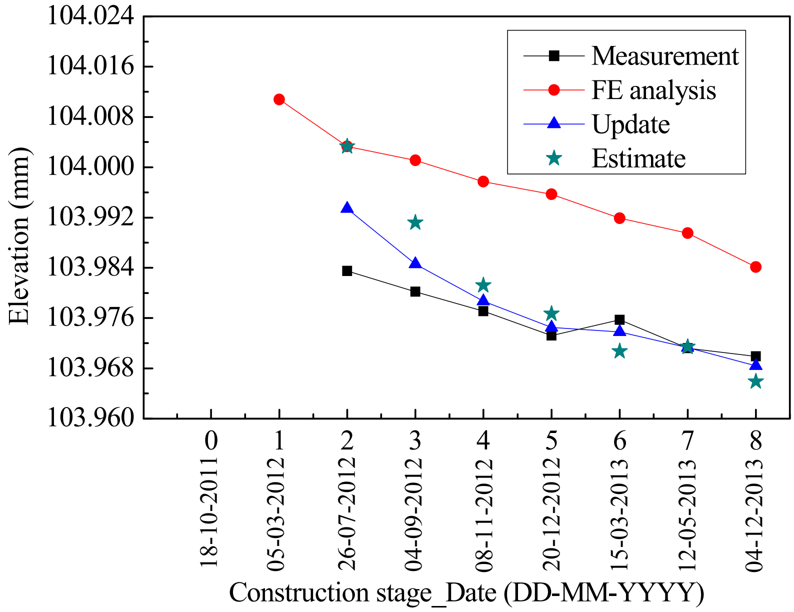

(a) Core wall

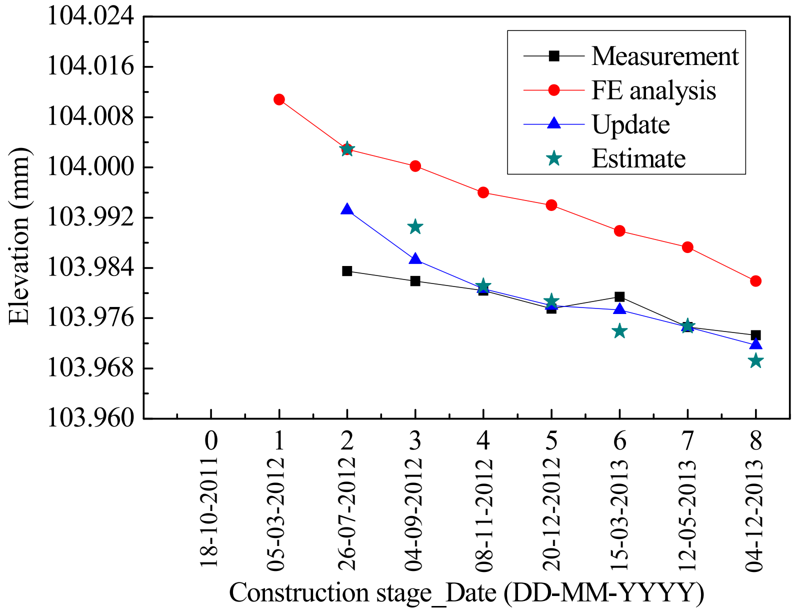

(b) Super column

Figure 4.15 Elevation of the control point at the 22nd floor

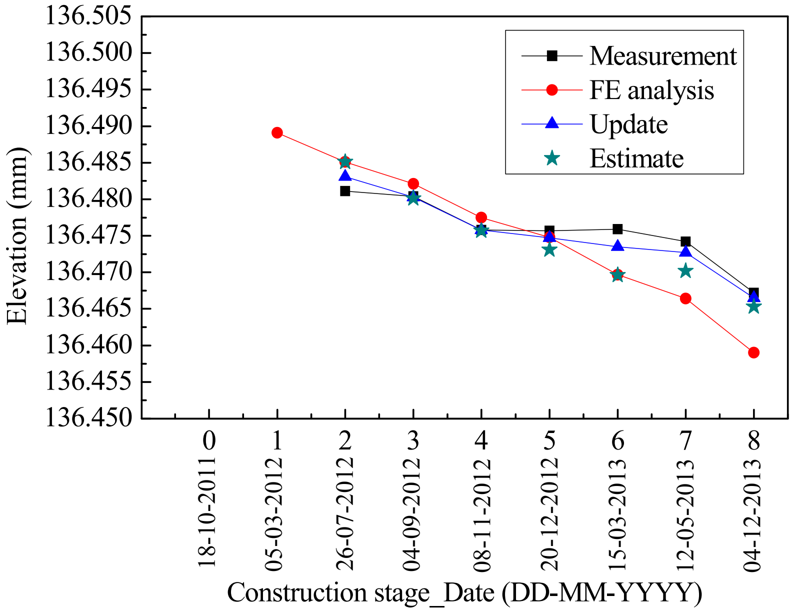

(a) Core wall

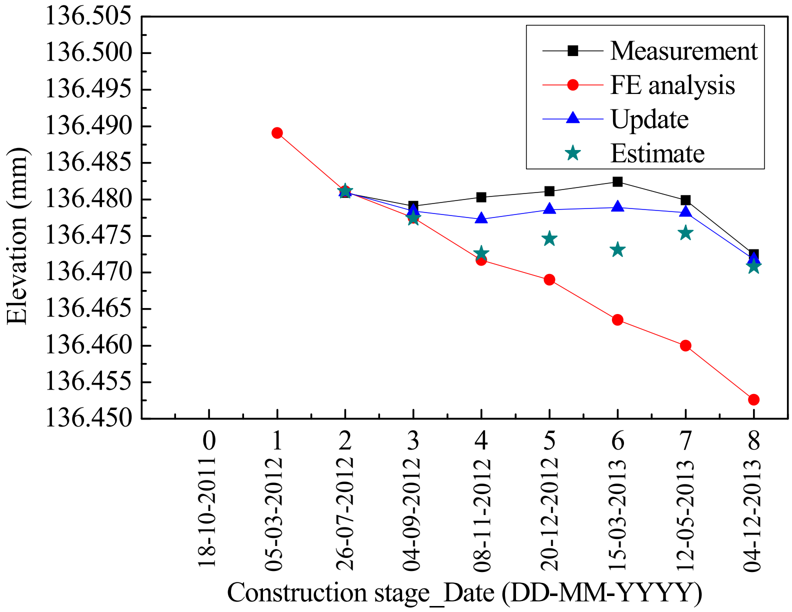

(b) Super column

Figure 4.16 Elevation of the control point at the 29th floor

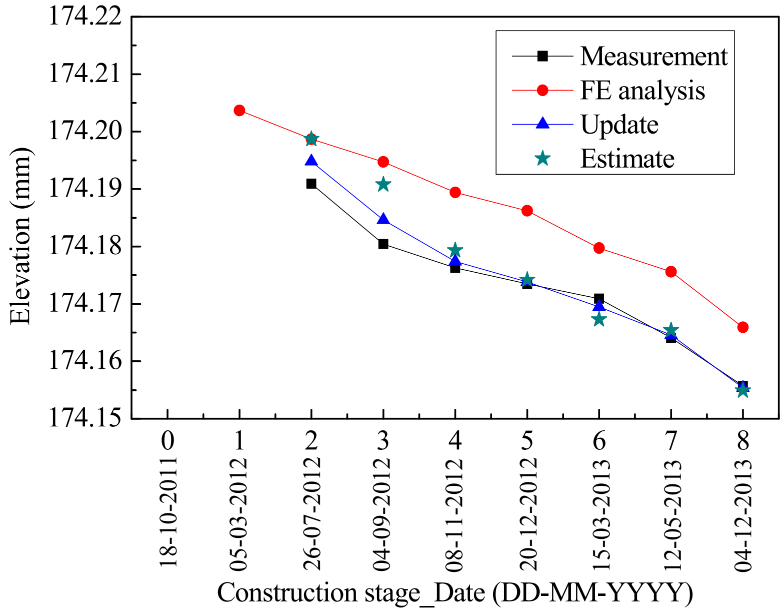

(a) Core wall

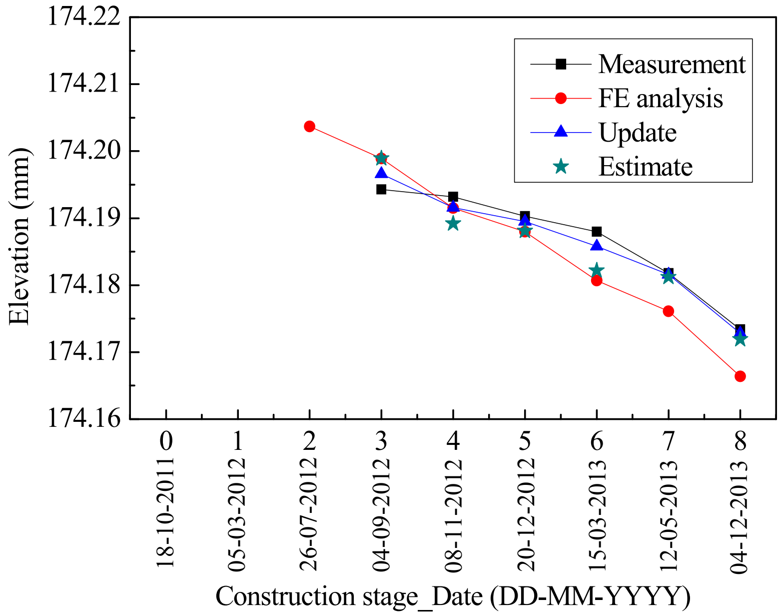

(b) Super column

Figure 4.17   Elevation of the control point at the 37th floor

4.4 Summary

The construction precision of supertall structures is very critical to ensure the safety and serviceability of the completed structures. Ever changing loadings and environmental factors make the construction positioning very difficult and the constructed structure may deviate from the design significantly. This chapter has proposed a construction settlement monitoring method integrating the Kalman Filtering approach and the FE forward construction stage analysis, and applied it to the 632-m tall Shanghai Tower.

With the Kalman Filtering method, the modelling errors and the measurement noise are filtered out. The updated results consider both the construction load effects and various uncertainties. Consequently, the results are more realistic and accurate for analysing the floors' pre-determined height of supertall buildings. The initial state parameters and the noise covariance may affect the filtering results to some degree. The present method can be extended to the construction control for positioning key components of the structure.

CHAPTER FIVE

TEMPERATURE DISTRIBUTION OF CANTON TOWER BASED ON LONG-TERM FIELD MONITORING

In this chapter, the long-term monitoring data of the Canton Tower over seven years from 2008 to 2014 will be employed to study the temperature distribution of the structure. In particular, the temperature difference between the inner and outer tubes, and the temperature difference between different facades of structure, will be detailed.

5.1 Deployment of Temperature Sensors

As mentioned in Chapter Three, a total of 12 cross-sections at different heights have been selected for temperature monitoring. Figures 5.1(a) and 5.1(b) show the layout of the sensors on Sections 3 and 12, respectively. The latter has a functional floor enclosed by the curtain wall, whereas the former not. At each of Point 1 ~ Point 4 on the monitoring sections of the inner tube, one thermistor was embedded in the middle of the concrete core wall. Point A ~ Point D at each section of the outer tube were also installed with temperature sensors. Each CFT column has two PT100 temperature sensors attached on the steel surface, one facing to the inner tube and the other to outward, as shown in Figure 5.1(c). From Sections 6 to 12, one thermistor was embedded in the concrete of the CFT column, which was located at one-third of the radius from the column surface. It is noted the plan locations of Points A to D vary as the height of the CFT columns increases.

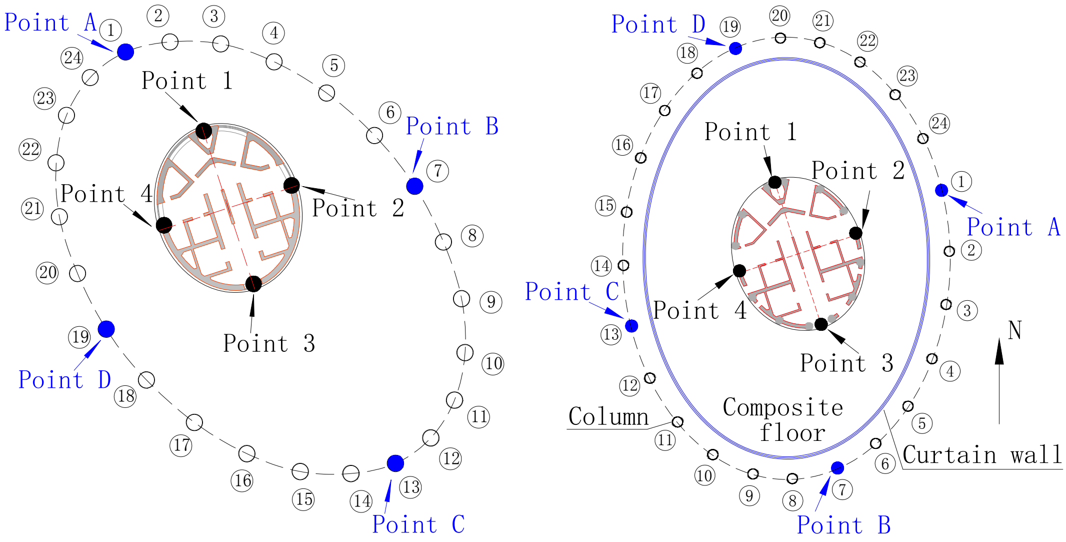

(a) Section 3 (b) Section 12

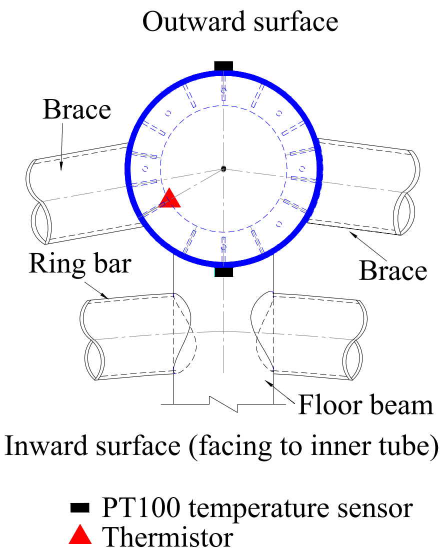

(c) Plan view of CFT

Figure 5.1 Layout of sensors on monitoring sections

A series of 20 PT100 temperature sensors were embedded into the RC wall along the thickness direction with equal spacing on Section 12 to measure the temperature gradients of walls during the construction stage. These sensors were installed at Point 1 to Point 4, each with five, as shown in Figure 5.2.

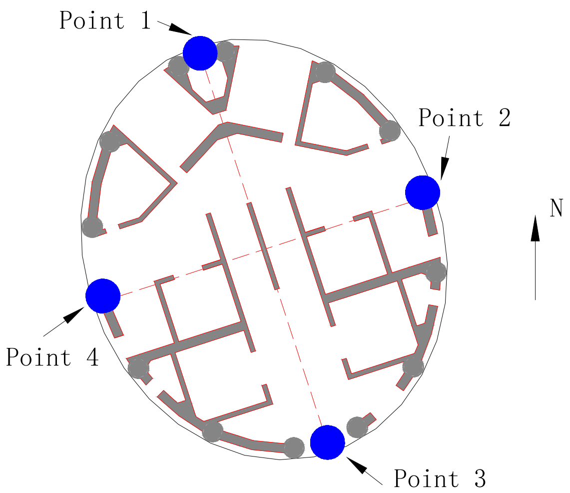

(a) Measurement points

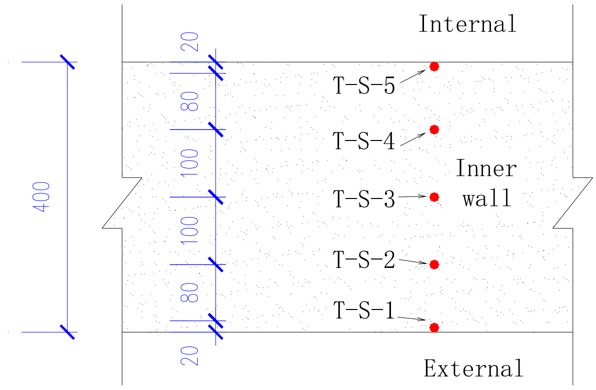

(b) Temperature sensors on the southern wall

Figure 5.2 Layout of temperature sensors on Section 12 (unit: mm)

Each of the sensors is conveniently labelled as T-Y-Z, in which the first alphabet (T) indicates the PT100 Platinum resistance temperature sensor, the second indicates the position of the inner wall (E, S, W and N denote east, south, west and north side respectively), and the last digit denotes the sensor location (1 to 5 represent from the external surface to internal surface of the wall, respectively). For example, tag T-S-1 denotes the temperature sensor located at the external surface of core wall in southern direction. Figure 5.3 illustrates the deployment of all temperature sensors on the inner RC structure and the outer CFT columns of the Canton Tower.

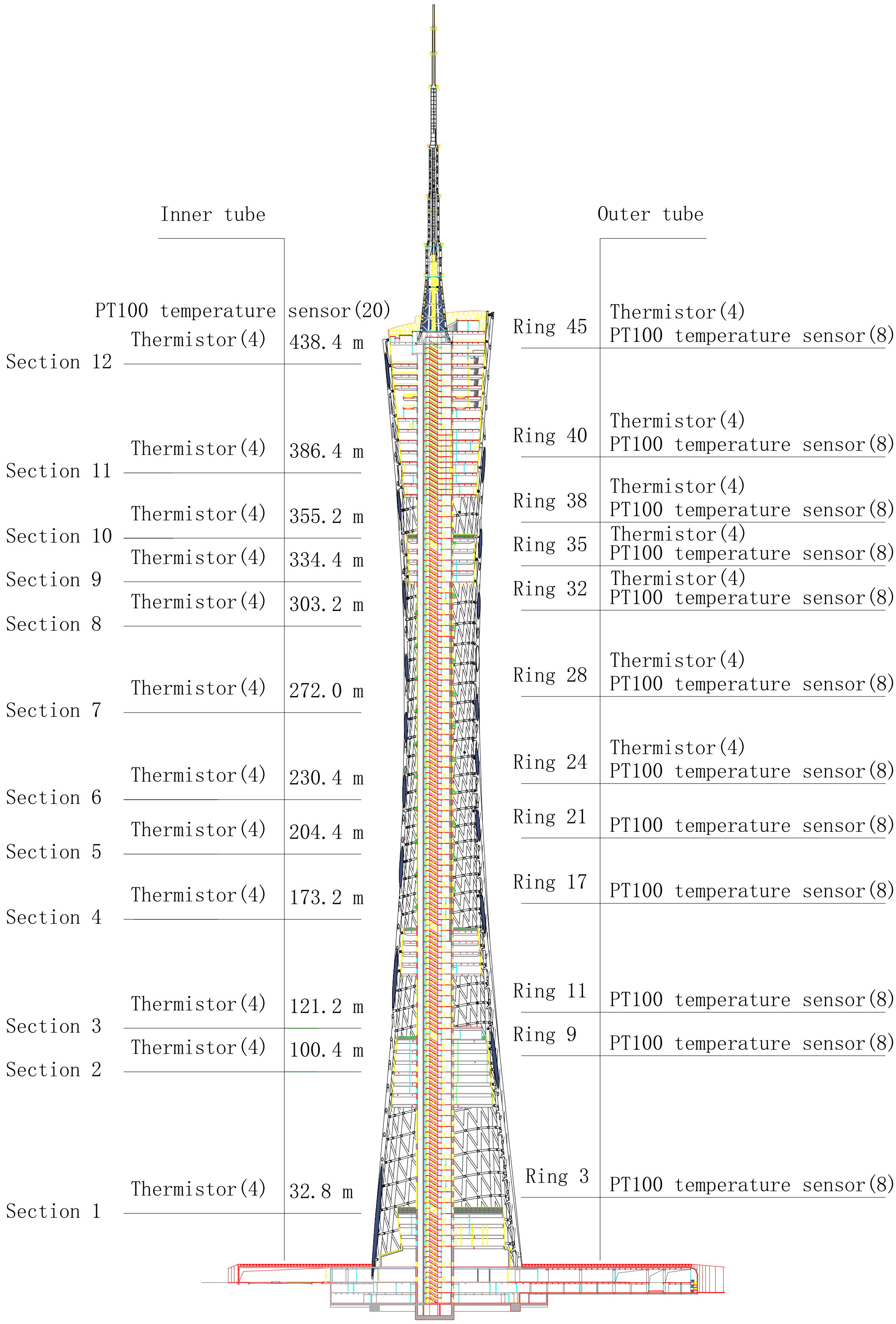

Figure 5.3 Deployment of temperature sensors for the Canton Tower

5.2 Temperature Measurement Data

The temperature data of the 12 monitoring sections were acquired, transmitted, and stored automatically by the SHM system.

5.2.1 Annual Temperature Variation

Figure 5.4 shows daily maximum and minimum ambient air temperature data from 2008 to 2014, which was retrieved from a weather station in Guangzhou Baiyun International Airport, about 30 km from the Canton Tower. The annual air temperature in this weather station is complete with the accuracy of 1.0℃. The measured temperature at Point 4 of Sections 3 and 9 during the period is shown in Figure 5.5. It is noted that the period covers the construction stage (from January 2008 to August 2010) and service stage (August 2010 afterwards) of the structure. Some data missed in some instances, mainly because of shut down of the data acquisition system.

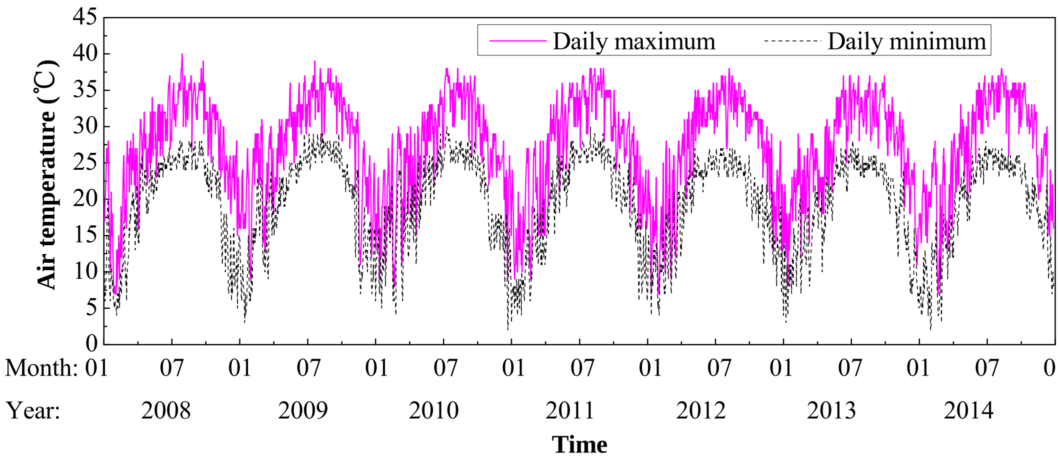

Figure 5.4 Daily maximum and minimum ground air temperature from 2008 to 2014

The measured temperature data have a similar variation pattern in each year with high temperature in summer and low temperature in winter for both sections. The inner wall at Section 3 is exposed to the ambient air and solar radiation while that at Section 9 has been enclosed by curtain wall since the year of 2010, when the construction completed. Therefore, the temperature fluctuation at Section 9 is smaller than that of Section 3 from then on (Figure 5.5). For example, the minimal and maximal temperature of Point 4 at Section 9 are 11.0°C and 29.1°C, respectively, in 2014, while those of Point 4 at Section 3 are 8.2°C and 32.5°C.

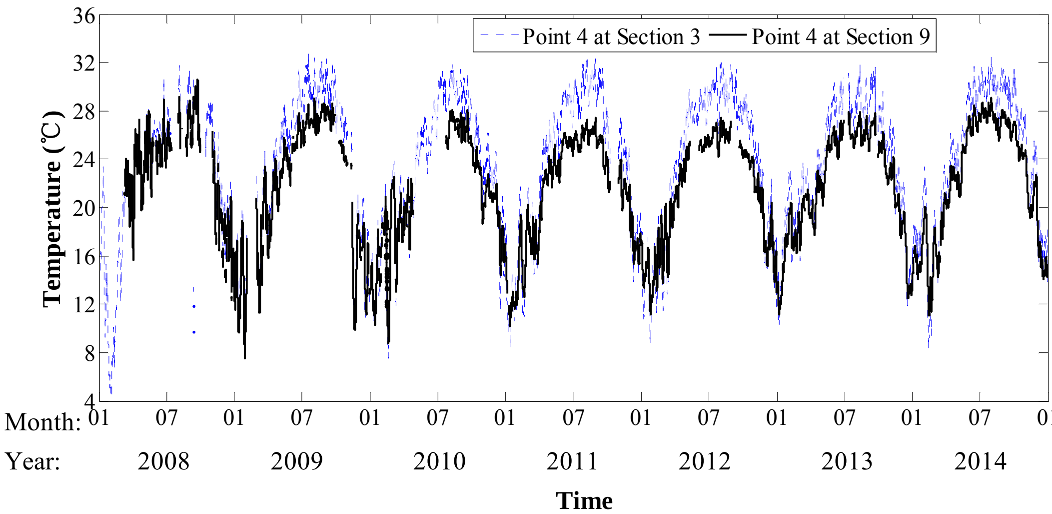

Figure 5.5 Measured temperature of inner wall from 2008 to 2014

All temperature sensors on the outer tube started collecting data from August 2010. Figure 5.6 illustrates the measured temperature of CFT (Point C) at Section 9. The overall variation pattern of temperature inside the concrete is similar to that of the steel surface. However, the temperature variation range inside the concrete is less than that of the steel surface because concrete has a small heat conductivity. In summary, structural temperature ranges from 2.5 to 29.2℃ for the concrete, and 3.1 to 34.8°C for the steel surface, in 2014.

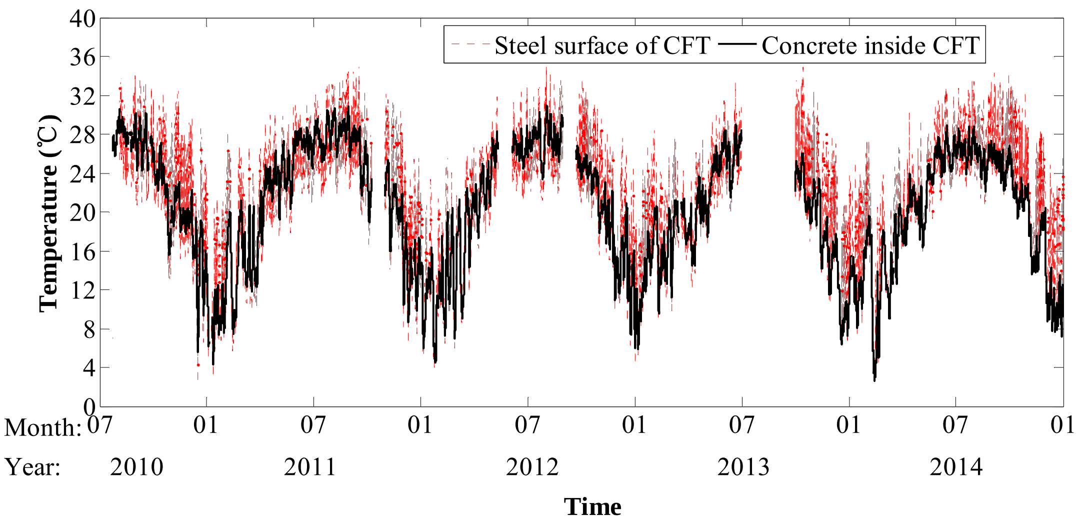

Figure 5.6 Measured temperature of CFT (Point C) at Section 9

5.2.2 Monthly Temperature Variation

The structural temperature of Sections 3 and 9 in the summer (August) of 2012 is shown in Figure 5.7. The daily ground air temperature and the daily average temperature in the month are also shown in Figure 5.7, which are obtained from a weather station about 6 km away from the Canton Tower, with the accuracy of 0.1°C.

Figure 5.7(a) shows that in summer the maximum daily variation of the ground air temperature is about 8°C. The air temperature is averaged per each day and its change in two successive days is less than 3°C. Temperature of the inner wall at Section 9 is consistently lower than Section 3 by 3 ~ 5°C because of indoor air conditioning in Section 9. The daily temperature of the steel surface has a good correlation with the air temperature, while temperature of the inner wall and concrete inside the CFT correlate well with the daily averaged ambient temperature.

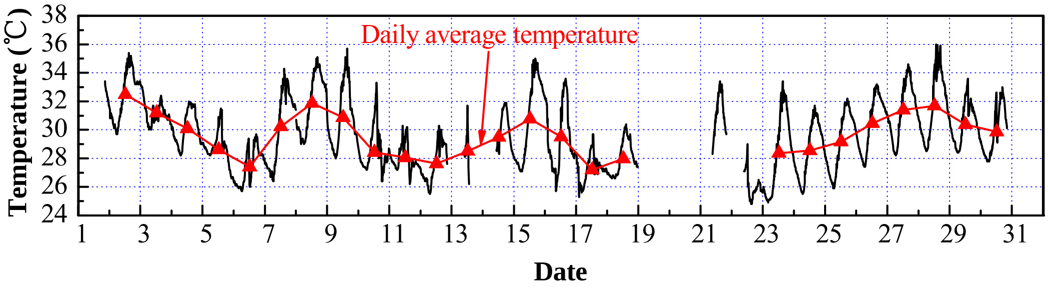

(a) Ground air temperature

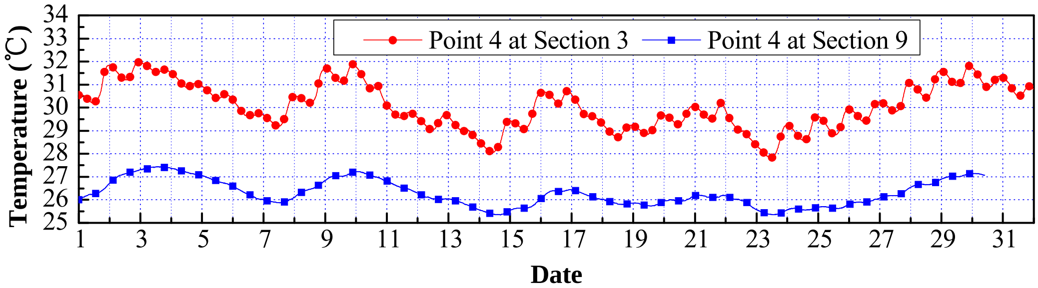

(b) Inner wall

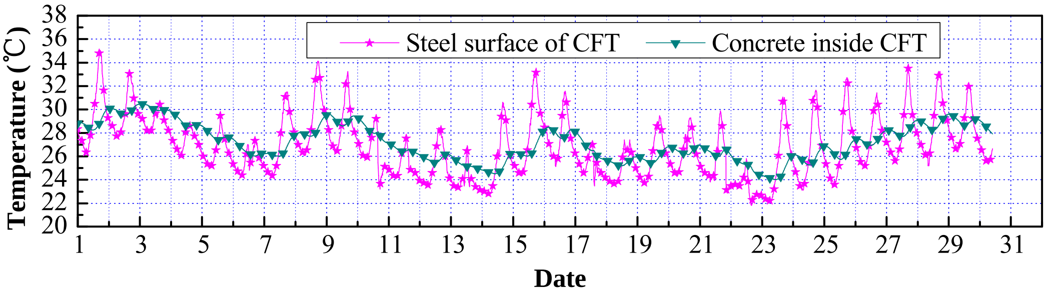

(c) Outer column (Point C) at Section 9

Figure 5.7 Temperature of inner wall and outer column in August 2012

The structural temperature and air temperature in winter (January) of 2012 are shown in Figure 5.8. The daily air temperature in winter fluctuates more irregularly and significantly, as compared with summer. For example, the daily averaged air temperature may drop down by 6°C or rise up by 3°C in two successive days. The maximum daily variation is approximately 8°C. The inner walls at Section 9 and Section 3 have similar temperature on most days of the month. Temperature at the steel tube surface has a high correlation with the air temperature, and temperature of concrete inside the CFT correlates well with the daily averaged ambient temperature, both are similar with those in summer.

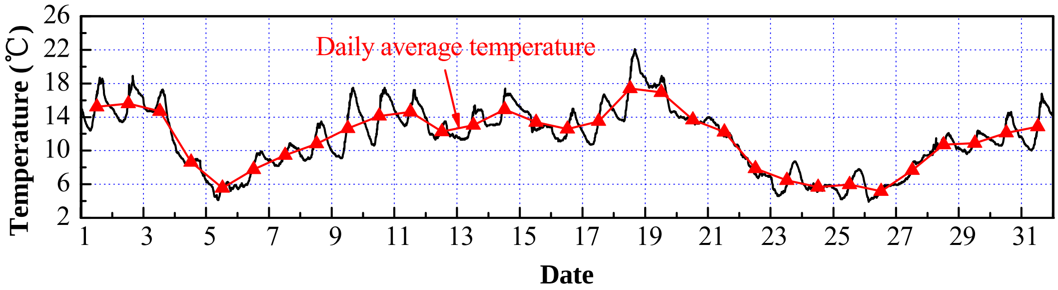

(a) Ground air temperature

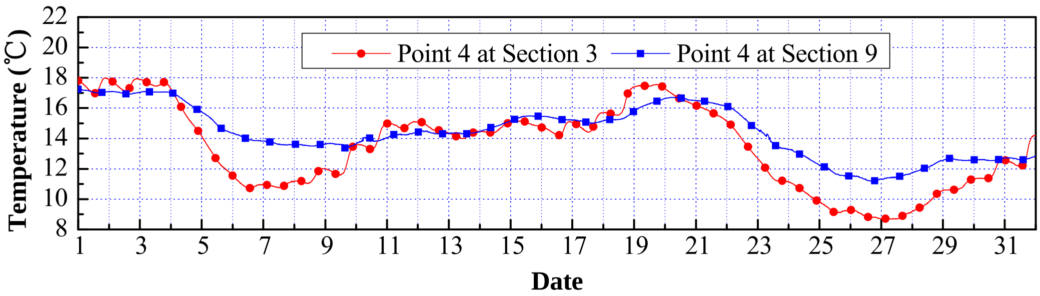

(b) Inner wall

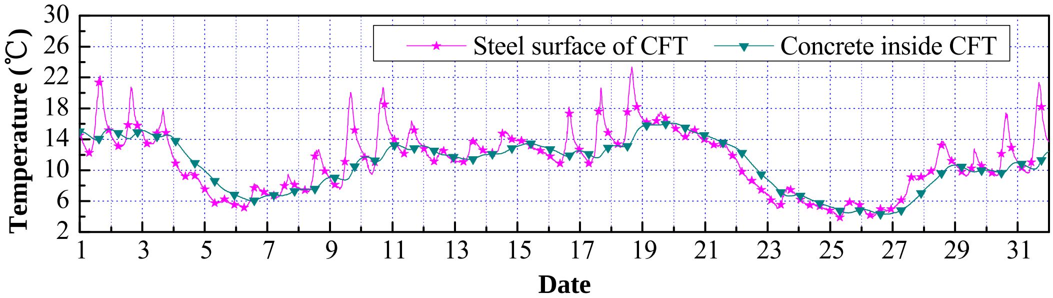

(c) Outer column (Point C) at Section 9

Figure 5.8 Temperature of inner wall and outer column in January 2012

5.2.3 Daily Temperature Variation

Figure 5.9 shows temperature of the inner wall and the steel surface of outer column at Sections 3 and 9 on two successive sunny days in summer and winter. The air temperature data on these two days are also shown in the figure as a reference. It is observed that the ambient temperature and the CFT surface temperature had a well-correlated variation cycle in the two seasons, although different components reach the maximum temperature at different time instants. The daily temperature fluctuation of the inner wall (Point 4) is very small because the sensors were installed inside the inner wall. In particular, Point 4 of Section 9 almost has constant temperature as the section is enclosed by curtain wall.

As for the steel surface of the CFT column at Section 3 (at 121.2 m), temperature of the steel surface has one hour delay in comparison with the ambient temperature, and the daily variation is about 8.5°C in summer and 11.6°C in winter, higher than the variation of air temperature (6.0°C in summer and 8.0°C in winter). In addition, temperature of the steel surface of CFT at Section 9 (at 334.4 m) is lower than that at Section 3 by about 2°C. The lowest temperature of the CFT surface at Section 9 is also lower than that of the ground air temperature. This may be because air temperature varies with respect to the elevation, which is investigated in the next section.

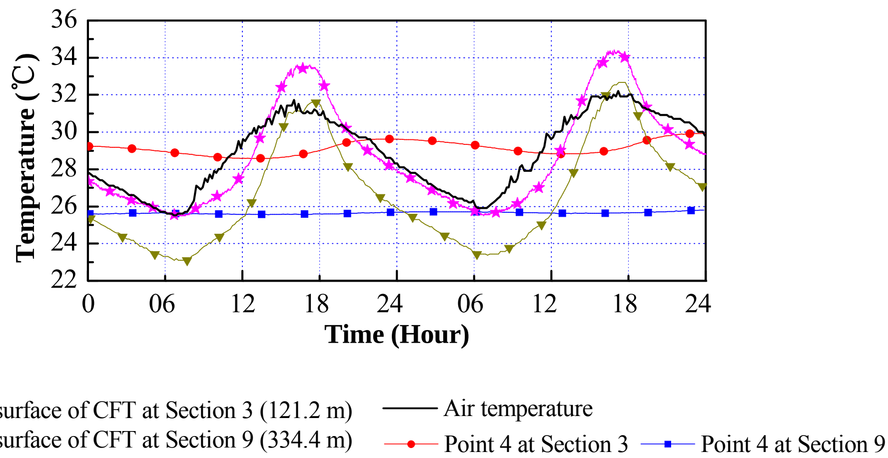

(a) On 24-25 August 2012

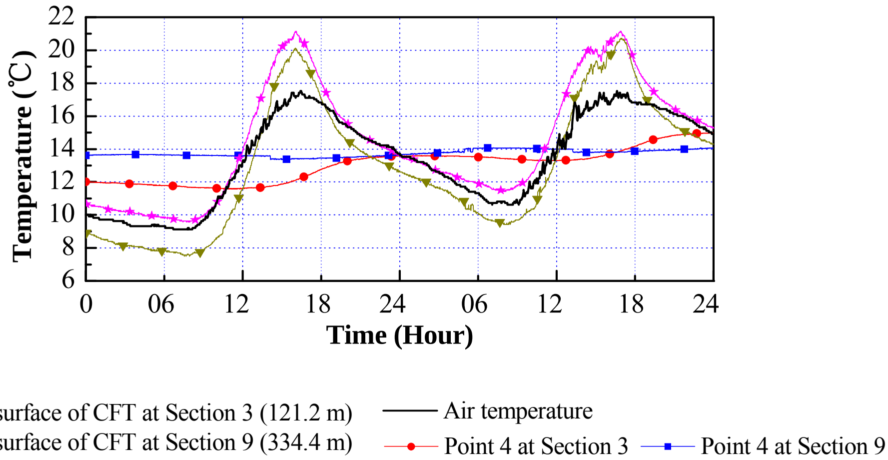

(b) On 9-10 January 2012

Figure 5.9 Daily temperature variation of inner wall and outer column

It is noted that temperature of the exterior surface of the steel CFT columns is not very high, even in summer. For example, the highest temperature of the steel surface is about 34.5°C on 25 August 2012 while the air temperature is 32°C. This is because the steel CFT columns, beams, and bracings are coated with several layers painting at approximately 1 mm thick in total. The white painting material has a low absorptivity coefficient (0.2 ~ 0.3) and very small thermal conductivity (Ma et al. 1986; Liu 2010; Howell *et al.* 2011), providing the steel components with a good temperature isolation from the ambient temperature environment.

5.2.4 Ambient Air Temperature

Past studies have shown that ambient air temperature is associated with the altitude and the relative air humidity. For example, it shows that, under normal atmospheric condition, the average air temperature decreases by 6.5°C as the altitude increases 1000 m (Jacobson 2005), and this value may be affected by the moisture content of the air.

Figure 5.10 displays the ground air temperature measured at the altitude of 48 m and the top of the tower (about 465 m) in summer (September 2013) and winter (December 2014). The ground air temperature is higher than the air temperature at the top of the tower in both seasons.

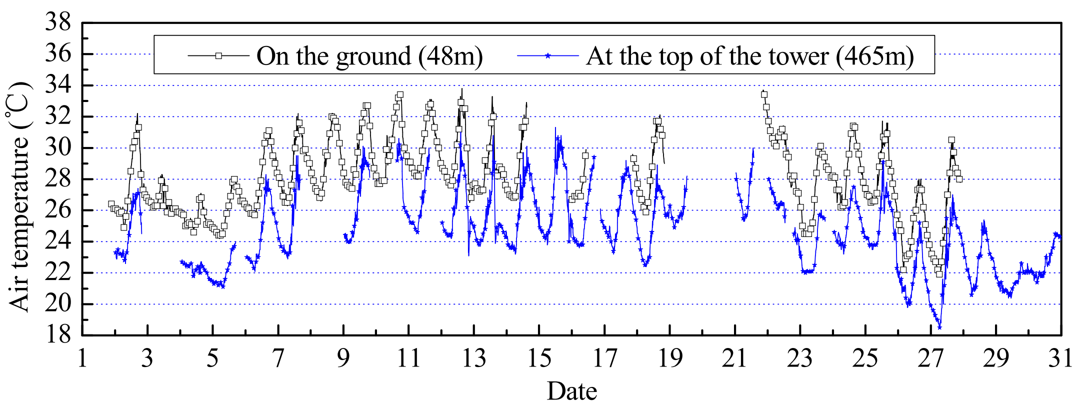

(a) September 2013

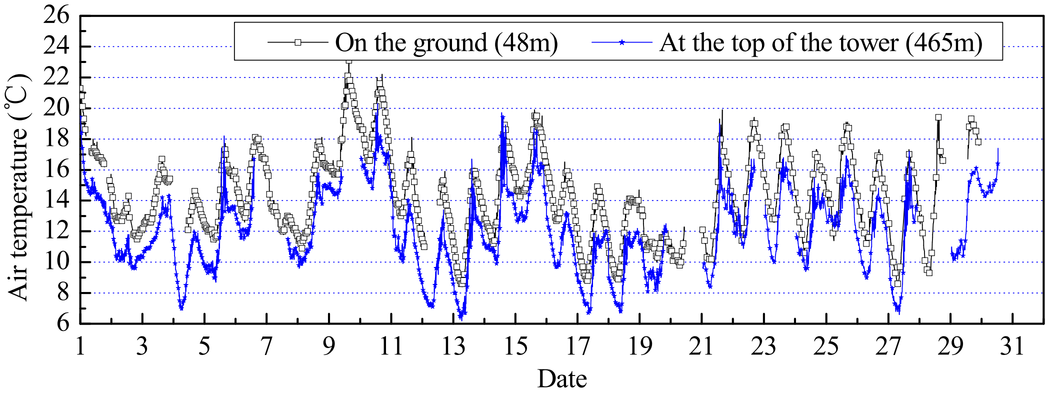

(b) December 2014

Figure 5.10 Ambient air temperature at different height

The relation of these two sets of temperature is plotted in Figure 5.11. The two quantities show a very good linear correlation with the correlation coefficient of 0.9563 in summer and 0.9483 in winter. A linear analytical function between them is taken as

$$T_{tw} = a \cdot T_{gr} + b \tag{5.1}$$

where T_{tw} and T_{gr} represents the air temperature at the tower top and ground, respectively, b is the intercept, and a is the slope factor. For simple, a is set as 1. With the least-squares fitting, intercept is obtained as b = –3.3556 in summer and b = –2.2080 in winter, indicating the air temperature at the tower top is lower than the air temperature near the ground by about 3.4°C in summer and 2.2°C in winter. The intercept b in summer and winter are different because of the difference in air humidity. The averaged temperature decrease rate is 2.8°C /417 m = 6.7°C / km, similar to 6.5°C / km suggested by Jacobson (2005).

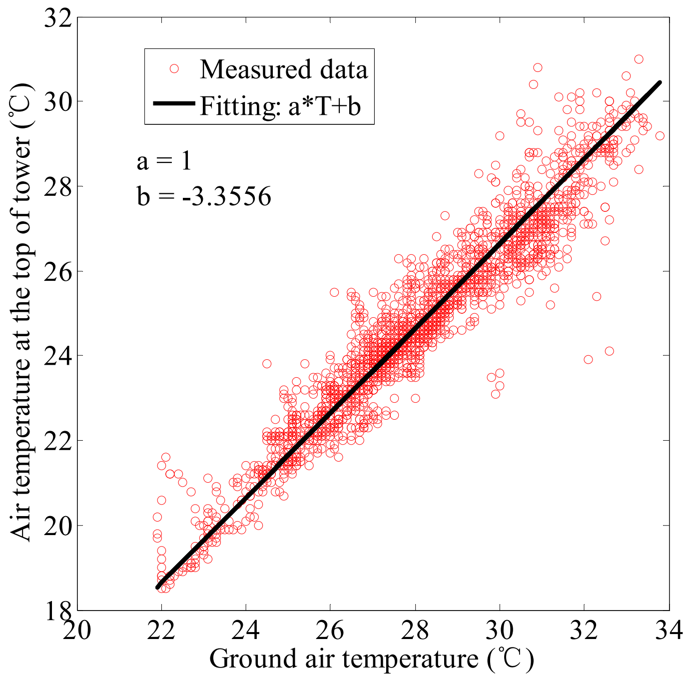

(a) September 2013

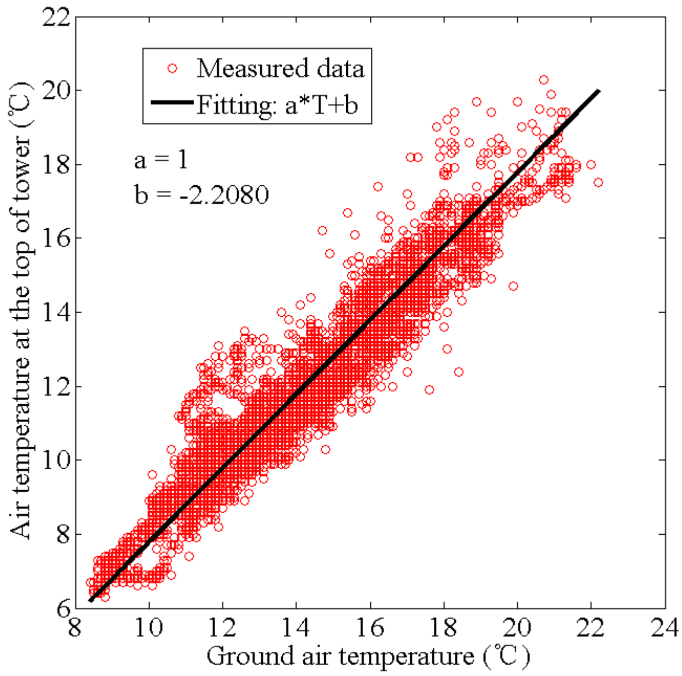

(b) December 2014

Figure 5.11 Relationship between the ground air temperature and the air temperature at the tower top

5.3 Temperature Distribution of the Canton Tower

The measured temperature data show that temperature of the inner wall and outer columns of the Canton Tower is different. So does temperature of different outer columns. Therefore, the temperature difference between the inner and outer tubes and the temperature difference between different facades of the inner core wall and outer columns will be studied in this section.

5.3.1 Effective Temperature of Main Components

Temperature distribution along the thickness of the RC core wall is not uniform. So does the CFT columns. The effective temperature is thus employed for simplicity. The effective temperature is an area-weighted average temperature of the cross-section of the structural component (Li *et al.* 2004a; Zhou *et al.* 2010). For example, an area A consists of several subareas A_i (i = 1, 2, …, k) each with average temperature $\overline{T}_i$, then the effective temperature of the component is calculated as

$$T_e = \sum_{i=1}^{k} \frac{A_i}{A} \overline{T}_i \tag{5.2}$$

For the Canton Tower, temperature at Points 1 ~ 4 is treated as the effective temperature of the inner core walls facing to north, east, south and west, respectively, since only one thermistor sensor was installed at the middle thickness of the wall at each point.

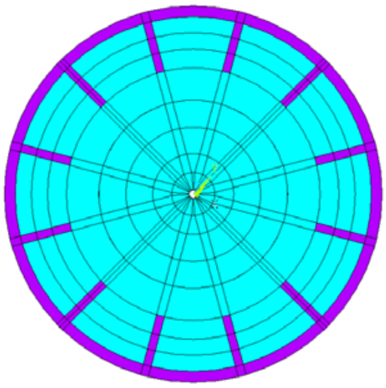

(a) FE model of CFT column

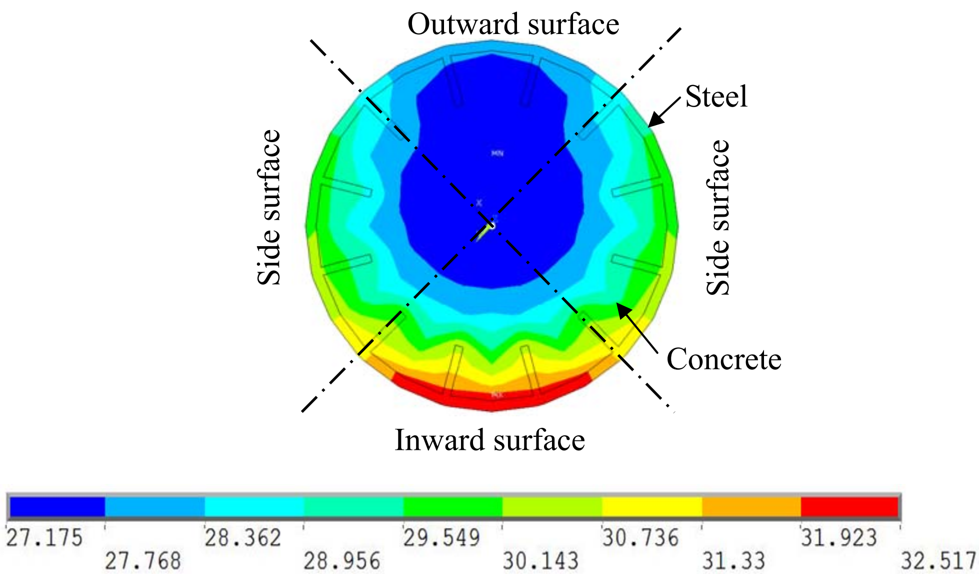

(b) Temperature contour

Figure 5.12 FE model and heat-transfer analysis of CFT column

As for the CFT columns, the steel surface and inside concrete have different temperature distribution. In view of difficulty in measuring the detailed temperature distribution of CFT columns by a few sensors, the numerical counterpart can be obtained through a heat-transfer analysis. In this regard, the FE model of a typical column section at Point C of Section 8 is constructed in ANSYS (ANSYS 10.0 2005) and shown in Figure 5.12(a). The FE model consists of 400 nodes and 360 two-dimensional Plane55 elements. Plane55 has four in-plane nodes each with a single degree of freedom (DOF) of temperature. The CFT steel surface is divided into four regions: outward surface, inward surface, and two side surfaces, according to their orientations.

The first kind thermal boundary condition (Equation (2.4)) is applied. In particular, temperature on the outward and inward surfaces use the real temperature measured from the two surface temperature sensors, those of two side surfaces use the average temperature of the inward and outward surfaces. The main material properties are summarized in Table 5.1 (Howell *et al.* 2011). With the transient heat-transfer analysis in ANSYS, temperature variation of the column at different time instants is obtained. Figure 5.12(b) shows the temperature contour of the section at 15:00 on 4 August, 2011. It can be seen that the temperature distributes non-uniformly with an approximate 5.3°C difference between the steel surface and concrete inside.

Table 5.1 Material parameters of the column for thermal analysis

Parameters	Steel	Concrete
Density (kg/m^3)	7850	2400
Heat capacity (J/(kg°C))	460	925
Thermal conductivity (W/(m°C))	60	2.71
Emissivity coefficient	0.80	0.88
Absorptivity coefficient	0.75	0.65

The obtained temperature inside the concrete is compared with the measurement counterpart (the measurement point is shown in Figure 5.1 (c)) in Figure 5.13. The numerical result agrees well with the field measurement with a difference less than 0.5°C, which verifies the effectiveness of the heat-transfer analysis.

According to the simulated temperature data at each point, the effective temperature of the cross-section is calculated and also plotted in Figure 5.13. It can be seen that the section effective temperature is very close to the measured concrete temperature. Consequently, the measured temperature inside the column will be regarded as the effective temperature of the composite section of the column, and be employed in the following analysis.

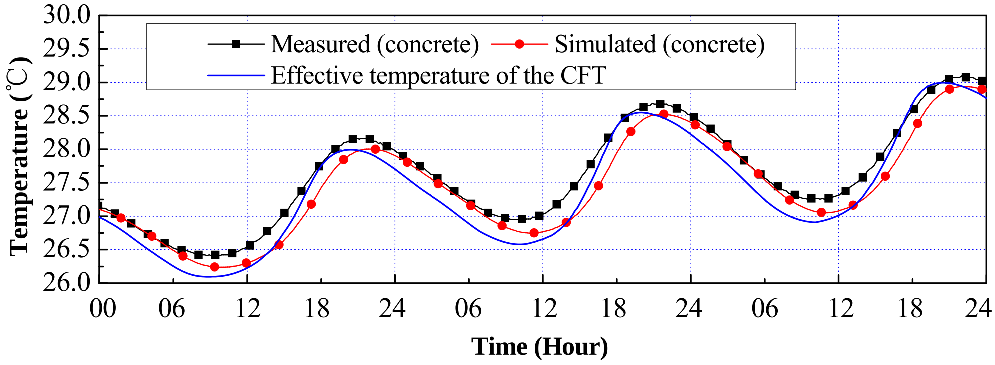

Figure 5.13 The simulated and measured temperature of CFT column at Point C of Section 8 on 2-4 August 2011

5.3.2 Temperature Difference between Inner and Outer Tubes

First we study the temperature difference between the CFT column and the inner core wall in the same structural façade. The effective temperature of the corresponding components as described above is employed. A positive temperature difference denotes the CFT column has higher temperature than the inner wall.

The temperature difference at Sections 8 and 12 in the whole year of 2011 are shown in Figure 5.14 and Figure 5.15, respectively. The two sections represent two typical structural configurations. In Section 8, both inner and outer tubes are exposed to the ambient environment and under similar thermal condition. In contrast, the inner tube of Section 12 is enclosed by the curtain wall whereas the outer tube exposed to the ambient environment. The results show that Section 8 has the maximum positive temperature difference of 2°C in summer and the maximum negative temperature difference of −6°C in winter. In contrast, Section 12 has a maximum positive temperature difference of 8.1°C in summer and negative difference of −15.0°C in winter, both are more significant than Section 8. This is because the curtain wall keeps the inner tube under a stable temperature condition. In particular, it is much cooler in summer and warmer in winter than the outer CFT columns. Consequently its lateral temperature difference is more significant than that without curtain wall.

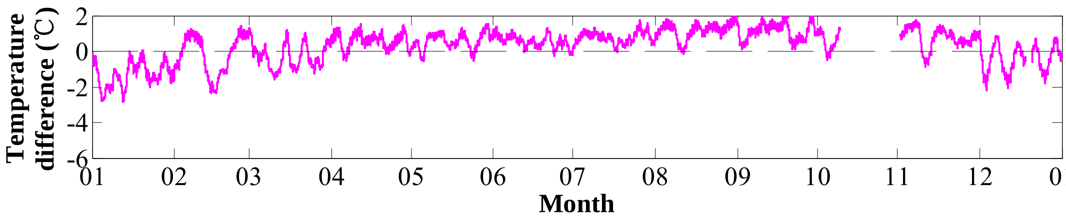

(a) North facade

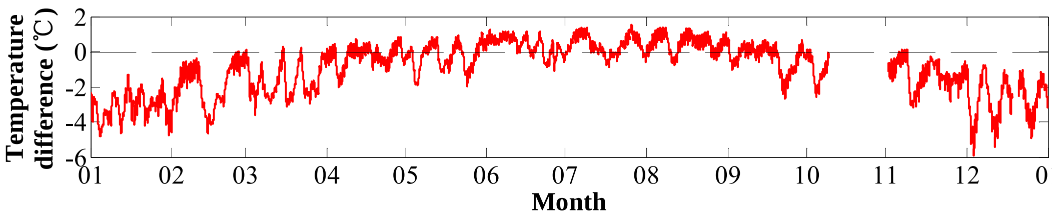

(b) East facade

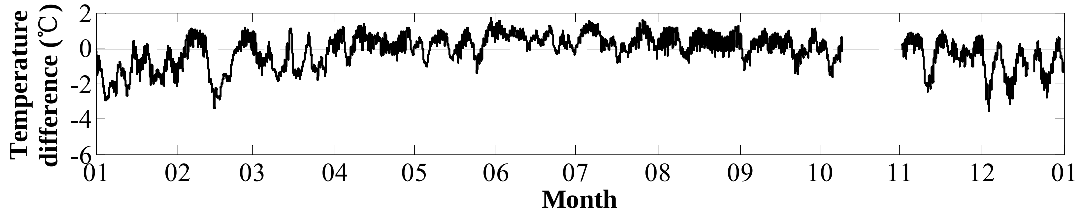

(c) South facade

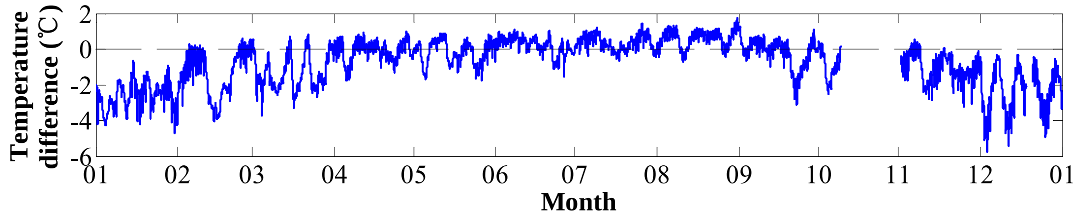

(d) West facade

Figure 5.14 Temperature difference between inner and outer tubes at Section 8 in 2011

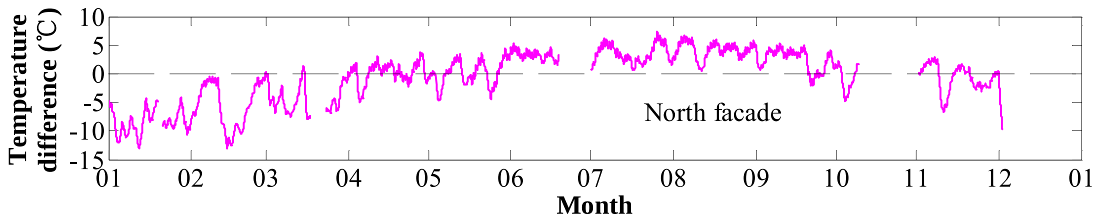

(a) North facade

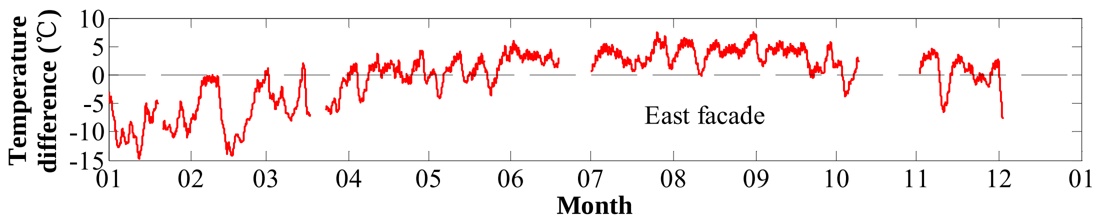

(b) East facade

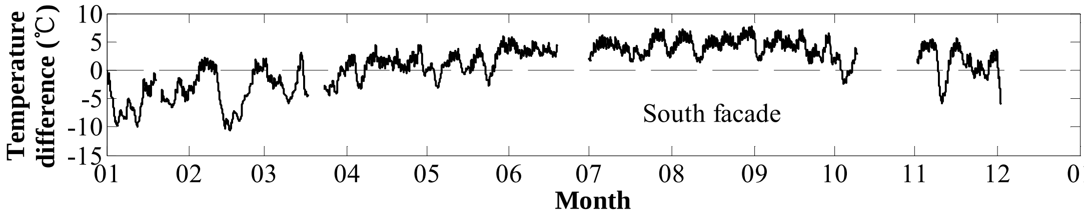

(c) South facade

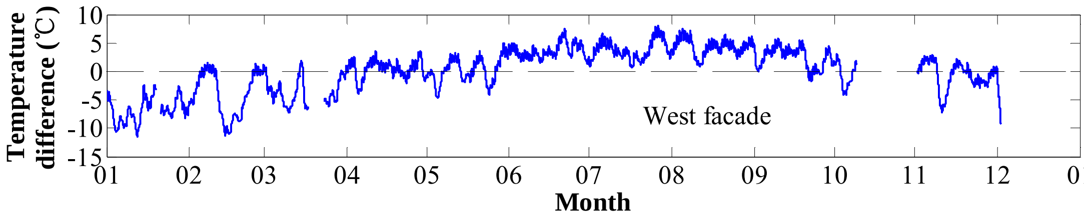

(d) West facade

Figure 5.15 Temperature difference between inner and outer tubes at Section 12 in 2011

The maximum temperature differences of Sections 1 ~ 12 during 2011 are listed in Table 5.2. For Sections 1 ~ 5, temperature of the CFT columns are obtained from the above numerical heat-transfer analysis as no temperature sensor has been installed inside these columns. The maximum positive differences of all sections occur in summer (July and August) and the maximal negative difference in winter (December and January). The orientation of the maximum difference of each section was different, which might occur at all facades except the north. In this regard, the temperature differences at four facades are averaged at each monitoring section to analyze the distribution of temperature difference along the height of the structure.

Table 5.2 Maximal temperature difference between inner and outer tubes in 2011

Section No.	Maximal Positive Value (°C)	Orientation	Time (Month)	Maximal Negative Value (°C)	Orientation	Time (Month)
1	5.0	West	Aug.	−9.0	West	Dec.
2	3.1	West	Aug.	−5.0	West	Dec.
3	1.0	West	Aug.	−2.1	West	Dec.
4	0.9	West	Aug.	−2.6	West	Dec.
5	0.8	South	Aug.	−2.5	East	Dec.
6	1.0	South	Aug.	−2.8	East	Dec.
7	1.9	West	Aug.	−5.3	West	Dec.
8	2.0	West	Aug.	−6.0	East	Dec.
9	4.0	East	Aug.	−7.7	West	Jan.
10	4.5	West	Aug.	−9.7	West	Jan.
11	3.2	South	Aug.	−9.2	South	Dec.
12	8.1	West	Jul.	−15.0	East	Jan.

Among all sections, Section 12 has the largest temperature difference (−15.0°C and 8.1°C), which is significantly larger than that at Section 11 (−9.2°C and 3.2°C), although the inner tube of both Sections 11 and 12 are enclosed by curtain wall. For functional floors at Section 9 ~ 12, which served for various functions including television and radio transmission facilities, observatory decks, computer gaming, shop, as well as revolving restaurants, temperature of the indoor air may be adjusted to be different according to the need of different functions during the operation. As shown in Figure 5.16, temperature of the inner tube (Point 3) at Sections 11 and 12 were similar in 2009 during the construction stage. After that, however, the annual temperature variation at Section 12 is smaller than that of Section 11 during the service stage, exhibiting cooler in summer and warmer in winter than the latter. As a result, the temperature difference between inner and outer tubes at Section 12 is higher than other sections.

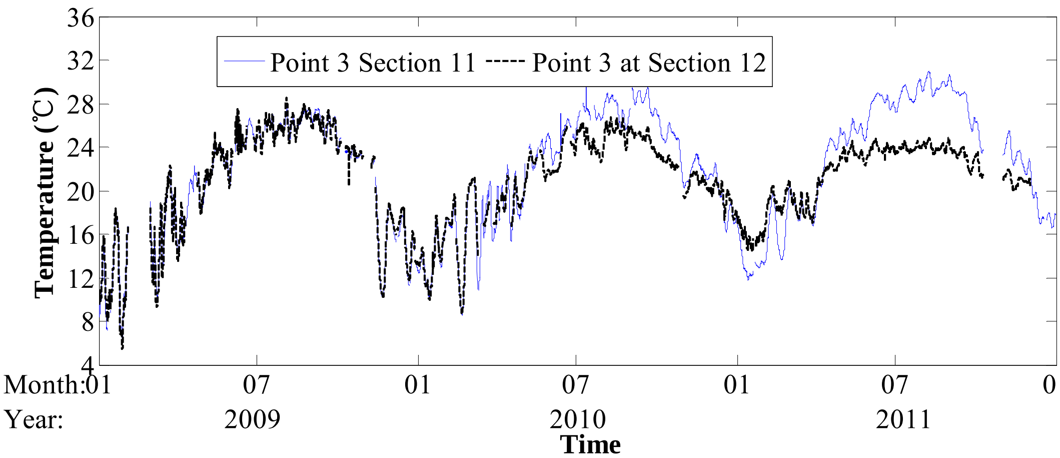

Figure 5.16 Temperature of the inner tube (Point 3) at Sections 11 and 12

Figure 5.17 shows the maximum temperature difference distribution along the structural height, in which data from years of 2010 to 2014 are employed. In winter, the significant negative differences occur in days with a sharp temperature drop. Negative difference distribution along the height of the structure follows a regular pattern that the difference decreases as the elevation of the monitoring section decreases except for Sections 1 and 2, as shown in Figure 5.17. This may be attributed to the fact that air temperature at higher altitude is lower than the lower floor. In addition, the radius of CFT column becomes smaller as the monitoring section higher. The temperature of smaller columns changes faster and larger than the bigger columns when subjected to the varying temperature environment. In summer, the significant positive differences occur in days with high solar radiation intensity. The maximum positive difference occurs at Section 12 as well and the difference decreases as the altitudes decreases. For Sections 3 ~ 8 without functional floors, temperature difference between inner and outer tubes changes slightly along the height of the structure and remains at a relative lower level in both winter and summer. For Section 1 ~ 2 with functional floors, the temperature differences between inner and outer tubes are similar to those at Sections 9 ~ 11.

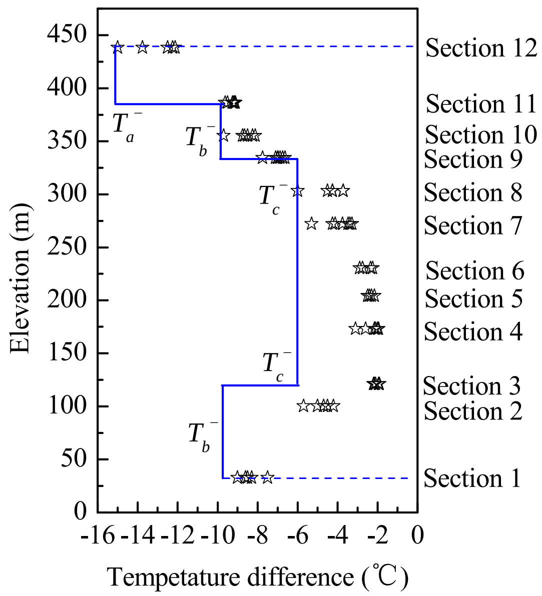

(a) In winter

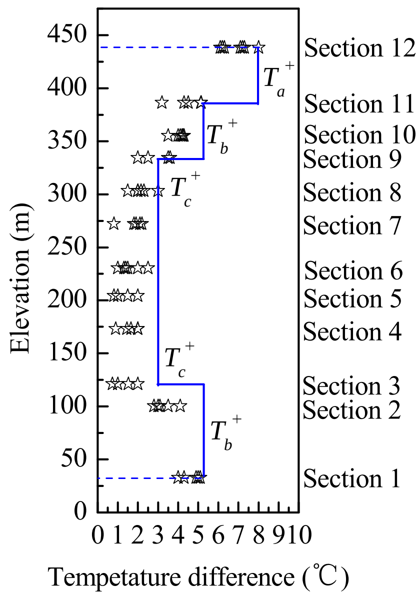

(b) In summer

Figure 5.17 Distribution of the inner and outer temperature difference along the height

On the basis of above observations, the envelope of the temperature difference with respect to the height of the structure can be categorized into three groups, as shown in Figure 5.17: i) the largest temperature difference, $T_a^{+,-}$ for Sections 11 and 12; ii) $T_b^{+,-}$ for Sections 1, 2, 9 and 10 with curtain wall; and iii) $T_c^{+,-}$ for Sections 3 ~ 8 without curtain wall. Superscripts "+" and "–" denote the positive and negative temperature difference, respectively. Here, T_a^+ = 8.0°C, T_b^+ = 5.1°C, and T_c^+ = 3.0°C in summer, while T_a^-, T_b^-, and T_c^- are equal to –15.0°C, –9.7°C, and –6.0°C in winter, respectively.

5.3.3 Temperature Difference between Different Facades of the Structure

In this section we will investigate the temperature difference between different facades. We start with the inner RC core wall, then the outer CFT columns.

5.3.3.1 Inner RC core wall

For the inner RC core wall, define $\Delta T_{ij} = T_i - T_j$, where T_i and T_j (i, j = 1, 2, 3, 4) represent temperature at Points 1 ~ 4. The locations of these measured points are shown in Figure 5.1.

Figure 5.18 illustrates the temperature differences between different facades of Section 12 in 2014. It can be seen that the temperature difference fluctuates slightly in a range of –2.0 ~ 1.5°C in Section 12, indicating that the inner walls with functional floors enclosed by curtain walls have a uniform temperature distribution over different facades. Therefore, their temperature difference is negligible.

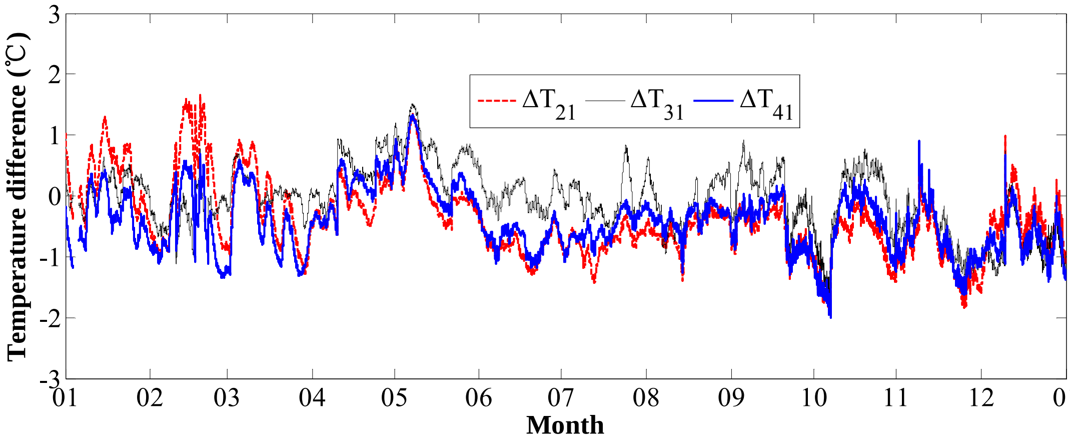

Figure 5.18 Temperature difference between different facades of the inner tube at Section 12 in 2014

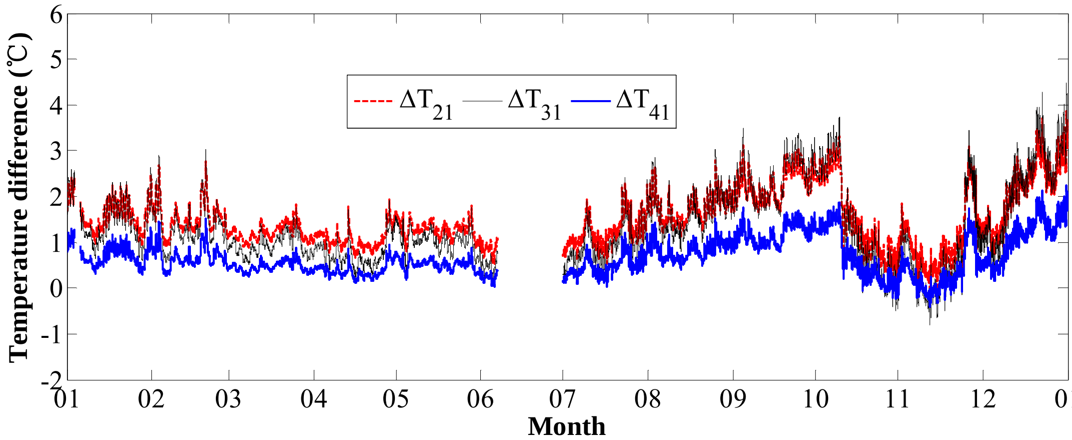

Figure 5.19 Temperature difference between different facades of the inner tube at Section 8 in 2014

The temperature difference between different facades of Section 8 without functional floor is shown in Figure 5.19. The difference is almost positive during the whole year, indicating temperature of the north facade is the lowest, as expected. Winter has the largest difference of about 4.5℃. Some areas of the external surface of the wall are in the shadow of the CFT columns, and thus receive only a portion of solar radiation.

Therefore, the temperature difference between facades at Section 8 remains at a low level and is slightly higher than that of Section 12.

5.3.3.2 Outer CFT columns

For the Outer CFT columns, define $\Delta T_{mn} = T_m - T_n$, where T_m and T_n (m, n = N, E, S, W) represent temperature of the monitoring column on north, east, south and west façades.

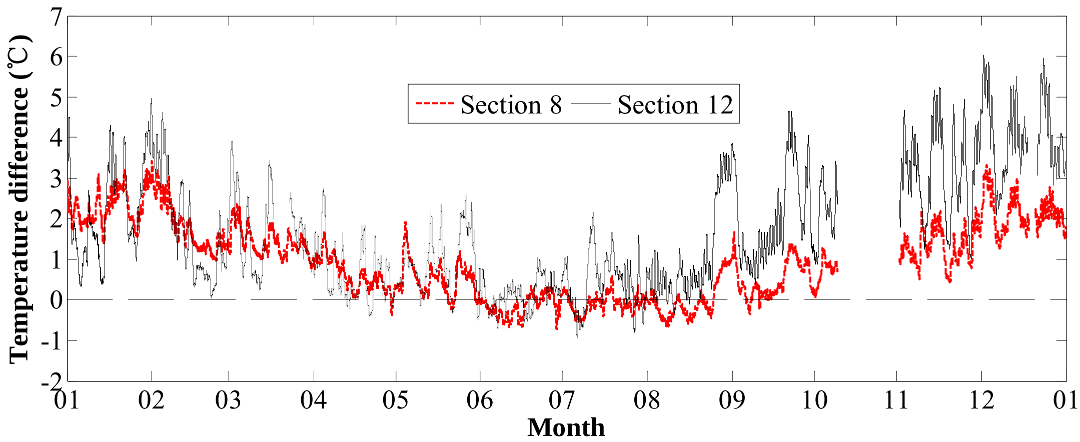

Figure 5.20 Temperature difference of CFT columns between south and north facades (ΔT_{SN}) in 2011

Outer CFT columns receive different solar radiation, causing the temperature difference between different facades. Figure 5.20 shows the temperature difference between the columns on south and north facades at Sections 8 and 12 in 2011. For each CFT column, the effective temperature of the column section is used. A positive temperature difference denotes the south facade has higher temperature than the north. Temperature of the south facade is higher than that of the north facade along the year, as expected. In addition, winter has a larger temperature difference than summer, with a maximum value of 6.0℃.

As the outer columns incline in the vertical direction, the monitoring points at different sections rotate in plan. The temperature difference of all monitoring points in a typical summer and winter days is illustrated in Figure 5.21, where the numeric-alphabet code represents the CFT column, for example, "12A" denotes Point A at Section 12. The lowest temperature of the columns is chosen as the reference and the temperature difference is shown in the figure.

These two typical days are the summer solstice (on 21 June 2012) and the winter solstice (on 22 December 2011), which respectively represents the longest and shortest day of the year in the northern hemisphere. As expected, the south facade has the highest temperature and north the lowest. The temperature difference between different facades of the outer tube is relatively uniform before sunrise, which is below 2.5℃ in both summer and winter. The difference increases after sunrise and reaches 3.6℃ in summer and 6.6℃ in winter. This implies that the difference in winter is more significant than summer. This is attributed to the fact that the Canton Tower is located on the Tropic of Cancer. The sun rises up from the east and appears highest in the sky in the summer solstice and thus the temperature difference between the north and south is small. From summer to winter, the sun moves to the south hemisphere gradually. In winter solstice, the south facade receives much more solar radiation than the north and the temperature difference is thus significant.

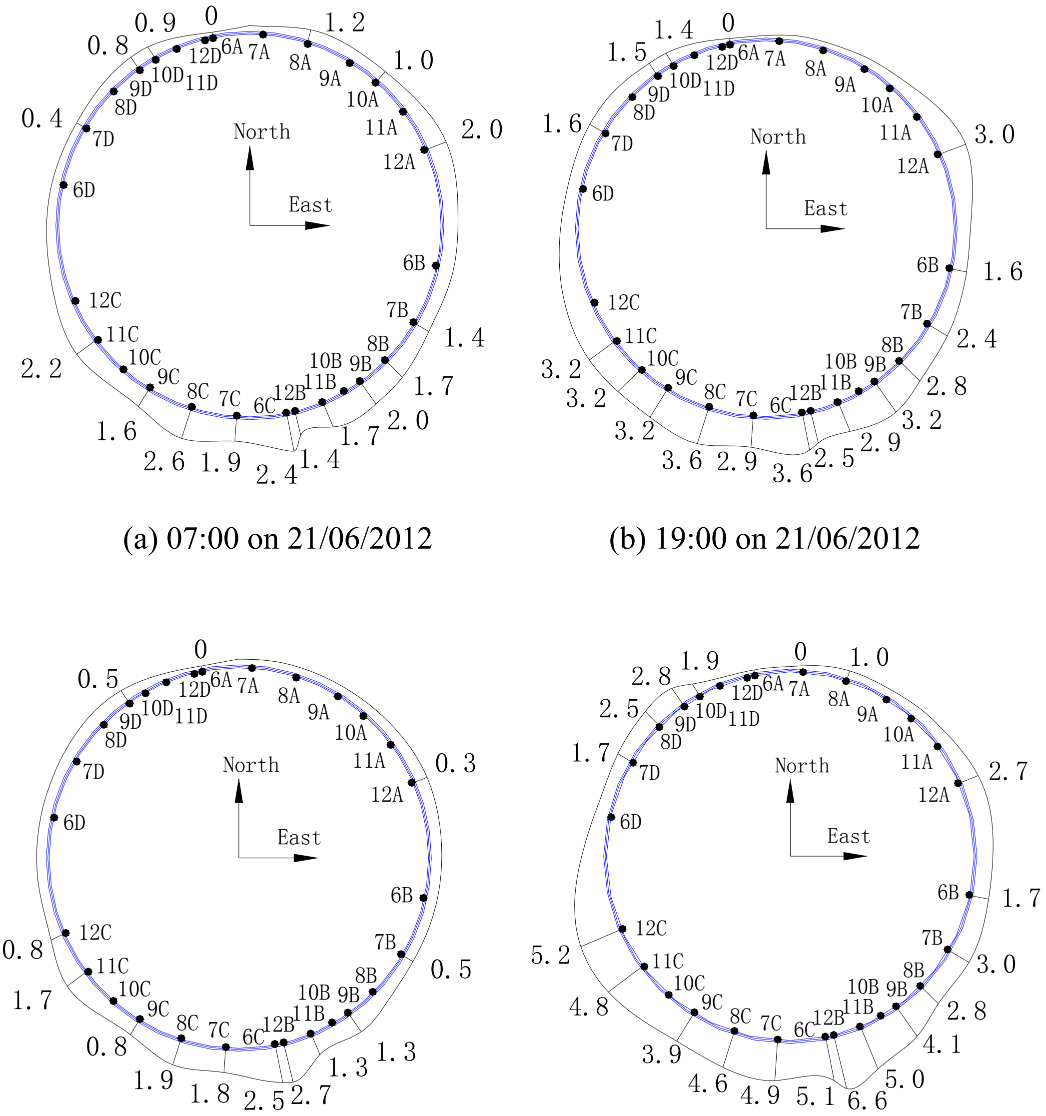

(a) 07:00 on 21/06/2012 (b) 19:00 on 21/06/2012

(c) 08:00 on 22/12/2011 (d) 18:00 on 22/12/2011

Figure 5.21 Temperature difference profile of the outer tube (Unit: ℃)

Figure 5.22 shows the envelope curve of the maximal temperature difference of the outer tube during the period of 2010-2014. It shows that columns in the south have the highest temperature, then west, east, and north the lowest.

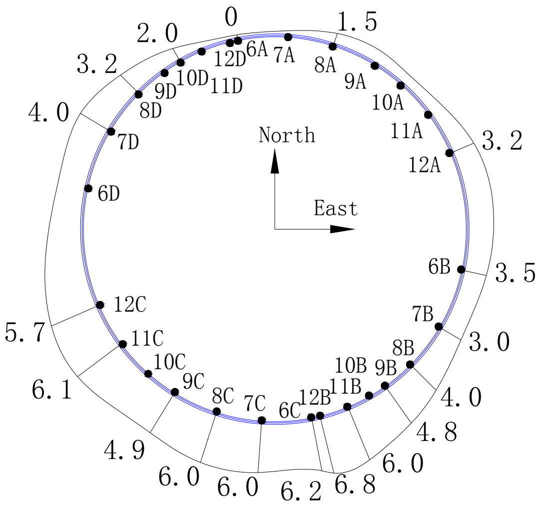

Figure 5.22 The maximal temperature difference of the outer tube (Unit: °C)

5.4 Summary

Accurately obtaining the temperature distribution of supertall buildings is a challenge because of complex configuration and high uncertain and varying meteorological environment. The densely distributed thermal sensors in Canton Tower are used in this study to study the temperature distribution of this supertall structure. Based on the 5-year field monitoring data during the service stage of the structure, following results have been obtained:

1) The structural temperature ranges from 6 to 32°C for the inner tube, and 1 to 36°C for the outer tube.

2) The maximal temperature difference between the outer CFT tube and inner RC tube is −15.0°C in winter and 8.1°C in summer for the inner tube enclosed by curtain wall. For segments where both the outer and inner tubes are exposed to the environment, the maximal difference is −6.0°C in winter and 2.0°C in summer.

3) In all monitoring sections, temperature of the outer tube is higher than the inner tube in summer and lower in winter. Recommendation for distribution of their difference along the structural height is proposed.

4) Temperature difference between different facades of the inner tube enclosed by curtain wall is negligible, while difference of segments where the inner tube is exposed to the environment cannot be ignored.

5) In the outer tube, the south facade has higher temperature than the north, and the maximum difference can be 7°C approximately. The temperature difference profile between different facades is obtained.

The measured temperature data can be used for structural analysis to obtain the temperature-induced deformation and stresses. The temperature distribution model can be used as the reference in design and construction of similar supertall structures in future.

The temperature pattern obtained in this study may not necessarily represent other structures. The temperature characteristics depend on the structural configuration, construction materials, meteorological condition, and geographical locations. For example, temperature of a steel structure directly exposed to the ambient may reach 40 ~ 50°C in summer in South China. With more in-service monitoring exercises implemented in high-rise structures, the temperature models can be more reliably formulated and codified.

CHAPTER SIX

THERMAL LOADING EFFECTS ON CANTON TOWER

6.1 Introduction

Chapter Five has shown that the Canton Tower has a significant temperature difference between the inner and outer tubes, and difference between facades of the structure due to the varying temperature conditions. Statical indeterminacy of the structure and non-uniform distribution of temperature will lead to deflection and thermal stress of the structure (Yi *et al.* 2013; Chen *et al.* 2014).

For high-rise structures, most of relevant studies involve short-term field measurement of temperature and movement only. There have been few studies of thermal effects on high-rise structures based on long-term SHM system. This chapter will integrate the field monitoring and numerical simulation to study the temperature action of the Canton Tower, including temperature-induced displacement and stresses. The results will be compared with the typhoon-induced counterparts.

6.2 Temperature-induced Responses from Field Monitoring

6.2.1 Temperature-induced displacement

The GPS-measured horizontal displacement track at the top of the tower (465 m) in one year (from April 2013 to March 2014) is illustrated in Figure 6.1. The maximum motion for the whole year was about 31 cm in the east-west direction and 31 cm in the south-north. The displacement is mainly induced by the temperature change and the heavy wind or typhoon. During the period, the air temperature varied approximately from 3°C to 37°C, while the maximum 10-min mean wind speed was about 25 m/s in Typhoon Usagi occurred during 22-23 September 2013.

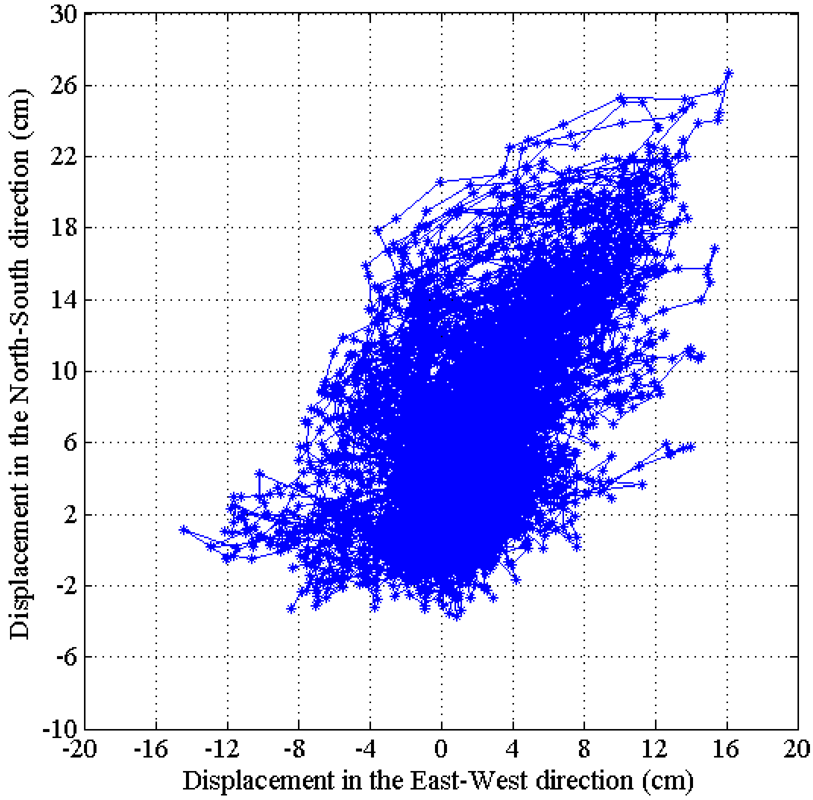

Figure 6.1 Horizontal displacement of the tower top in one year

Figure 6.2 shows the measured horizontal displacement at the top of the tower on 1 December 2013, which was a sunny day and the wind speed was low. The displacement was mainly induced by the thermal load because there was no other significant loading on the structure. The ground air temperature variation on 1 December 2013 was 9°C ~ 23°C, as illustrated in Figure 6.3.

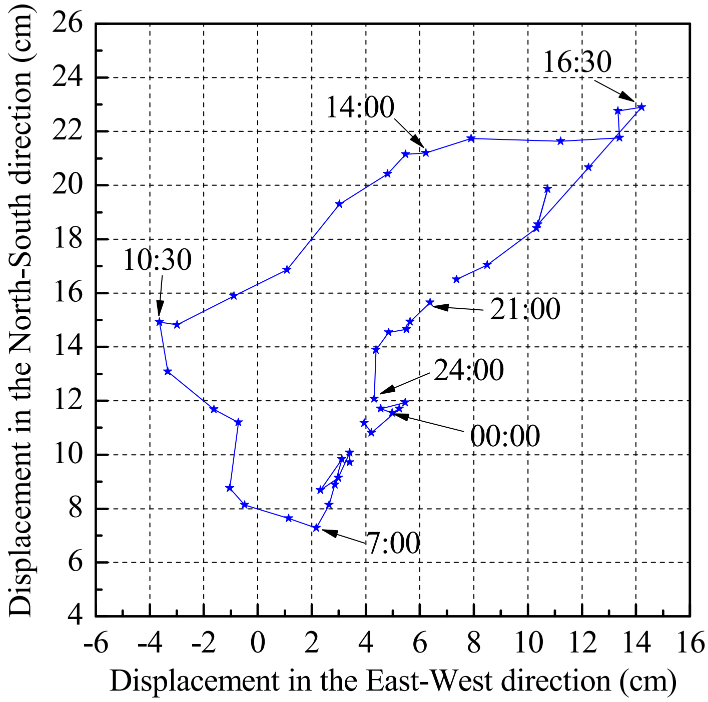

Figure 6.2 Measured horizontal displacement of the tower top on 1 December 2013

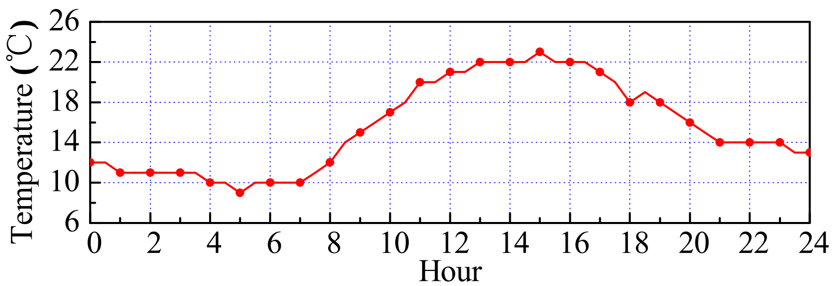

Figure 6.3 Air temperature on 1 December 2013

The positions of the daily movement track shown in Figure 6.2 were the averaged data every half-hour period. The tower moved relatively slow before sunrise (before 7:00), and moved to northwest after sunrise and arrived at its westernmost position at approximately 10:30. This is attributed to the fact that the sun rose from the southeast direction in the winter, causing the members in the southeast had higher temperature than those on the shaded façade, and consequently the structure bent away from the sun. For the same reason, the temperature of the members in the southwest increased when the sun moved to the west in the afternoon, causing the tower moved toward northeast and reaching its northernmost position at about 16:30. After sunset, the temperature difference between the tower members decreased. Therefore, the tower moved back gradually from the north to the south and return back to the initial point (at 24:00) finally. The peak-to-peak motion throughout the day was 17.5 cm in the east-west direction and 15.6 cm in the south-north, and the maximum displacement was about 21 cm.

The measured horizontal displacement track at the top of the tower on other sunny days in different seasons is illustrated in Figure 6.4. The dates are 14 April 2013, 11 August 2013, 12 October 2013, and 1 January 2014. They all had a significant daily air temperature variation of more than 10°C (see Figure 6.5). The wind speed of the days was no more than 3.5 m/s.

The daily movement of the tower top on these four days exhibited a similar pattern as that shown in Figure 6.2, in the clockwise direction. Moreover, the tower moved towards north-east by about 15 cm (between the centroids of tracks) from summer to winter. This is because the south façade receives more solar radiation than the north in winter and their temperature difference is significant, as explained in Chapter Five.

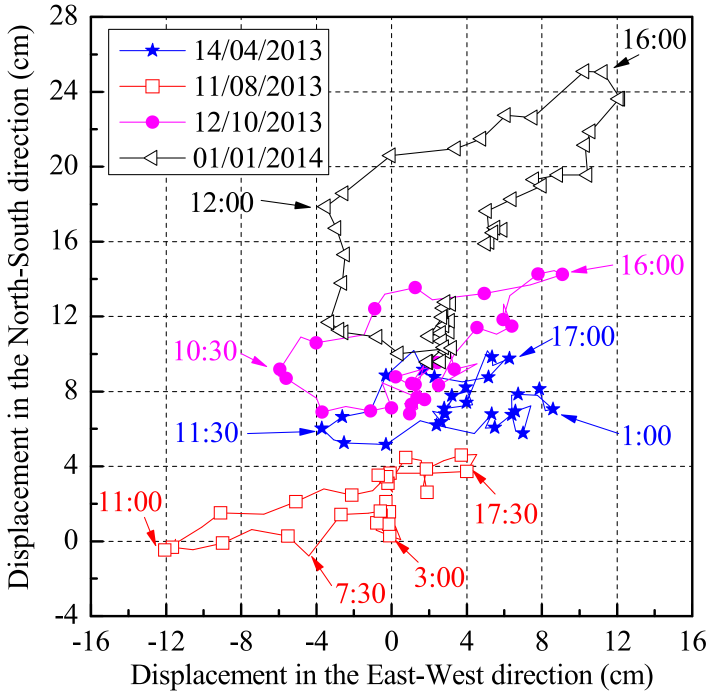

Figure 6.4 Measured horizontal displacement track at the tower top on four sunny days in different seasons

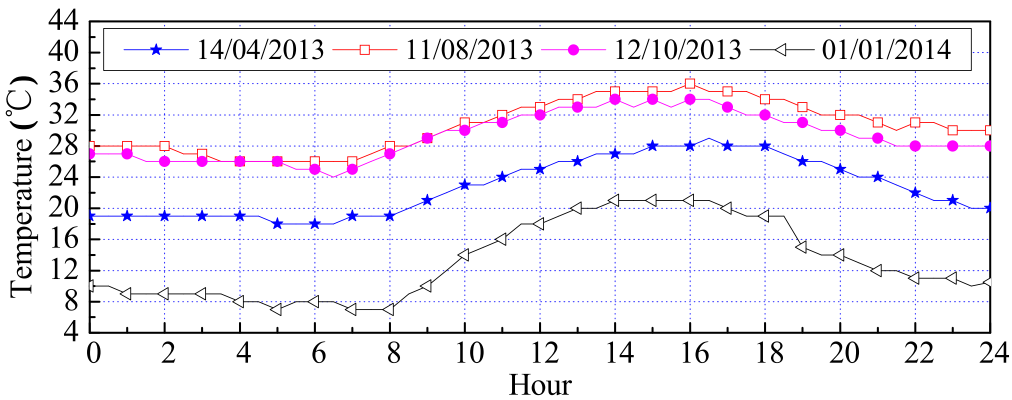

Figure 6.5 Air temperature on four sunny days in different seasons

The daily horizontal displacement in the east-west direction on sunny days in different seasons was more or less similar (12 ~ 16 cm). However, that in the south-north direction in winter (15 cm) was significant larger than that in summer (5 cm), as shown in Figures 6.4 and 6.6. Again this is because winter has a significant temperature difference between the south and north facades.

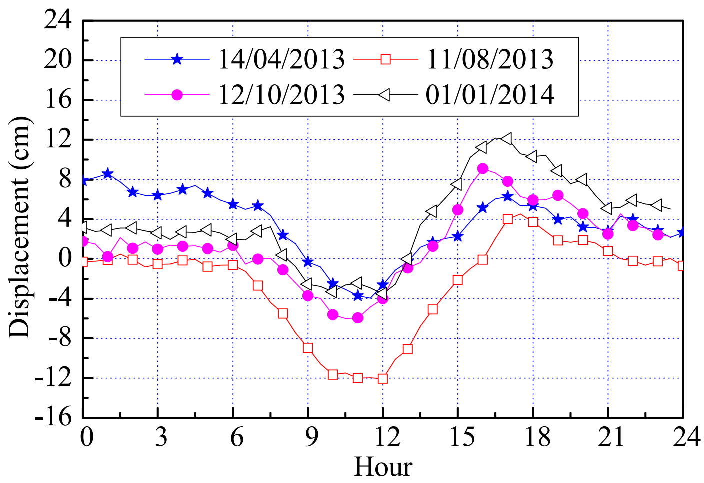

(a) East-west direction

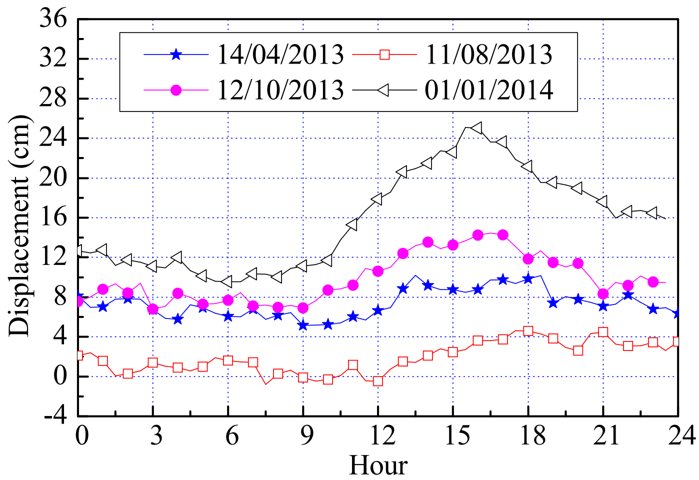

(b) South-North direction

Figure 6.6 Measured horizontal displacement at the tower top on four sunny days in different seasons

6.2.2 Temperature-induced stress

6.2.2.1 Seasonal stress change

For an axial loaded member made by one single material, stress σ is calculated from the following equation:

$$\sigma = E\left(\varepsilon - \alpha_T \Delta T\right) \tag{6.1}$$

where ε is the measured total strain, E is Young's modulus of material, and α_T is the thermal coefficient of linear expansion of the material. For the RC core wall of the inner tube, the stress is calculated based on the material properties of concrete. Although the stress of the wall is basically in three dimensions, only the vertical stress is studied here.

Figure 6.7 shows the variation of the vertical stress and temperature at Section 8 of the inner tube in 2011. As the structure had been completed, and there was no other special loading acting on the structure, the variation in the stresses is attributed to normal seasonal temperature change.

It was observed that the vertical stress measured at Point 1 increased (compression decreased) by around 0.5 MPa as temperature increased from winter to summer, as shown in Figure 6.7(a). A similar tendency can be observed at Points 2 ~ 4, with a compression dropped by about 1.0 MPa, 1.3 MPa, and 1.0 MPa, respectively, as plotted in Figure 6.7(b ~ d). This indicates that the inner tube was in tension as structure temperature increased from winter to summer. Subsequently, the vertical stresses at Point 1 ~ 4 decreased (or compressive rose up) by about 1.0 MPa, 1.2 MPa, 1.7 MPa, and 1.3 MPa, respectively, from summer to next winter. The variation in stress as a percentage of the total stress at Points 1 ~ 4 was about 10%, 12%, 17%, and 13%, respectively. The vertical stress changes at Point 1~ 4 were non-uniform due to the non-uniform temperature distribution and the eccentricity of the entire structure. The stresses at all monitored points were within linear range and far below the design strength of the concrete C50 (the nominal strength is 32.4 MPa), according to GB 50010 (2010), indicating that no damage has occurred at the service stage.

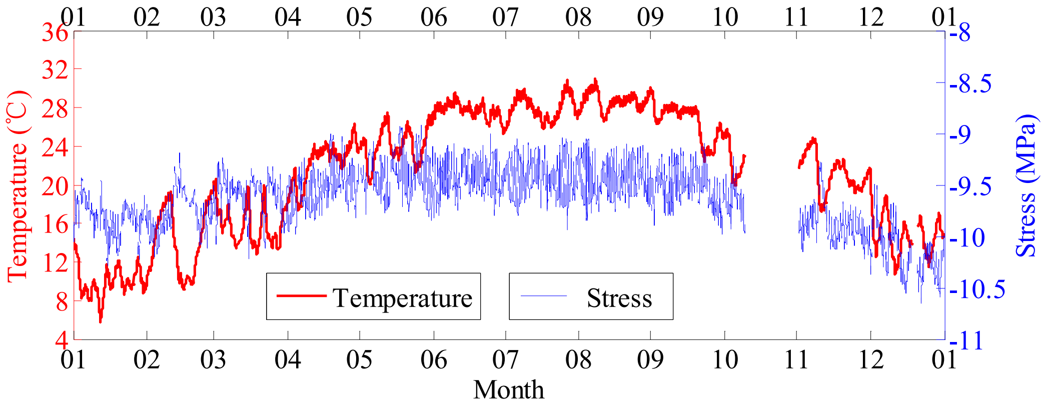

(a) Point 1

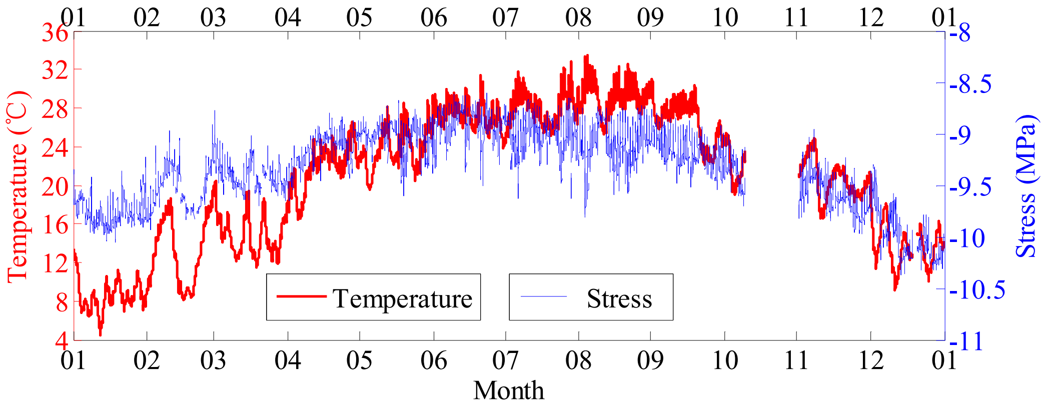

(b) Point 2

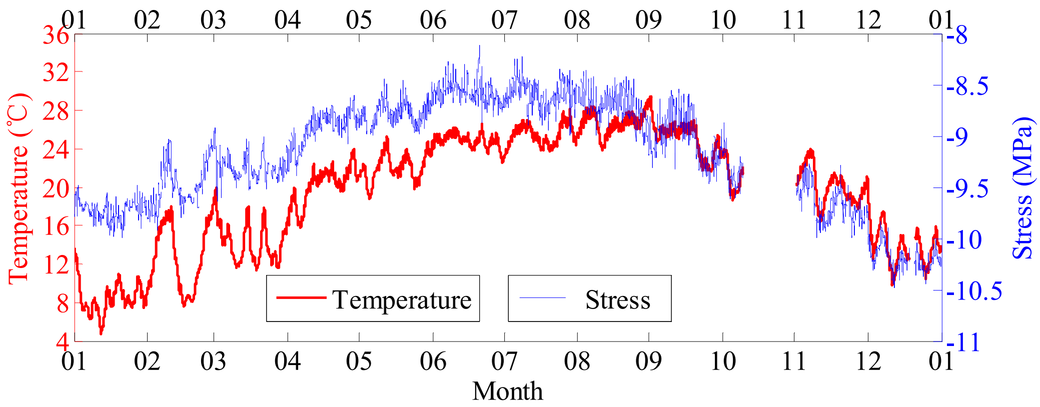

(c) Point 3

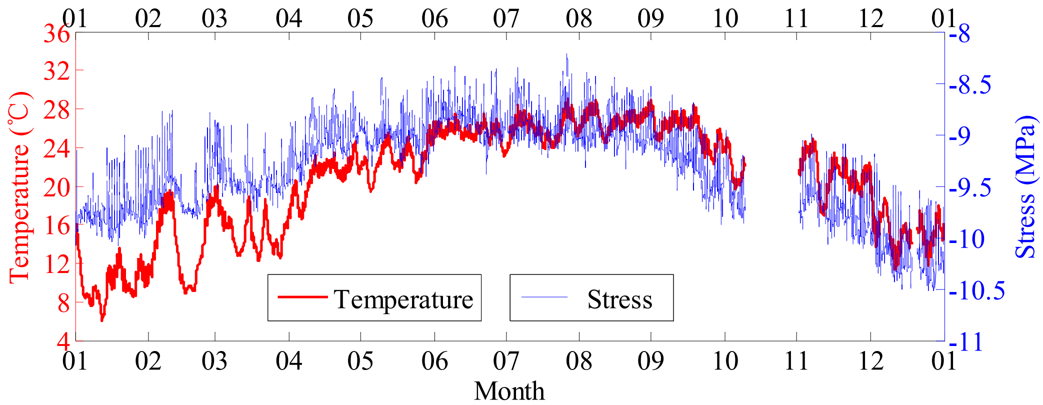

(d) Point 4

Figure 6.7 Temperature and concrete stress of the inner tube on Section 8 in 2011

To illustrate the stress responses along the tower height, the vertical stress changes on different sections of the tower are compared in Figure 6.8. It is noted that the vertical stresses at Point 1 ~ 4 on all sections of the inner tube decreased (compression increased) as temperature decreased from summer to winter. Figure 6.8 also shows that Sections 2 and 9 (in the transition between the zones with and without functional floors) experienced larger variations in stress than other sections, which might be due to the existence of the functional floors. The largest variation in stress was found at Point 2 of Section 2 with about −2.8 MPa, accounting for about

25% of the total stress.

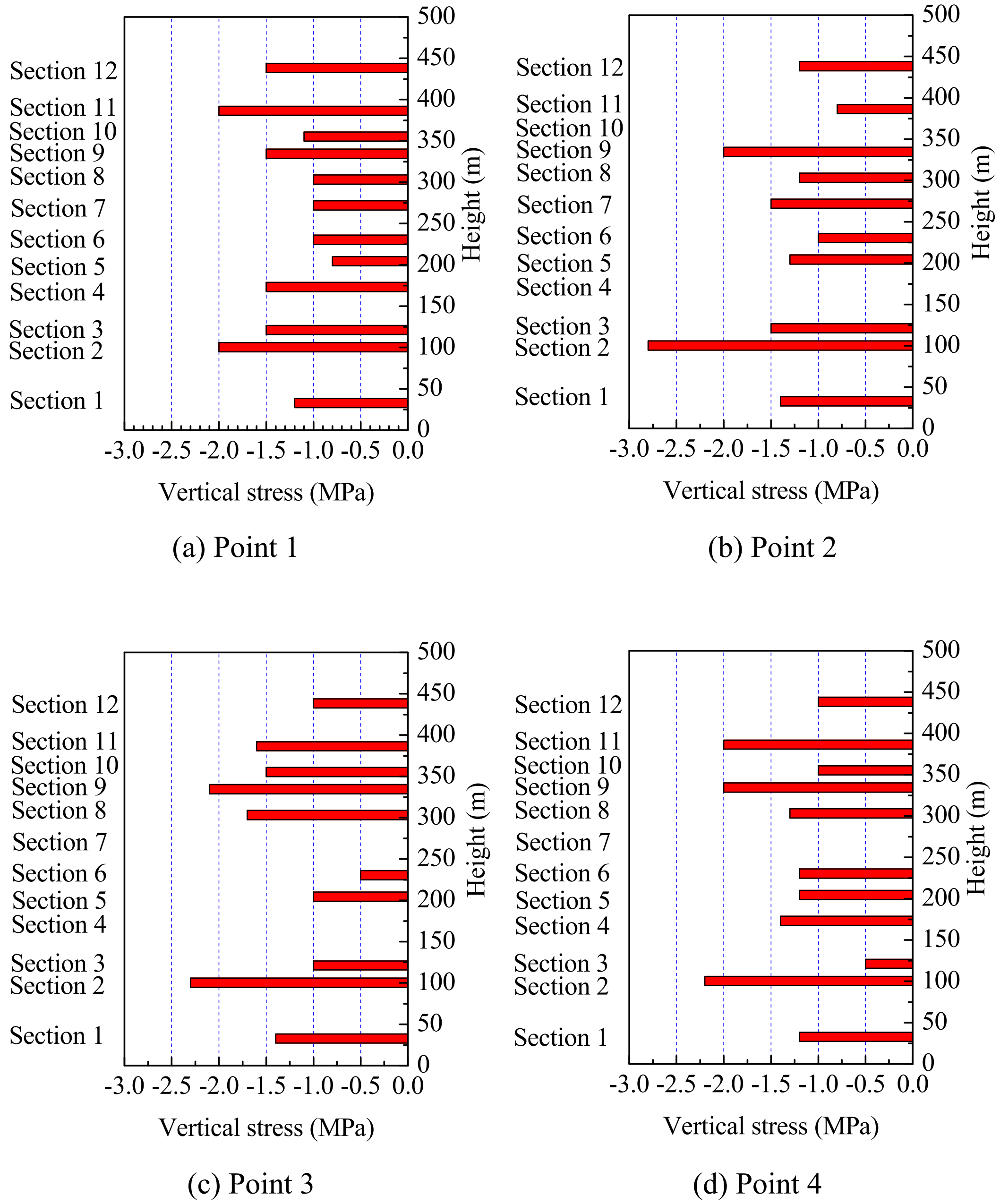

Figure 6.8 Variation in vertical stresses of the inner tube on different sections from summer to winter in 2011

For the outer CFT columns made of steel and concrete, their modulus are quite different and thus the equivalent stress of the columns can be calculated as:

$$\bar{\sigma} = \frac{A_c E_c \left(\varepsilon_c - \alpha_c \Delta T_c\right) + A_s E_s \left(\varepsilon_s - \alpha_s \Delta T_s\right)}{A_c + A_s} \tag{6.2}$$

where subscripts "*c*" and "*s*" denote the properties of concrete and steel, respectively.

The equivalent stress of the outer CFT column at Section 8 is then calculated from the measured stresses of the steel surface and concrete of column, and is shown in Figure 6.9. A similar tendency of the compressive stress as the inner tube can be observed at Point A that stress increased (compression decreased) with temperature increased from winter to summer, and decreased (compression went up) from summer to next winter subsequently. Point A had a variation of –0.7 MPa from summer to next winter. The opposite tendency is found at Point C, which had an increase of 0.9 MPa from summer to next winter. The variations in stress at Points B and D were quite small, no more than –0.2 MPa.

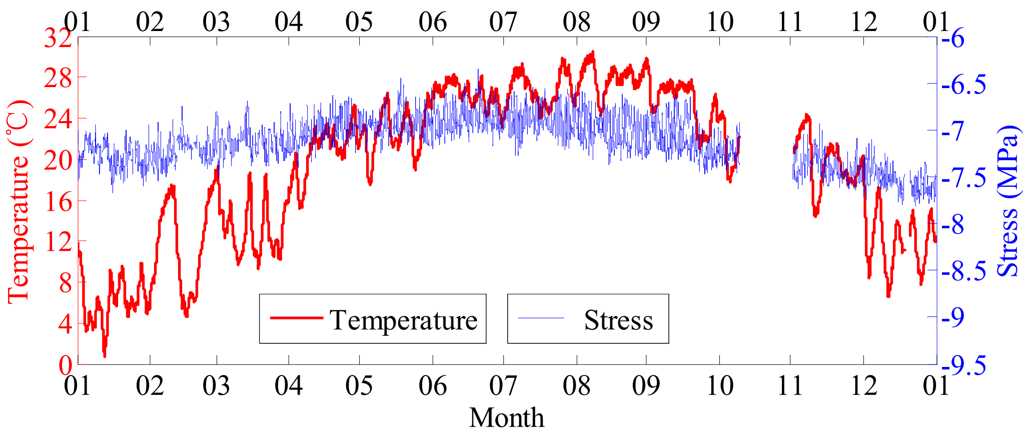

(a) Point A

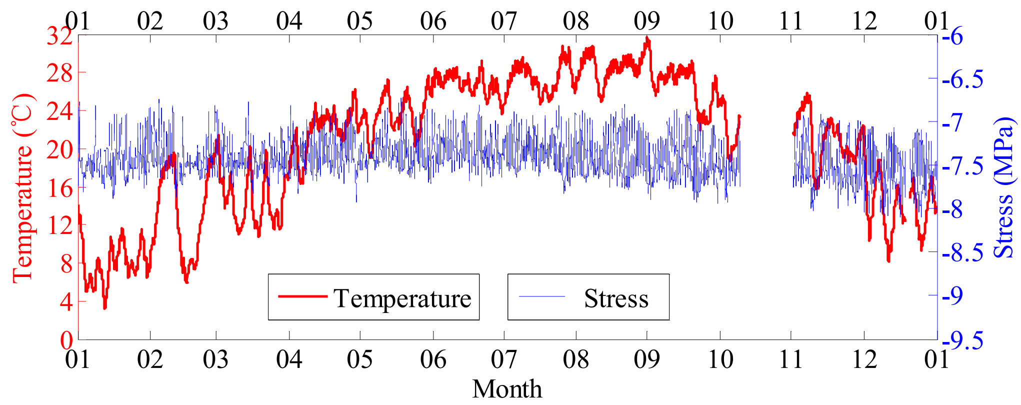

(b) Point B

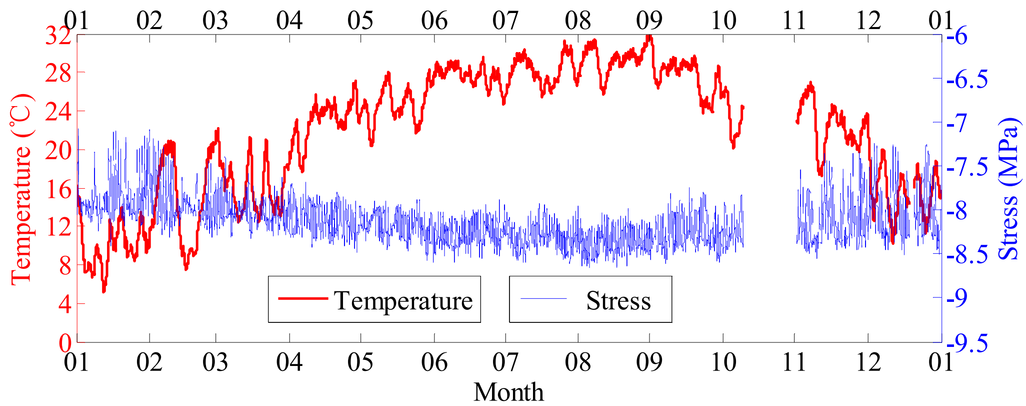

(c) Point C

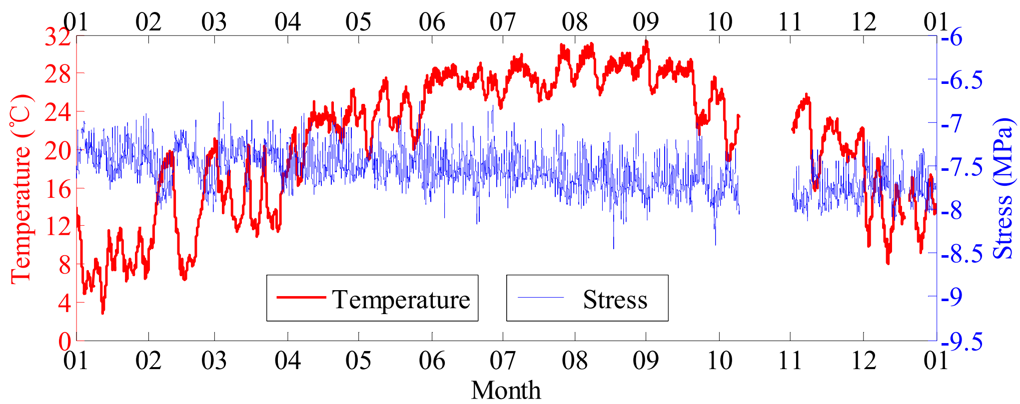

(d) Point D

Figure 6.9 Temperature and equivalent stress of the outer column on Section 8 in 2011

The outer columns on different facades and different heights have different stresses. The stress variation profile of the outer columns from summer to winter in 2011 is plotted in Figure 6.10. It can be seen that the stresses of the CFT columns on the northeast façade decreased, while those on the southwest façade increased. The tower was leaned toward northeast from summer to winter, resulting in the columns on the northeast with a compression increase. Moreover, temperature of the outer CFT columns on the south facade dropped down more than the inner wall from summer to winter, which caused the outer columns have larger contraction deformation in the vertical direction than the inner wall. Such non-uniform contraction between the inner and outer tubes led to tension in the outer columns and compression in the inner core. The largest stress variation of the outer columns was about 0.9 MPa, accounting for about 11% of the total stress.

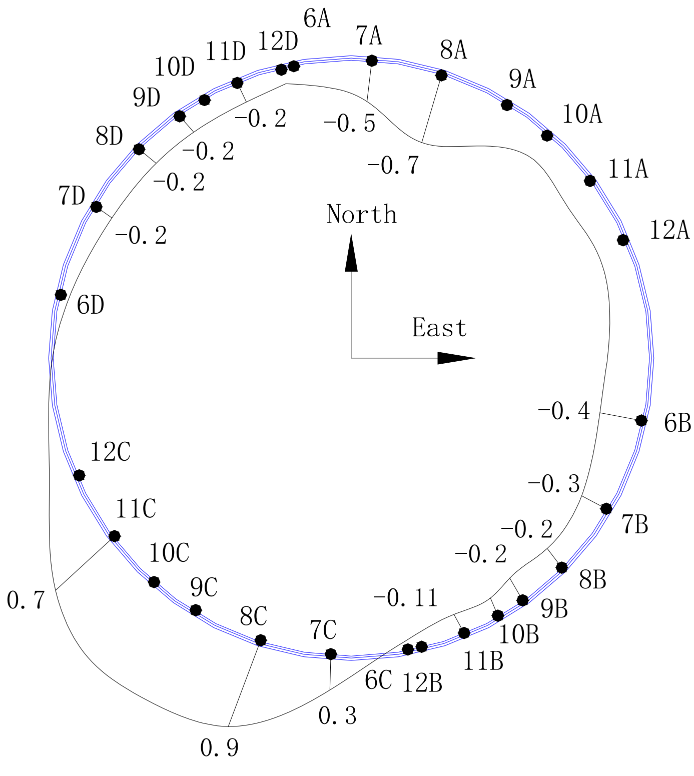

Figure 6.10 Temperature-induced stress variation profile of the outer tube from summer to winter in 2011 (Unit: MPa)

6.2.2.2 Daily stress change

The measured temperature-induced vertical stress of the inner tube on Section 8 in two sunny days (1-2 December 2013) is illustrated in Figure 6.11. The vertical stress remained stable in the early morning, and then increased (compression decreased) with structural temperature increased, which is similar to the seasonal stress changes (see Figure 6.7). In the afternoon, the stress decreased and returned back to the initial value in the evening and midnight. Different facades' stresses reached their maximum at different time instants. Point 2 facing the east had a maximum stress at approximately 10:00, the south wall (Point 3) reached the maximum at around 15:00, and the west (Point 4) did a little later. The stress variation of the north side (Point 1) was the smallest (approximately 0.2 MPa), while that of the west was the largest of about 0.9 MPa.

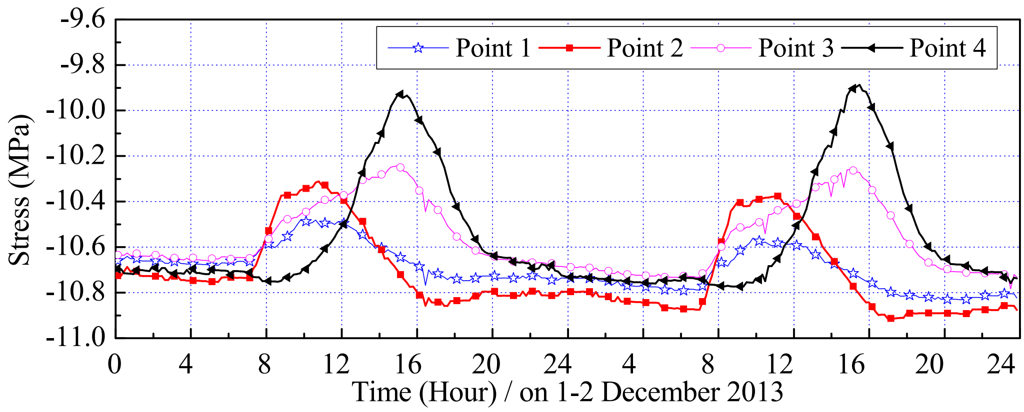

Figure 6.11 Measured temperature-induced vertical stress at Section 8 for the inner tube on 1-2 December 2013

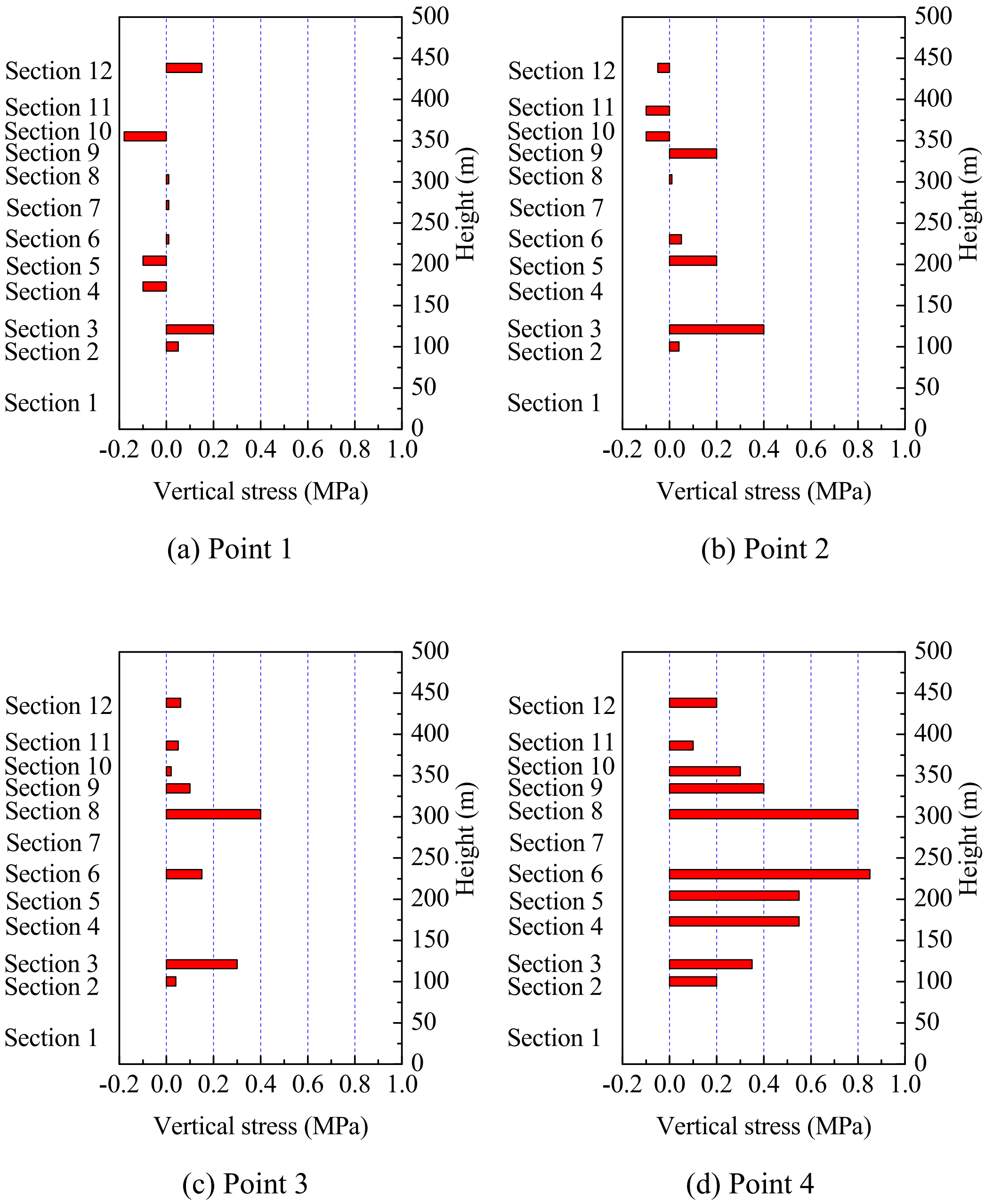

Figure 6.12 Vertical stress variation of different sections of the inner tube between 00:00 and 15:00 on 1 December 2013 (Unit: MPa)

The vertical stress variations at Points 1 ~ 4 on different sections of the tower between 00:00 and 15:00 on 1 December 2013 are shown in Figure 6.12. The vertical stresses at Points 3 and 4 on different sections increased (compression decreased) with daily air temperature increased, while those of some sections at Points 1 and 2 decreased. Point 4 (west facade) on Section 3 ~ 8 (without functional floors) experienced the larger variation in vertical stress when subjected to the daily temperature variation. Point 4 at each section had the largest compression decrease. It is attributed to the fact that the tower leaned toward northeast in the afternoon and the west façade was thus in tension, as shown in Figure 6.2. The largest stress variation at Point 4 was about 0.85 MPa.

Counterparts of the outer CFT columns in the two days are illustrated in Figure 6.13. Different facades' stresses changed inconsistently and reached their maximum at different time instants, resulting from the temperature difference between inner and outer tubes and difference between different facades. Point C on southwest facade had the largest stress increase (about 0.7 MPa), while Point A on the northeast had the smallest variation.

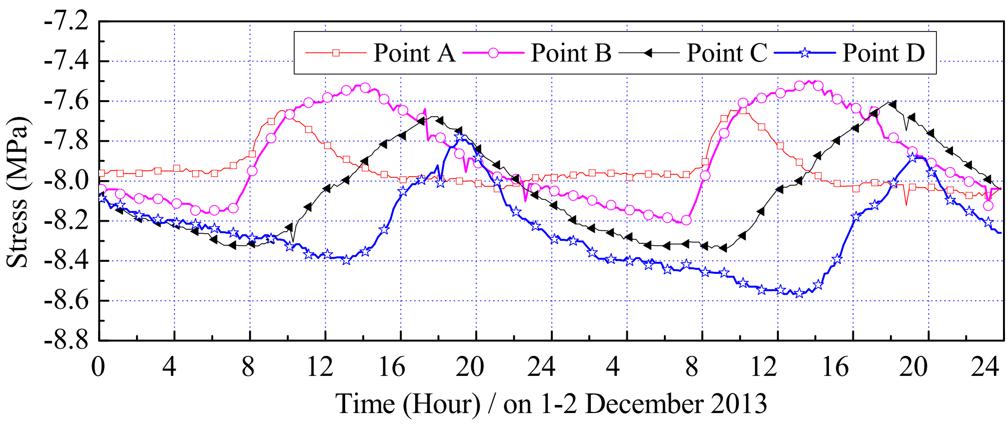

Figure 6.13 Measured temperature-induced stress at Section 8 for the outer CFT columns on 1-2 December 2013

Figure 6.14 plots the temperature-induced stress variation profile of the outer columns between two time instants, 00:00 and 15:00 on 1 December 2013. The air temperature increased by 11°C during the period, as illustrated in Figure 6.3. It can be seen that the CFT column on the south façade had about 0.2 ~ 0.55 MPa stress increase while the northwest and northeast façades had a decrease of 0.1 ~ 0.25 MPa. In addition, the stress variations of the CFT columns on southeast, south, and southwest were basically consistent for different sections.

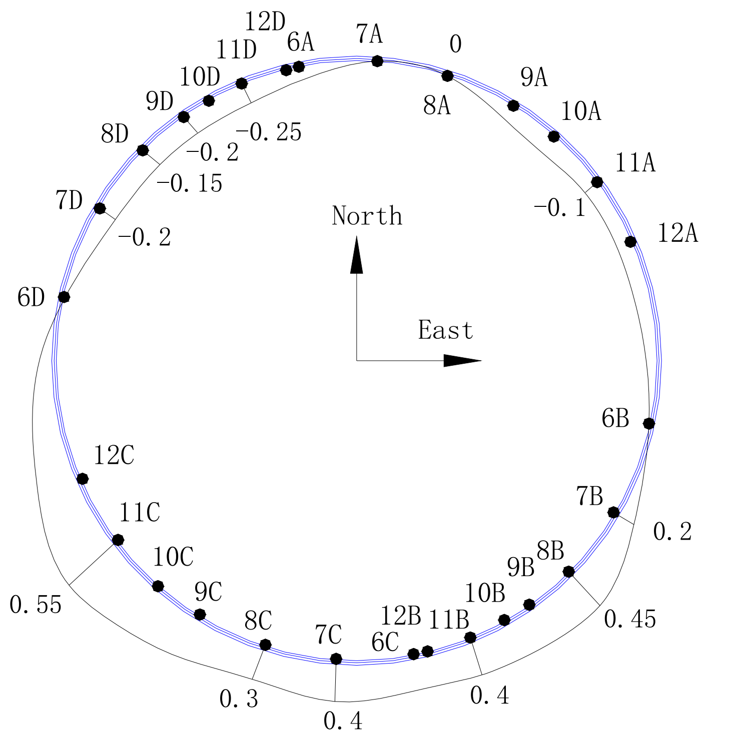

Figure 6.14 Temperature-induced stress variation profile of the outer tube between 00:00 and 15:00 on 1 December 2013 (Unit: MPa)

6.3 Temperature-induced Responses with Numerical Analysis

6.3.1 Finite element model of the Canton Tower

The global FE model of the Canton Tower was constructed using a general FE software package SAP2000 version 14.0 (Computers and Structures Inc. 2009). The full FE model of Canton Tower is shown in Figure 6.15. In this model, four-node and three-node area elements with six DOFs at each node are employed for the shear walls of the inner tube and the floor decks. Two-node three-dimensional beam elements with six DOFs at each node are used to model the outer tube members, the connection girders between the inner and outer tubes, and the antenna mast (see Figure 6.16). All of the nodes in the basement are fixed in all directions. The full model contains 43,067 elements and 28,305 nodes in total.

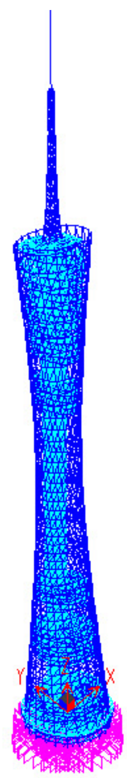

Figure 6.15 The full FE model of Canton Tower

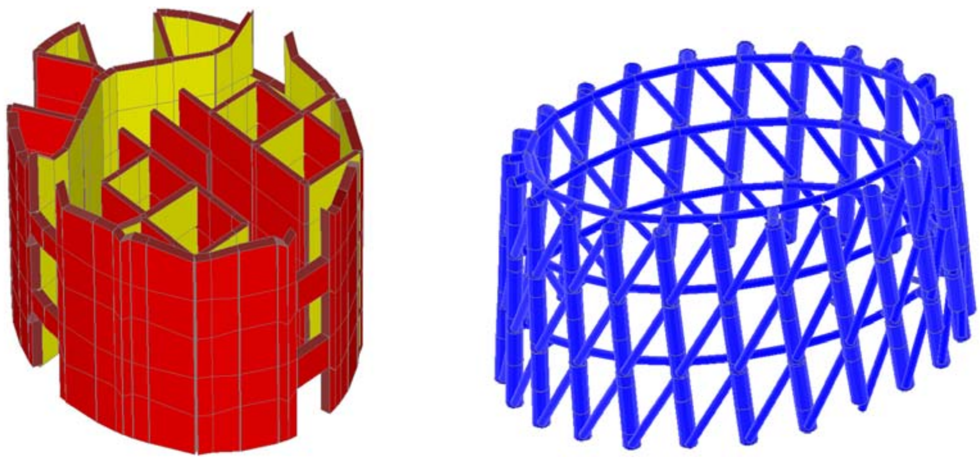

(a) Inner core wall (b) Outer frame tube

Figure 6.16 FE models of the main components

6.3.2 Temperature-induced response simulation

To verify the measured temperature-induced displacement of the tower top, some temperature loading cases with the measured temperature distribution of structural components are applied on the global FE model of the tower. The temperature distribution of the entire structure at 3:00 on 11 August 2013 is selected as the reference state (Case 0), in which the temperature difference between structural components is small. The temperature distribution at 11:00 and at 17:30 on the same day with large temperature difference, are selected as Case 1 and Case 2, respectively. For studying the temperature effects in different seasons, three cases in winter are also analyzed. The time instants of these cases are at 4:00 (Case 3), 12:00 (Case 4), and 16:00 (Case 5) on 1 January 2014.

Chapter Five has analyzed the temperature distribution of some points of the structure based on the long-term monitoring. However, it is very difficult to obtain the detailed temperature distribution of all components of the entire structure. In this regard, the global temperature distribution of the FE model is simplified as follows:

(i). Both the inner and outer tubes are divided into four regions: north facade, east facade, south facade, and west façade. The components on the same façade are assumed to have similar temperature at one time instant.

(ii). Temperature of the floor slab is assumed equal to the mean temperature of the inner tube because floor slabs are enclosed by curtain wall and inner wall.

(iii). The differences between inner and outer tubes are calculated by the simplified curve with respect to the height of the structure (see Figure 5.17). This difference is simplified to be the difference between the mean temperature of inner wall and the mean temperature of four outer columns, as listed in Table 6.1.

(iv). The inner walls in functional floors have a uniform temperature distribution over different facades. Segments where the inner tube are exposed to the environment also have a uniform temperature distribution in summer, whereas the inner walls on south and west façades have higher temperature than the north façade in winter (see Table 6.1).

(v). In the outer tube, the east, south and west facades have higher temperature than the north in winter and summer (see Table 6.1).

According to the above assumptions, temperature of the inner and outer tubes in Case 0 ~ Case 5 are summarized in Table 6.2 ~ Table 6.7, respectively.

Table 6.1 Simplified temperature differences in Case 0 ~ Case 5

Case	Temperature Difference (°C)								
	T_a^+	T_b^+	T_c^+	ΔT_{21}	ΔT_{31}	ΔT_{41}	ΔT_{EN}	ΔT_{SN}	ΔT_{WN}
Case 0	4.4	3.7	0.9	0	0	0	0.4	0.3	1.3
Case 1	4.9	4.1	0.6	0	0	0	3.0	1.4	0.6
Case 2	4.7	4.0	0.2	0	0	0	0.8	1.2	2.0
	T_a^-	T_b^-	T_c^-	ΔT_{21}	ΔT_{31}	ΔT_{41}	ΔT_{EN}	ΔT_{SN}	ΔT_{WN}
Case 3	–9.6	–7.1	0.1	0.6	2.5	1.3	1.7	3.8	1.9
Case 4	–8.9	–7.1	0.1	3.2	3.9	1.9	3.7	5.1	2.4
Case 5	–8.6	–6.1	0.6	1.4	4.1	3.0	2.0	6.7	5.4

Table 6.2 Simplified temperature of the structure at 3:00 on 11 August 2013 (Case 0) (Unit: ℃)

Elevation (m)	Inner Tube North facade	Inner Tube East facade	Inner Tube South facade	Inner Tube West facade	Outer Tube North facade	Outer Tube East facade	Outer Tube South facade	Outer Tube West facade
438.4								
	24.8	24.8	24.8	24.8	28.8	29.2	29.1	30.1
386.4								
	25.5	25.5	25.5	25.5	28.8	29.2	29.1	30.1
355.2								
	25.5	25.5	25.5	25.5	28.8	29.2	29.1	30.1
334.4								
	28.3	28.3	28.3	28.3	28.8	29.2	29.1	30.1
303.2								
	28.3	28.3	28.3	28.3	28.8	29.2	29.1	30.1
272.0								
	28.3	28.3	28.3	28.3	28.8	29.2	29.1	30.1
230.4								
	28.3	28.3	28.3	28.3	28.8	29.2	29.1	30.1
204.4								
	28.3	28.3	28.3	28.3	28.8	29.2	29.1	30.1
173.2								
	28.3	28.3	28.3	28.3	28.8	29.2	29.1	30.1
121.2								
	25.5	25.5	25.5	25.5	28.8	29.2	29.1	30.1
100.4								
	25.5	25.5	25.5	25.5	28.8	29.2	29.1	30.1
32.8								
	25.5	25.5	25.5	25.5	28.8	29.2	29.1	30.1
0.0								

Table 6.3 Simplified temperature of the structure at 11:00 on 11 August 2013 (Case 1) (Unit: ℃)

Elevation (m)	Inner Tube				Outer Tube			
	North facade	East facade	South facade	West facade	North facade	East facade	South facade	West facade
438.4								
	25.0	25.0	25.0	25.0	28.6	31.6	30.0	29.2
386.4								
	25.8	25.8	25.8	25.8	28.6	31.6	30.0	29.2
355.2								
	25.8	25.8	25.8	25.8	28.6	31.6	30.0	29.2
334.4								
	29.3	29.3	29.3	29.3	28.6	31.6	30.0	29.2
303.2								
	29.3	29.3	29.3	29.3	28.6	31.6	30.0	29.2
272.0								
	29.3	29.3	29.3	29.3	28.6	31.6	30.0	29.2
230.4								
	29.3	29.3	29.3	29.3	28.6	31.6	30.0	29.2
204.4								
	29.3	29.3	29.3	29.3	28.6	31.6	30.0	29.2
173.2								
	29.3	29.3	29.3	29.3	28.6	31.6	30.0	29.2
121.2								
	25.8	25.8	25.8	25.8	28.6	31.6	30.0	29.2
100.4								
	25.8	25.8	25.8	25.8	28.6	31.6	30.0	29.2
32.8								
	25.8	25.8	25.8	25.8	28.6	31.6	30.0	29.2
0.0								

Table 6.4 Simplified temperature of the structure at 17:30 on 11 August 2013 (Case 2) (Unit: ℃)

Elevation (m)	Inner Tube North facade	Inner Tube East facade	Inner Tube South facade	Inner Tube West facade	Outer Tube North facade	Outer Tube East facade	Outer Tube South facade	Outer Tube West facade
438.4								
	25.3	25.3	25.3	25.3	29.0	29.8	30.2	31.0
386.4								
	26.0	26.0	26.0	26.0	29.0	29.8	30.2	31.0
355.2								
	26.0	26.0	26.0	26.0	29.0	29.8	30.2	31.0
334.4								
	29.8	29.8	29.8	29.8	29.0	29.8	30.2	31.0
303.2								
	29.8	29.8	29.8	29.8	29.0	29.8	30.2	31.0
272.0								
	29.8	29.8	29.8	29.8	29.0	29.8	30.2	31.0
230.4								
	29.8	29.8	29.8	29.8	29.0	29.8	30.2	31.0
204.4								
	29.8	29.8	29.8	29.8	29.0	29.8	30.2	31.0
173.2								
	29.8	29.8	29.8	29.8	29.0	29.8	30.2	31.0
121.2								
	26.0	26.0	26.0	26.0	29.0	29.8	30.2	31.0
100.4								
	26.0	26.0	26.0	26.0	29.0	29.8	30.2	31.0
32.8								
	26.0	26.0	26.0	26.0	29.0	29.8	30.2	31.0
0.0								

Table 6.5 Simplified temperature of the structure at 4:00 on 1 January 2014 (Case 3) (Unit: ℃)

Elevation (m)	Inner Tube				Outer Tube			
	North facade	East facade	South facade	West facade	North facade	East facade	South facade	West facade
438.4								
	20.0	20.0	20.0	20.0	8.6	10.3	12.4	10.5
386.4								
	18.1	18.1	18.1	18.1	8.6	10.3	12.4	10.5
355.2								
	18.1	18.1	18.1	18.1	8.6	10.3	12.4	10.5
334.4								
	9.5	10.1	12.0	10.8	8.6	10.3	12.4	10.5
303.2								
	9.5	10.1	12.0	10.8	8.6	10.3	12.4	10.5
272.0								
	9.5	10.1	12.0	10.8	8.6	10.3	12.4	10.5
230.4								
	9.5	10.1	12.0	10.8	8.6	10.3	12.4	10.5
204.4								
	9.5	10.1	12.0	10.8	8.6	10.3	12.4	10.5
173.2								
	9.5	10.1	12.0	10.8	8.6	10.3	12.4	10.5
121.2								
	18.1	18.1	18.1	18.1	8.6	10.3	12.4	10.5
100.4								
	18.1	18.1	18.1	18.1	8.6	10.3	12.4	10.5
32.8								
	18.1	18.1	18.1	18.1	8.6	10.3	12.4	10.5
0.0								

Table 6.6 Simplified temperature of the structure at 12:00 on 1 January 2014 (Case 4) (Unit: ℃)

Elevation (m)	Inner Tube North facade	Inner Tube East facade	Inner Tube South facade	Inner Tube West facade	Outer Tube North facade	Outer Tube East facade	Outer Tube South facade	Outer Tube West facade
438.4								
	20.5	20.5	20.5	20.5	8.8	12.5	13.9	11.2
386.4								
	18.7	18.7	18.7	18.7	8.8	12.5	13.9	11.2
355.2								
	18.7	18.7	18.7	18.7	8.8	12.5	13.9	11.2
334.4								
	9.3	12.5	13.2	11.2	8.8	12.5	13.9	11.2
303.2								
	9.3	12.5	13.2	11.2	8.8	12.5	13.9	11.2
272.0								
	9.3	12.5	13.2	11.2	8.8	12.5	13.9	11.2
230.4								
	9.3	12.5	13.2	11.2	8.8	12.5	13.9	11.2
204.4								
	9.3	12.5	13.2	11.2	8.8	12.5	13.9	11.2
173.2								
	9.3	12.5	13.2	11.2	8.8	12.5	13.9	11.2
121.2								
	18.7	18.7	18.7	18.7	8.8	12.5	13.9	11.2
100.4								
	18.7	18.7	18.7	18.7	8.8	12.5	13.9	11.2
32.8								
	18.7	18.7	18.7	18.7	8.8	12.5	13.9	11.2
0.0								

Table 6.7 Simplified temperature of the structure at 16:00 on 1 January 2014 (Case 5) (Unit: ℃)

Elevation (m)	Inner Tube North facade	Inner Tube East facade	Inner Tube South facade	Inner Tube West facade	Outer Tube North facade	Outer Tube East facade	Outer Tube South facade	Outer Tube West facade
438.4								
	21.1	21.1	21.1	21.1	9.0	11.0	15.7	14.4
386.4								
	18.6	18.6	18.6	18.6	9.0	11.0	15.7	14.4
355.2								
	18.6	18.6	18.6	18.6	9.0	11.0	15.7	14.4
334.4								
	9.8	11.2	13.9	12.8	9.0	11.0	15.7	14.4
303.2								
	9.8	11.2	13.9	12.8	9.0	11.0	15.7	14.4
272.0								
	9.8	11.2	13.9	12.8	9.0	11.0	15.7	14.4
230.4								
	9.8	11.2	13.9	12.8	9.0	11.0	15.7	14.4
204.4								
	9.8	11.2	13.9	12.8	9.0	11.0	15.7	14.4
173.2								
	9.8	11.2	13.9	12.8	9.0	11.0	15.7	14.4
121.2								
	18.6	18.6	18.6	18.6	9.0	11.0	15.7	14.4
100.4								
	18.6	18.6	18.6	18.6	9.0	11.0	15.7	14.4
32.8								
	18.6	18.6	18.6	18.6	9.0	11.0	15.7	14.4
0.0								

In all cases, the temperature data are inputted into the FE model respectively. The position of the entire structure in Case 0 is regarded as the initial state. The changes of other cases to Case 0 are then calculated and regarded as the thermal-induced responses. For example, the deformed shape of the tower in Case 5 is shown in Figure 6.17, with the scale factor of 200. The simulated displacement in the vertical and horizontal directions of the inner tube (the monitoring point of the GPS rover) in Case 1 ~ Case 5 is listed in Table 6.8, relative to the position in Case 0.

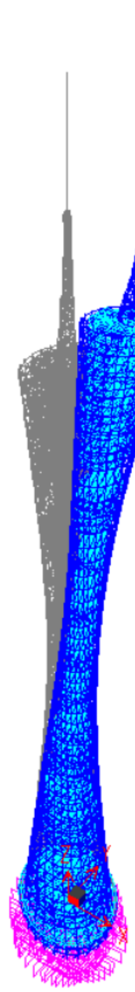

Figure 6.17   Deformed shape of tower in Case 5

The vertical displacement of the GPS monitoring point in the summer day (Cases 1 ~ 2) was very slight, with a value of 0.2 ~ 0.3 cm. From summer (Case 2) to winter (Case 5), the elevation of the tower (465 m) decreased by about 6.0 cm as the average temperature of the inner tube dropped from 26.8°C to 14.5°C. For the inner concrete wall with the thermal coefficient of linear expansion of 10^{-5}/°C, the contraction of the inner wall at the 465 m tall is $\alpha{\cdot}H{\cdot}\Delta T = 10^{-5} \times 465 \times (26.8-14.5) = 0.057$ m, which is in a good agreement with the above displacement (ΔH = 6.0 cm). The daily variation of the vertical displacement of the monitoring point in the winter day (Cases 3 ~ 5) also remained small, while that of the horizontal displacement was significant.

Table 6.8 Simulated displacement of the GPS monitoring point (465 m) in Case 1 to Case 5

Case	Averaged Temperature (°C)	Displacement (cm)		
	Inner tube	Vertical direction	Horizontal direction	
			East-West	North-South
Case 1	15.3	0.2	–6.9	2.0
Case 2	14.5	0.3	1.8	5.3
Case 3	27.8	–5.8	2.3	12.6
Case 4	27.5	–5.5	–2.8	15.6
Case 5	26.8	–5.7	9.9	23.1

Figure 6.18 compares the simulated and measured horizontal position of the tower top (465 m) in all cases. It can be found that the simulated horizontal displacement in the summer day is 8.7 cm in the east-west direction and 5.3 cm in the south-north

direction. The temperature-induced displacement in the winter day is 12.7 cm and 10.5 cm in the east-west and south-north direction, respectively, both larger than the summer. The tower top moved toward the northeast direction from summer to winter. The simulated temperature-induced horizontal displacement under the simplified temperature loads agree with the field measurements very well. Therefore, the simplified temperature model is effective in obtaining the thermal-induced responses of the structure.

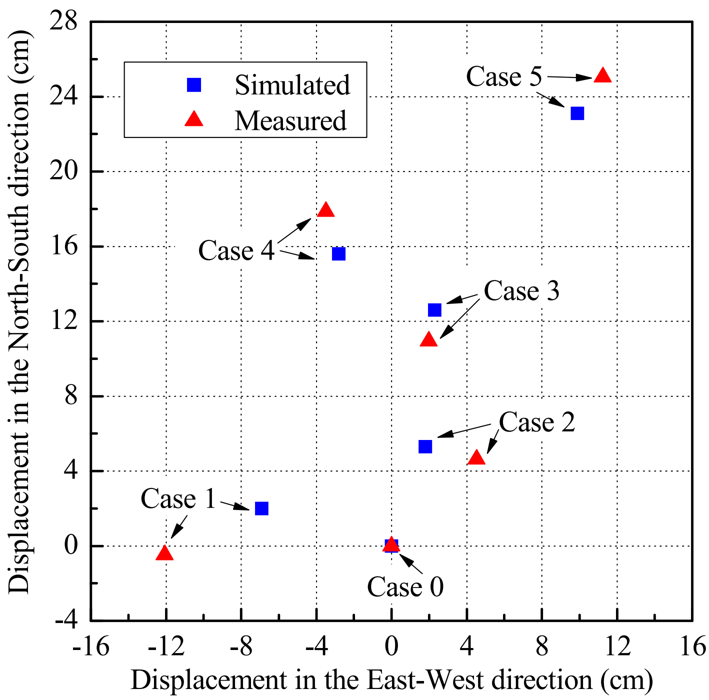

Figure 6.18　Comparison between the simulated and measured horizontal position of the tower top in Case 0 ~ Case 5

Figure 6.19 plots the simulated temperature-induced horizontal and vertical displacement profile of the tower along the height in Case 5 when the Tower had the maximum horizontal displacement relative to the reference state. The horizontal displacement exhibits the bending mode, different from the bending-shear mode of a typical frame-wall structure. This is because the floor girders are pin connected to the outer CFT columns through bolts, which causes the outer columns can rotate freely to release the bending moment of the joints between the inner and outer tubes. Consequently there is less restraint on the deformation between the inner tube and the outer CFT column. In addition, different facades of the same height had a quite consistent horizontal displacement induced by temperature load. In vertical direction, the outer columns had a larger vertical displacement than the inner tube, because the outer tube had a larger temperature decrease from summer to winter. Moreover, different facades had different vertical displacement. In particular, the north and east facades had larger downward displacement than the south and west. This agrees with the observation that the tower leaned toward north-east and thus the horizontal cross-section had an inclination. The maximum vertical displacement difference is about 1.4 cm in the inner tube and 4.4 cm in the outer tube, occurred between the north and south facades.

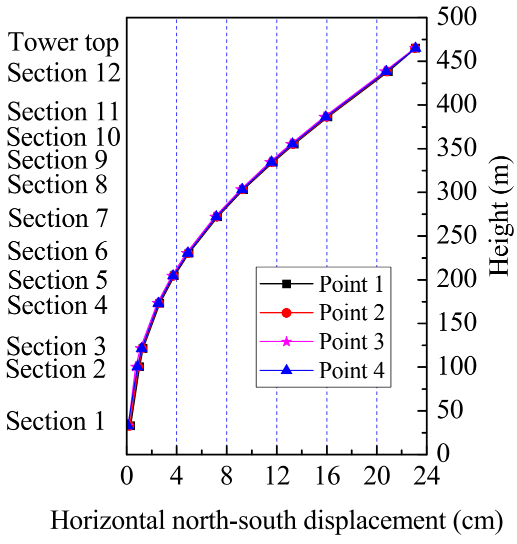

(a) Inner tube

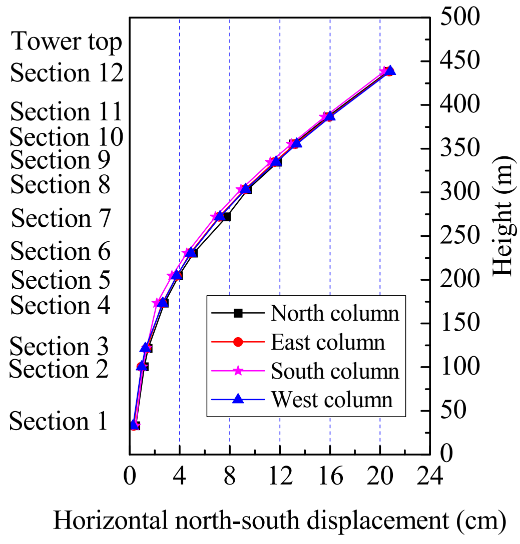

(b) Outer CFT column

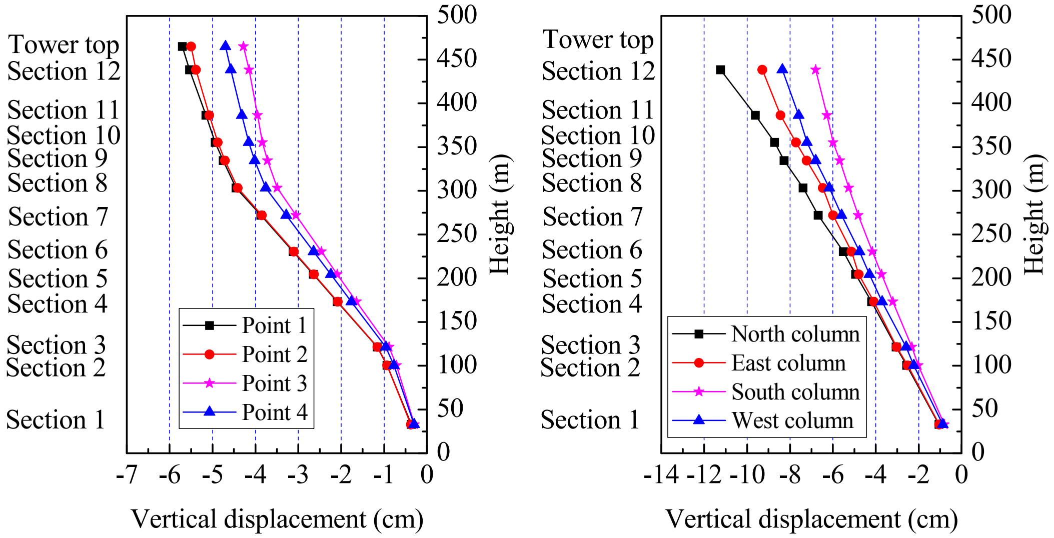

(c) Inner tube　　　　(d) Outer CFT column

Figure 6.19　Simulated temperature-induced displacement profile of the inner and outer tubes in Case 5

Figure 6.20 shows the calculated variations in the stresses of Points 1 ~ 4 at different heights between Case 1 and Case 3 when the structure has the highest temperature in summer and the lowest temperature in winter, as compared with the measured counterparts. The largest variation in stress is found at Point 2 of Section 11 with about −2.2 MPa. The variation of stress changed sharply in the transition between the zone with and without functional floors (Sections 2, 9 and 11), which agrees with the measured result well.

It can be seen that the simulated and measured tendency of the stress change along the height of the tower are generally in agreement although some discrepancy can be found in the segments where the inner tube connects with functional floors. The major reason may be the inaccuracy of the temperature data used in the simplified FE model. For example, the temperature distribution of the floor slabs is assumed as uniform as no sensor has been installed on the floors. In addition, the measurement noise may be the other reason.

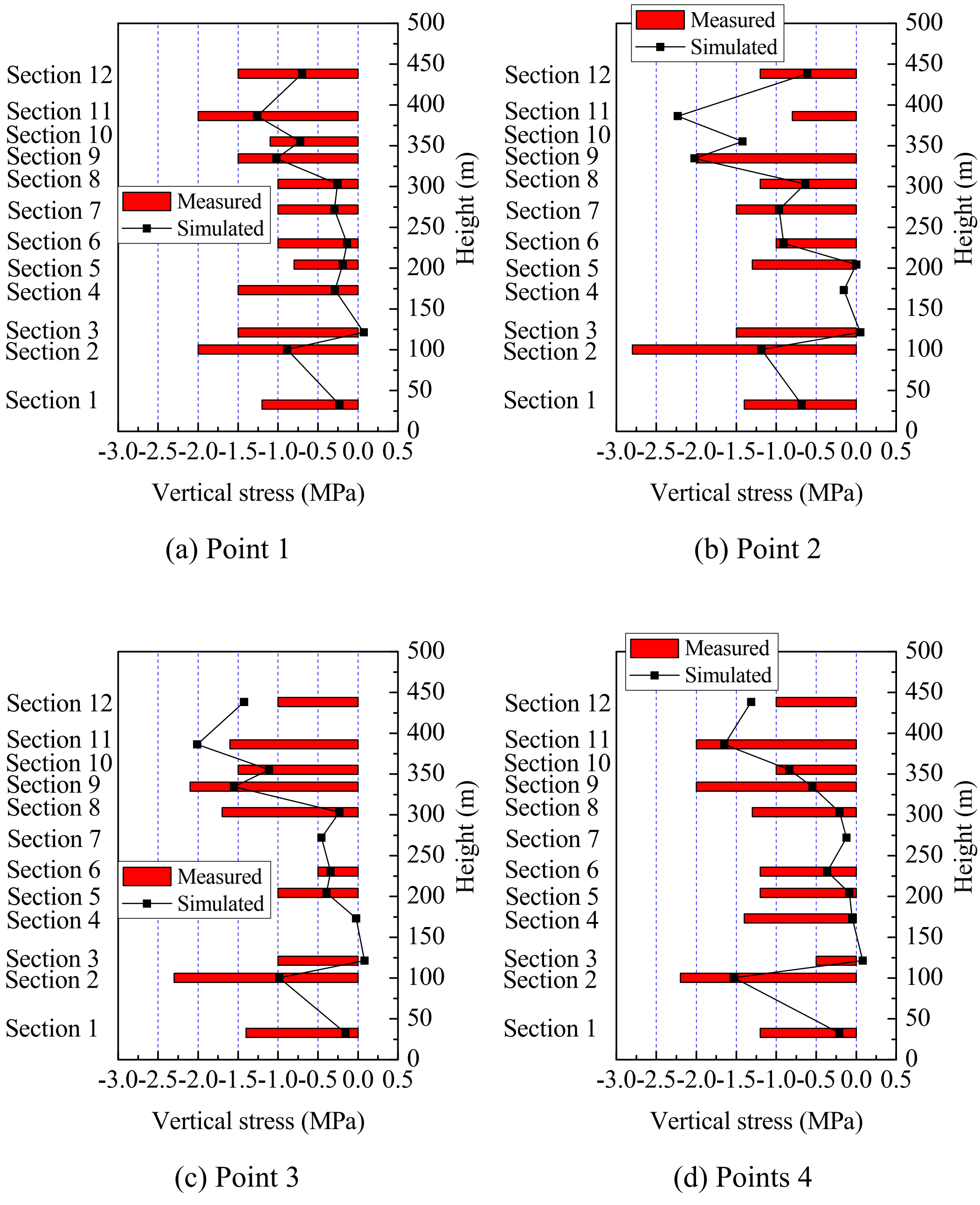

Figure 6.20 Simulated and measured stress variation of the inner tube from summer to winter

Figure 6.21 compares the simulated and measured stress variation profile of the outer tube from Case 1 to Case 3. The columns on the southwest had a significant stress increase by 1.2 MPa. The largest stress decrease occurred at the column on the northeast. The simulated stress variations differ from the measured ones for some columns, particularly northwest. Again this may be because of the modelling error of the temperature distribution and the measurement noise.

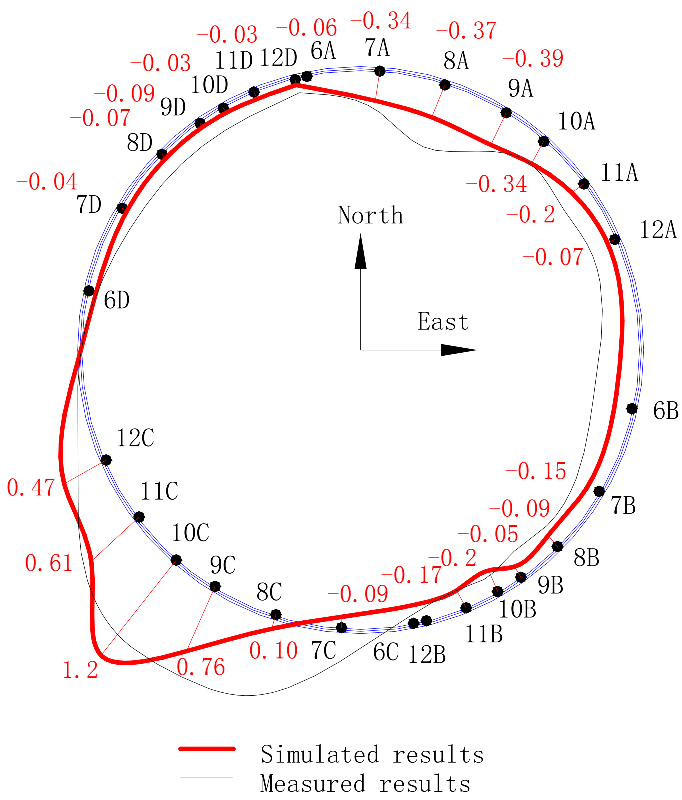

Figure 6.21 Simulated and measured stress variation profile of the outer tube from summer to winter (Unit: MPa)

6.4 Comparison between Temperature-induced and Typhoon -induced Responses

The Canton Tower is located in the coastal region and is frequently subjected to strong typhoons. This section will compare the temperature-induced responses of the structure with those by a strong tropical cyclone, Typhoon Usagi, attacked Guangdong Province from 22 to 23 September 2013. The track of the storm is shown in Figure 6.22.

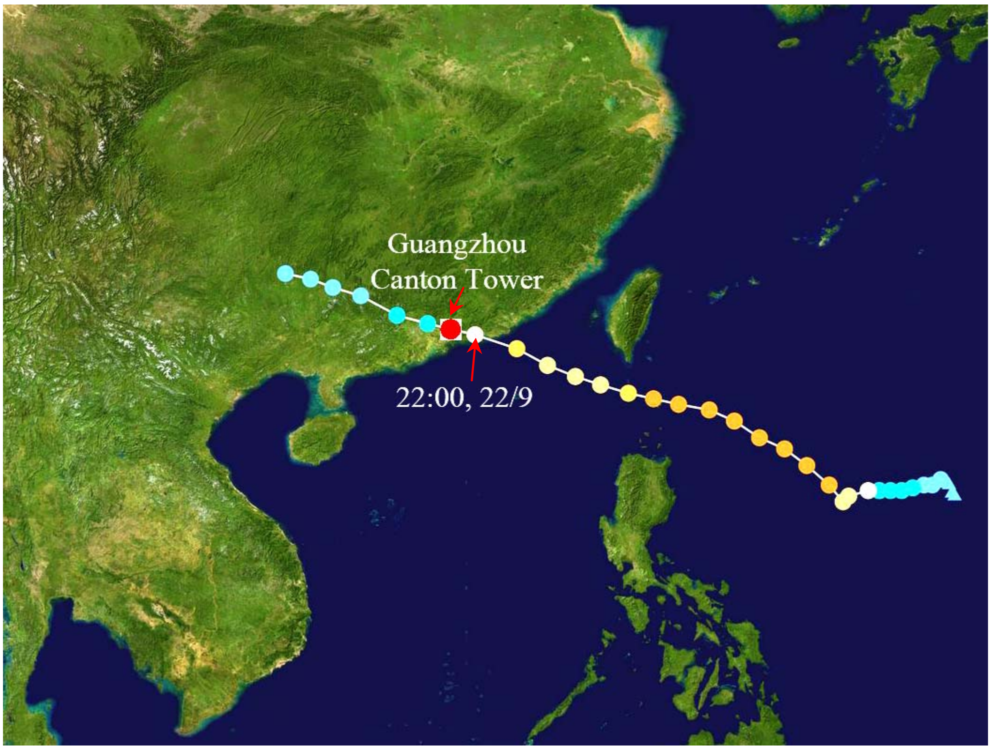

Figure 6.22 The track of Typhoon Usagi

Figure 6.23 shows the ten-minute mean wind speed and the corresponding wind direction, which were measured by the weather station installed on the top of the tower. The wind speed significantly increased from 12 m/s (14:00 on 22 September) to the maximum of 25 m/s (0:00 ~ 4:00 on 23 September), and then decreased to 8 m/s as the typhoon gradually landed in. The wind direction was mainly from the north on 22 September, and turned to the northwest (0:00 ~ 4:00 on 23 September), southwest (4:00 ~ 8:00 on 23 September).

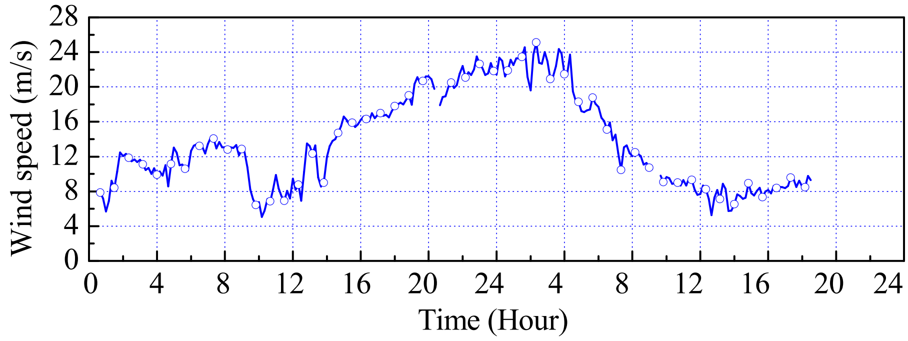

(a) Ten-minute mean wind speed

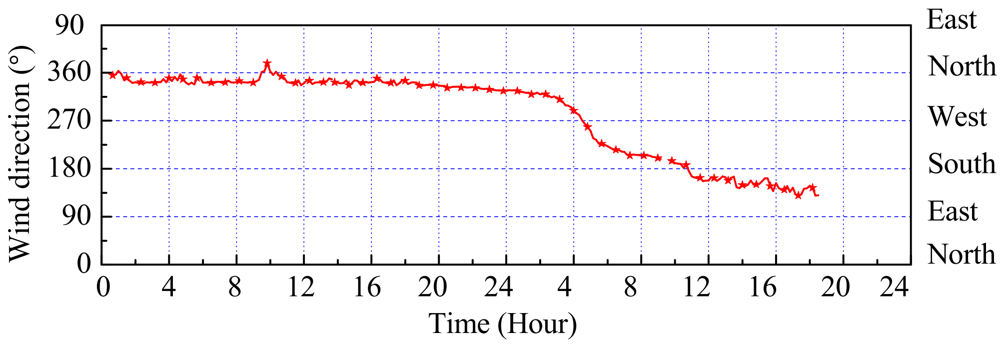

(b) Ten-minute mean wind direction

Figure 6.23 Ten-minute mean wind speed and wind direction at the top of the tower on 22-23 September 2013

Figure 6.24 presents the GPS measured typhoon-induced horizontal displacement of the tower top on 22-23 September 2013. The tower top moved to the south direction by about 7.0 cm between 14:00 on 22 September and 2:00 on 23 September with the increasing north wind. Subsequently, the tower top leaned toward the east direction mainly by about 6.2 cm between 2:00 and 4:00 on 23 September with the maximum west-northwest wind. After that, the tower top returned back toward the west as the wind speed slow down (4:00 and 8:00 on 23 September). The peak-to-peak motion was about 10.1 cm in the east-west direction and 7.0 cm in the north-south during the typhoon period, as shown in Figure 6.25. In comparison with Figure 6.2, it can be found that the temperature-induced horizontal displacement is much larger than that caused by a strong Typhoon.

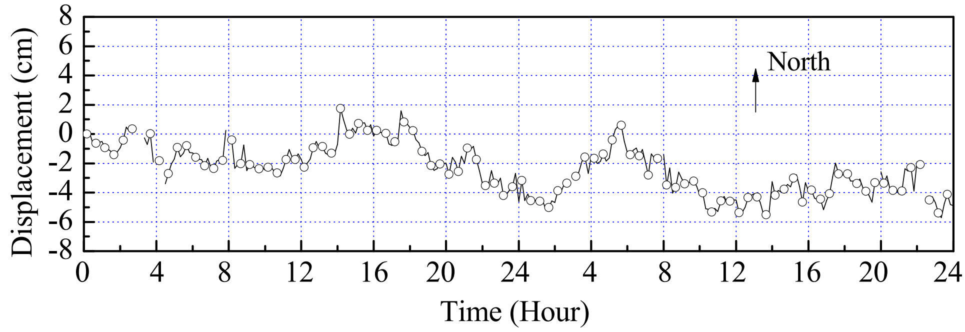

(a) North-South direction

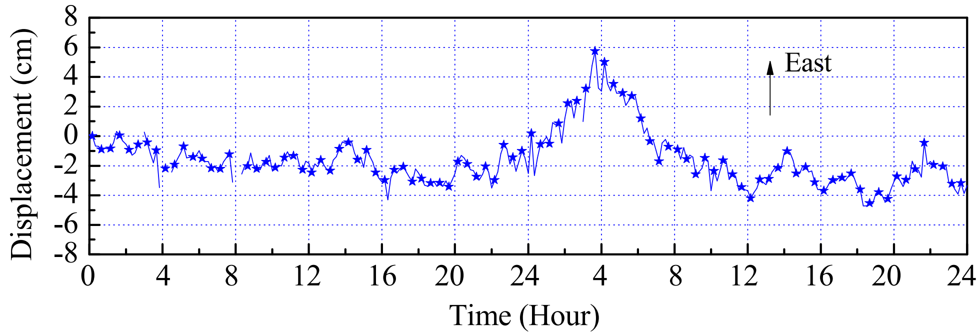

(b) East-west direction

Figure 6.24 Typhoon-induced horizontal displacement at the tower top on 22-23 September 2013

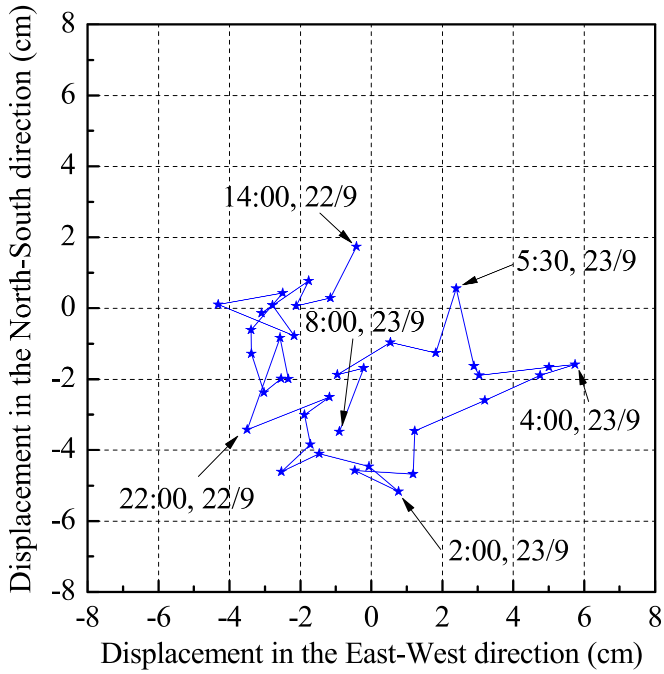

Figure 6.25 Typhoon-induced displacement track at the tower top

Figure 6.26 shows the vertical stress measured at Section 8 for the inner tube from 21 to 23 September 2013. The air temperature of these days is shown in Figure 6.27. On 21 September 2013, it was a sunny day with 4.5 m/s mean wind speed. The variation of the vertical stress of the inner tube in the day was mainly induced by the temperature variation. The pattern is quite similar to the daily stress change under temperature load (see Figure 6.11). Point 4 had the largest variation in stress of about 0.7 MPa. The stress of the inner tube remained stable between 6:00 to 14:00 on 22 September. Subsequently, the stress began to fluctuate significantly from 18:00, which was induced by gust, until 10:00 on 23 September. The largest fluctuation range was about 0.3 MPa. The maximal variation in stress of Point 1 ~ Point 4 during the typhoon period (between 18:00 on 22 to 12:00 on 23 September) was about −0.4 MPa, −0.3 MPa, −0.2 MPa, and 0.5 MPa, respectively. It can be concluded that this stress variation was mainly induced by typhoon, because the air temperature changed

2℃ only during the period (Figure 6.27).

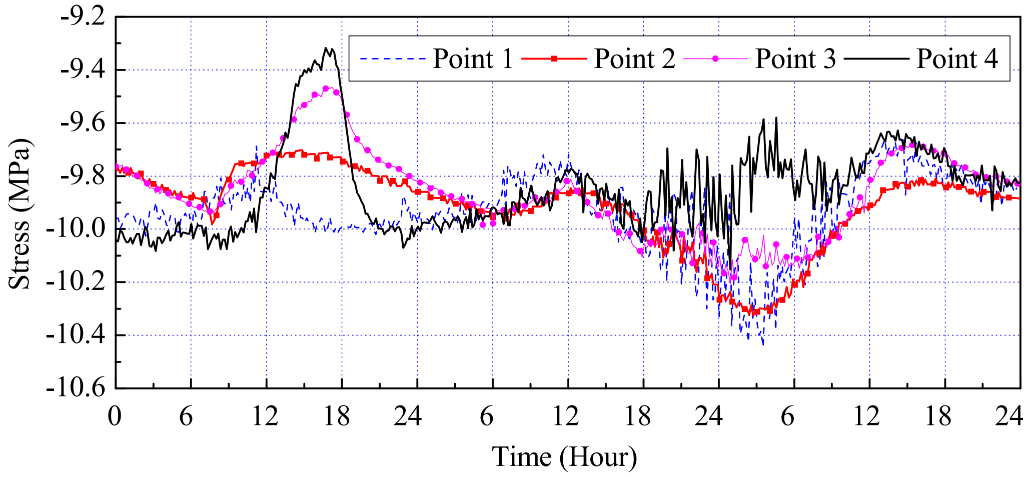

Figure 6.26 Vertical stress of the inner tube on Section 8 during 21-23 September 2013

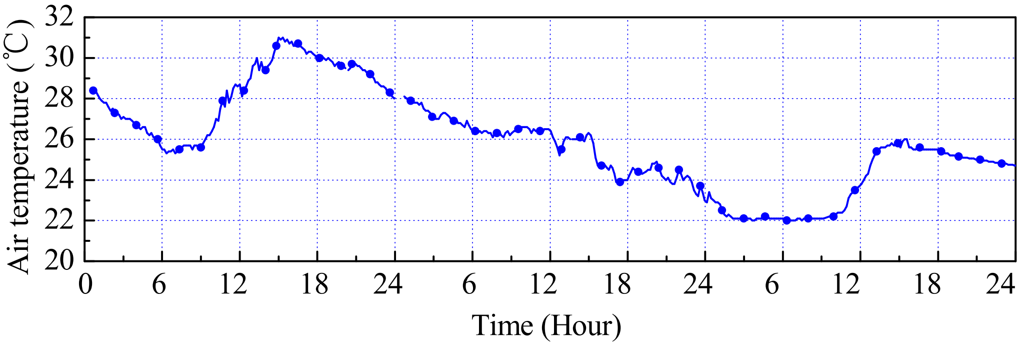

Figure 6.27 Air temperature at the top of the tower during 21-23 September 2013

Changes in the vertical stresses recorded at four monitoring points of the inner tube on different sections of the tower are compared in Figure 6.28 to illustrate the typhoon-induced responses at various heights of the tower. The vertical stresses on Points 1 ~ 3 of all sections decreased, while those at Point 4 increased. The maximum typhoon-induced stress occurred at Section 3, is 0.55 MPa, taking 5.5% of the total stress. Comparison between Figure 6.12 and Figure 6.28 shows that the typhoon-induced vertical stress is fairly smaller than the temperature-induced.

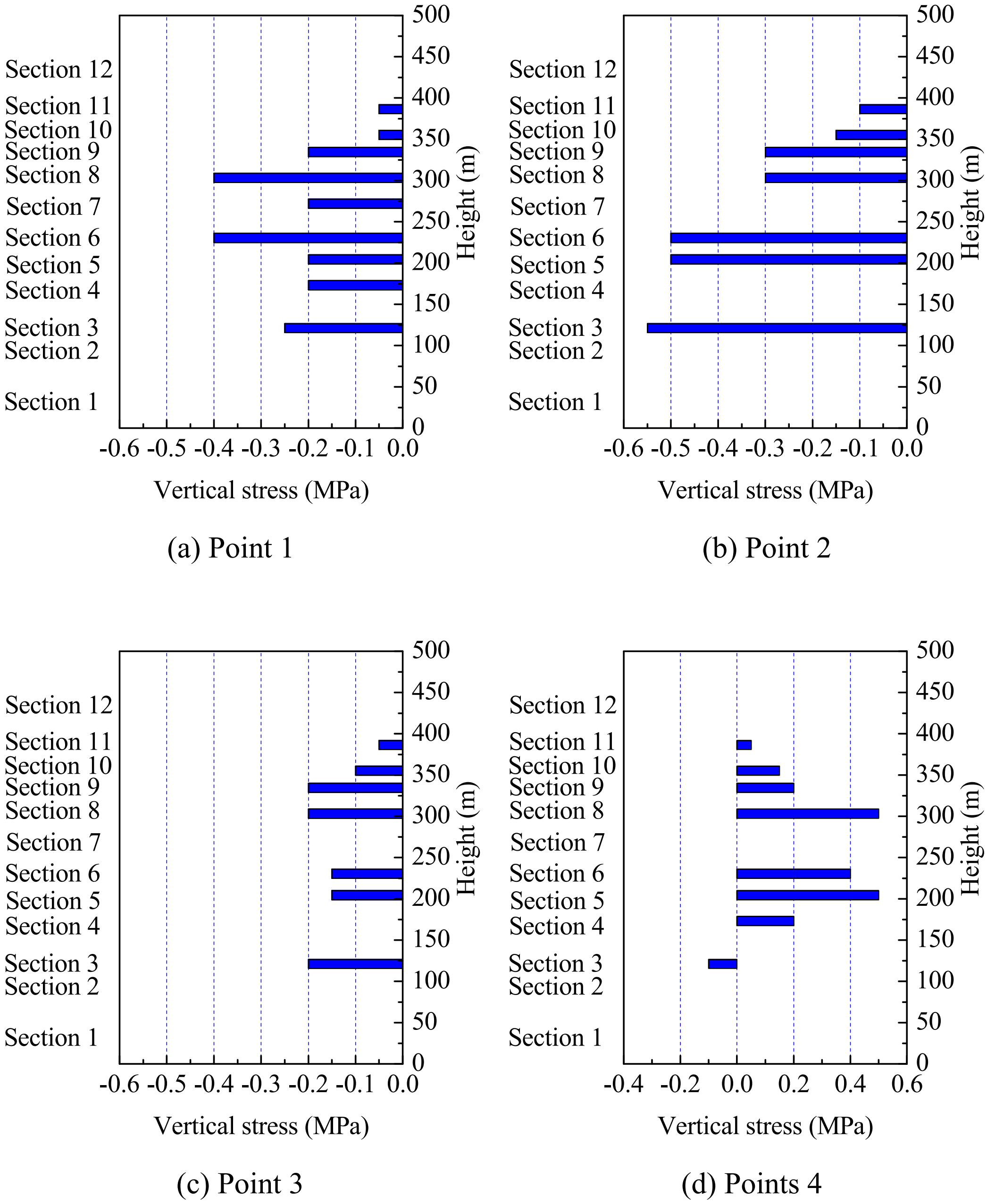

Figure 6.28 Maximal in vertical stresses in different sections during the typhoon period

Sensors on the outer tube were lost from July to October 2013, due to the problem of the data acquisition system. Therefore, the typhoon-induced stress for the outer tube is not available.

6.5 Summary

The temperature-induced displacement and thermal strain/stress are analyzed based on the long-term SHM, and compared with typhoon-induced displacement and strain/stress. Temperature distribution of the structure is input into the global FE model of the tower to calculate its temperature-induced displacement and strain/stress. The simulated results are verified through comparison with the measurements. In particular, the following conclusions can be drawn.

1 The measured temperature-induced yearly displacement at the tower top can reach 31 cm in both east-west and north-south directions. The measured daily horizontal displacement can reach about 21 cm in winter. From summer to winter, the tower leaned towards north-east and the tower top moved about 15 cm. The tower had a larger daily horizontal displacement in the south-north direction in winter than that in other seasons.

2 The temperature-induced vertical stresses of the inner tube decreased (compression increased) as temperature decreased from summer to winter. The compressive stress of the CFT columns on the northeast façade went up, while that on the southwest façade decreased from summer to winter. The temperature-induced stress change at different seasons can reach 25% of the total stress for the inner tube and 11% for the outer tube.

3 The temperature-induced displacement at the tower top was calculated using the FE model. The results show a good agreement with the measured data.

4 The temperature-induced horizontal displacement is much larger than that caused by a strong Typhoon. The stresses caused by a strong typhoon and the daily temperature change are comparable.

CHAPTER SEVEN

CONCLUSIONS AND RECOMMENDATIONS

7.1 Conclusions

This dissertation focused on monitoring the floors' settlement during the construction stage of supertall structures and on monitoring their thermal actions to comprehensively understand the loading environment and structural responses under the real construction and operational conditions. The main contributions and conclusions of this dissertation were summarized as follows.

1. The structural systems and the SHM systems of two test-beds (the Shanghai Tower and the Canton tower) in China were described systematically. The practical monitoring exercise provided the designer, the contractor, and the researcher with valuable real-time data in terms of structural performance.

2. A construction settlement monitoring method that aimed to improve the construction precision was proposed and numerically applied to the Shanghai Tower. This method integrated the Kalman Filtering approach and the FE forward construction stage analysis using a general FE analysis software package MIDAS/GEN. With the Kalman Filtering method, the modelling errors and the measurement noise were filtered out. The updated results considered both the construction load effects and various uncertainties. Consequently, the results were more realistic and accurate for analysing the floors' pre-determined height of supertall buildings. The effect of the error covariance on the Kalman filter results was then investigated. The results showed that the initial state

parameters and the noise covariance may affect the filtering results to some degree. The present method can be extended to the construction control for positioning key components of supertall structures.

3. Based on the five-year field monitoring data using thermal sensors during the service stage of the Canton Tower, the temperature distribution of this supertall structure was studied. In particular, the temperature difference between the inner and outer tubes and the temperature difference between different facades of structure were detailed. In particular, the maximal temperature difference between the outer CFT tube and inner RC tube was –15.0℃ in winter and 8.1℃ in summer for the inner tube enclosed by curtain wall. For segments where both the outer and inner tubes were exposed to the environment, the maximal difference was –6.0℃ in winter and 2.0℃ in summer. In all monitoring sections, temperature of the outer tube was higher than the inner tube in summer and lower in winter. Recommendation for distribution of their difference along the structural height was then proposed. Temperature difference between different facades of the inner tube enclosed by curtain wall was negligible, while difference of segments where the inner tube was exposed to the environment cannot be ignored. In the outer tube, the south facade had higher temperature than the north, and the maximum difference can be 7℃ approximately. The temperature difference profile between different facades was then obtained. The temperature distribution model can be used as the reference in design and construction of similar supertall structures in future.

4. Based on the long-term SHM data, the temperature-induced displacement and thermal strain/stress were analyzed. The measured temperature-induced yearly displacement at the tower top can reach 31 cm in both east-west and north-south directions. The measured daily horizontal displacement can reach about 21 cm in

winter. From summer to winter, the tower leaned towards north-east and the tower top moved 15 cm approximately. The tower had a larger daily horizontal displacement in the south-north direction in winter than that in other seasons. The temperature-induced vertical stresses of the inner tube decreased (compression increased) as temperature decreased from summer to winter. The compressive stress of the CFT columns on the northeast façade went up, while that on the southwest façade decreased from summer to winter. The temperature-induced stress change at different seasons can reach 25% of the total stress for the inner tube and 11% for the outer tube.

5. Temperature distribution of the structure was input into the global FE model of the tower constructed in SAP2000 to simulate its temperature-induced displacement and strain/stress. The simulated results were verified through a comparison with the measurement data. The obtained displacement was in a good agreement with the measurement while the stresses had some discrepancy, which might be due to the inaccuracy of the temperature model used in the FE model. Moreover, many factors would affect the results, both in simulation (such as un-modeled factors and modeling errors) and measurement (sensor quality and accuracy).

6. The temperature-induced displacement and strain/stress were finally compared with typhoon-induced counterparts. The temperature-induced horizontal displacement was much larger than that caused by a strong Typhoon. The stresses caused by a strong typhoon and the daily temperature change were comparable.

7.2 Recommendations for Future Studies

Although progress has been made in this thesis for the construction settlement monitoring and thermal action monitoring of supertall structures, several important issues deserve further studies.

1. The noise covariance in the Kalman Filtering affects the filtering results. Accurately estimating the covariance is challenging and needs further investigation.

2. For the cost consideration, it is infeasible to install sensors on all components of the entire structure. The sensor location optimization should be focused to realize an effective and economical SHM sensory system. Moreover, for such a tube-in-tube structure, the temperature difference between the inner and outer tubes causes significant internal forces of the floors and connection girders. Therefore, temperature and strain sensors can be deployed on these components to investigate the thermal actions on them.

3. The measured temperature data can be used for structural analysis to obtain the temperature-induced deformation and stresses of the Canton Tower. However, the temperature pattern obtained in this thesis may not necessarily represent other structures. The temperature characteristics depend on the structural configuration, construction materials, meteorological condition, and geographical locations. For example, temperature of a steel structure directly exposed to the ambient may reach 40 ~ 50°C in summer in South China. With more in-service monitoring exercises implemented in high-rise structures in the future, the temperature models can be more reliably formulated and codified.

4. The structural responses were mainly induced by the temperature change, the heavy wind, or their combination. In this thesis, the responses induced by the thermal loading only were studied on clear, calm days to eliminate the effect from wind loading. However, it is very hard to measure the typhoon-induced response only by separating it from the thermal effect accurately, because the air temperature is apt to decrease during the typhoon period. Moreover, the thermal effect on the structure will lag behind the change of the air temperature, and interacts with wind effect. Therefore, appropriate separation of the two effects merits further study.

REFERENCES

Abdelrazaq, A., (2011), "Validating the structural behavior and response of Burj Khalifa: synopsis of the full scale structural health monitoring programs", *In Proceeding of 1st Middle East Conference on Smart Monitoring, Assessment and Rehabilitation of Civil Structures*, Dubai, UAE.

Abdelrazaq, A., Kijewski-Correa, T., Song, Y.H., Case, P., Isyumov, N. and Kareem, A., (2005), "Design and full-scale monitoring of the tallest building in Korea: Tower Palace III", *Proceedings of 6th Asia-Pacific Conference on Wind Engineering*, Seoul, Korea.

Aktan, A.E., Bergmeister, K., Bucher, C., Dorfmann, L., Fehling, E., Frey, R.P., Geier, R., Huth, O., Inaudi, D., Maier, J.E., Santa, U., Schwesinger, P., Slowik, V. and Wenzel, H., (2003), "*Monitoring and Safety Evaluation of Existing Concrete Structures*", Ceb-Fib State-of-art report, ISBN 978-2-88394-062-8.

Aktan, A.E., Catbas, F.N., Grimmelsman, K.A. and Tsikos, C.J., (2000), "Issues in infrastructure health monitoring for management", *Journal of Engineering Mechanics*, **126**(7), 711-724.

Alam, S.M.S., Yamada, K. and Baba, S., (1995), "A Kalman filter approach for galloping control of a bridge tower", *Computers & Structures*, **57**(1), 67-79.

ANSYS 10.0, (2005), [Computer software], ANSYS Inc., Southpointe, PA, USA.

Azkune, M., Puente, I. and Insausti, A., (2007), "Effect of ambient temperature on the redistribution of loads during construction of multi-storey concrete structures", *Engineering Structures*, **29**(6), 933-941.

Balendra, T., Ma, Z. and Tan, C.L., (2003), "Design of tall residential buildings in

Singapore for wind effects", *Wind and Structures*, **6**(3), 221-248.

Bast, W.D., McDonnell, T.R., Parker, L. and Shanks, S.P., (2003), "Measured Shortening and its Effects in a Chicago High-rise Building", *In Proceedings of the Third Forensic Engineering Congress*, San Diego, CA, USA.

Branco, F.A. and Mendes, P.A., (1993), "Thermal actions for concrete bridge design", *Journal of Structural Engineering*, **119**(8), 2313-2331.

Branco, F.A., Mendes, P.A. and Mirambell, E., (1992), "Heat of hydration effects in concrete structures", *ACI Materials Journal*, **89**(2), 139-145.

Breuer, P., (2010), "Monitoring the horizontal displacement of slim high towers caused by daily temperature variation and wind impact by application of static and kinematic GPS-Mode: some results", *Proceedings of the 5th World Conference on Structural Control and Monitoring*, Tokyo, Japan.

Breuer, P., Chmielewski, T., Gorski, P. and Konopka, E., (2002), "Application of GPS technology to measurements of displacements of high-rise structures due to weak winds", Journal of Wind Engineering and Industrial Aerodynamics, **90**(3), 223-230.

Breuer, P., Chmielewski, T., Gorski, P., Konopka, E. and Tarczynski, L., (2008), "The Stuttgart TV Tower-displacement of the top caused by the effects of sun and wind", *Engineering Structures*, **30**(10), 2771-2781

Brown, D., (2003). "*Analysis of Wind-induced Acceleration and Pressure Data from an Eight-hundred-foot Tower*", Master's Degree Thesis, University of Notre Dame, USA.

Brown, R.G. and Hwang, P.Y.C., (1992), *Introduction to Random Signals and Applied Kalman Filtering*, second edition, John Wiley & Sons, Inc.

Brownjohn, J.M.W., (2005), "Lateral loading and response for a tall building in the non- seismic doldrums", *Engineering Structures*, **27**(12), 1801-1812.

Brownjohn, J.M.W., (2007), "Structural health monitoring of civil infrastructure", *Philosophical Transactions of the Royal Society A*, **365**(1851), 589-622.

Brownjohn, J.M.W. and Pan, T.C., (2001), "Response of a tall building to weak long distance earthquakes", *Earthquake Engineering and Structural Dynamics*, 30, 709-729.

Brownjohn, J.M.W. and Pan, T.C., (2008), "Identifying loading and response mechanisms from ten years of performance monitoring of a tall building", *Journal of Performance of Constructed Facilities*, **22**(1), 24-34.

Brownjohn, J.M.W. and Pan, T.C., (2009), "Structural health monitoring of a tall building", *Encyclopedia of Structural Health Monitoring*, Boller, C., Chang, F.K. and Fujino, Y. (editors.), John Wiley and Sons, Chichester, UK, chapter 133.

Brownjohn, J.M.W., Pan, T.C. and Cheong, H.K., (1998), "Dynamic response of Republic Plaza, Singapore", *The Structural Engineer*, **76**(11), 221-226.

Casciati, F. and Fuggini, C., (2009), "Engineering vibration monitoring by GPS: long duration records", *Earthquake Engineering and Engineering Vibration*, **8**(3), 459-467.

Çelebi, M., (1993), "Seismic response of eccentrically braced tall building", *Journal of Structural Engineering*, **119**(4), 1188-1205.

Çelebi, M., (2002), "Seismic Instrumentation of Buildings (with Emphasis on Federal Buildings)", An Administration Report, United States Geological Survey, Menlo Park, CA, USA.

Çelebi, M. and Safak, E., (1991), "Seismic response of Transamerica Building. I: data and preliminary analysis", *Journal of Structural Engineering*, **117**(8), 389-2404.

Celebi, M. and Safak, E., (1992), "Seismic response of Pacific Park Plaza. I: data and preliminary analysis", *Journal of Structural Engineering*, **118**(6), 1547-1565.

Celebi, M. and Sanli, A., (2002), "GPS in pioneering dynamic monitoring of long-period structures", *Earthquake Spectra*, **18**(1), 47-61.

Chang, P.C., Flatau, A. and Liu, S.C., (2003), "Health monitoring of civil infrastructure", *Structural Health Monitoring*, **2**(3), 257-267.

Chen, B., Sun, Y.Z., Wang, G.J. and Duan, L.Y., (2014), "Assessment on time-varying thermal loading of engineering structures based on a new solar radiation model", *Mathematical Problems in Engineering*, 2014, Article ID 639867, 15 pages.

Chen, D.H., Ji, B.H., Tang, X.H., Zhang, Y.Q. and Chen, Y.H., (2010), "Sensor network based synchronous lifting technology in bridge reconstruction", *Proceedings of the first International Workshop on Construction, Environment, Transportation,* China, Jiaozuo, 4788-4795.

Chen, W.H., Lu, Z.R., Lin, W., Chen, S.H., Ni, Y.Q., Xia, Y. and Liao, W.Y., (2011), "Theoretical and experimental modal analysis of the Guangzhou New TV Tower", *Engineering Structures*, **33**(12), 3628-3646.

Chen, Y.Q., Huang, D.F., Ding, X.L., Xu, Y.L. and Ko, J.M., (2001), "Measurement of vibrations of tall buildings with GPS: a case study", *Proceedings of the International Symposium on NDE for Health Monitoring and Diagnostics*, SPIE, Newport Beach, California, USA.

Choi, S.W., Kim, Y., Kim, J.M. and Park, H.S., (2013), "Field monitoring of column shortenings in a high-rise building during construction", *Sensors*, **13**(11), 14321-14338.

Computers and Structures Inc., (2009), "*SAP2000 Linear and Nonlinear Static and Dynamic Analysis and Design of Three-Dimensional Structures*", Berkeley, California, USA, version 14.0.

Dalgliesh, W.A. and Rainer, J.H., (1978), "Measurements of wind induced displacements and accelerations of a 57-storey building in Toronto, Canada", *In Proceeding of 3rd Colloquium on Industrial Aerodynamics*, Aachen, part 2, 67-78.

Defraeye, T., Blocken, B. and Carmeliet, J., (2010), "Convective heat transfer coefficients for exterior building surfaces: existing correlations and CFD modelling", *Energy Conversion and Management*, **52**(1), 512-522.

Dilger, W., Dilger, W., Ghali, A., Cheung, M.S. and Beauchamp, J.C., (1981), "Field measurements of Muskwa River Bridge", *Journal of Structural Engineering*, **107**(11), 2147-2161.

Ding, J.M., Zhao, X. and Chao, S., (2010), "The Shanghai Tower", *Conference on Structural Marvels*, Singapore, December 13-14.

Durgin, F.H. and Gilbert, T., (1994), "Data from a full scale study of an 800 foot building in Boston", *Internal Report WBWT-TR-1250*, Wright Brothers Facility, Department of Aeronautics and Astronautics, Massachusetts Institute of Technology.

Elbadry, M.M. and Ghali, A., (1983), "Temperature variations in concrete bridges", *Journal of Structural Engineering*, **109**(10), 2355-2374.

European Committee for Standardization, (2003), "*Eurocode 1: Actions on Structures - Part 1-5: General Actions - Thermal Actions*", EN 1991-1-5:2003, Brussels, Belgium: CEN.

Froli, M., Hariga, N. and Nati, G., (1996), "Longitudinal thermal behavior of a concrete box girder bridge", *Structural Engineering International*, **6**(4), 237-242.

Fan, F., Wang, H.J., Zhi, X.D., Huang, G., Zhu, E.C. and Wang, H., (2013), "Investigation of construction vertical deformation and pre-deformation control for three super high-rise buildings", *Advances in Structural Engineering*, **16**(11), 1885-1898.

Fang, D.P., Zhu, H.Y., Geng, C.D. and Liu, X.L., (2001), "On-site measurements of structural characteristics of reinforced concrete buildings during construction", *ACI Structural Journal*, **98**(2), 157-63.

Fintel, M., Ghosh, S.K. and Iyengar, H., (1987), "*Column Shortening in Tall Buildings-Prediction and Compensation*", Portland Cement Association, Skokie, IL, USA.

Fu, H.C., Ng, S.F. and Cheung, M.S., (1990), "Thermal behavior of composite bridges", *Journal of Structural Engineering*, **116**(12), 3302-3323.

Fu, J.Y., Li, Q.S., Wu, J.R., Xiao, Y.Q. and Song, L.L., (2008), "Field measurements of boundary layer wind characteristics and wind-induced responses of super-tall buildings", *Journal of Wind Engineering and Industrial Aerodynamics*, 96, 1332-1358.

Fuhr, P.L., Huston, D.R., Kajenski, P.J. and Ambrose, T.P., (1992), "Performance and health monitoring of the Stafford Medical Building using embedded sensors", *Smart Materials and Structures*, **1**(1), 63-68.

GB 50009-2012, (2012), "*Load Code for the Design of Building Structures*", Ministry of Housing and Urban-Rural Development of the People's Republic of

China, China Architecture and Building Press, Beijing, China.

GB 50010-2010, (2010), "*Code for Design of Concrete Structures*", Ministry of Housing and Urban-Rural Development of the People's Republic of China, China Architecture and Building Press, Beijing, China.

Gekokn 4200, http://www.geokon.com/content/datasheets/4200_Series_Strain_ Gages. pdf .

Gekokn 4000, http://www.geokon.com/content/datasheets/4000_Strain_Gage.pdf .

Giraldo, D.F., Dyke, S.J. and Caicedo, J.M., (2006), "Damage detection accommodating varying environmental conditions", *Structural Health Monitoring*, **5**(2), 155-172.

Glisic, B., Inaudi, D., Lau, J.M. and Fong, C.C., (2013), "Ten-year monitoring of high-rise building columns using long-gauge fiber optic sensors", *Smart Materials and Structures*, **22**(5), 15.

Huang, M.J. and Shakal, A.F., (2001), "Structure instrumentation in the California strong motion instrumentation program", *Strong Motion Instrumentation for Civil Engineering Structures*, 373, 17-31.

Hudson, D.E., (1977), "Dynamic tests of full-scale structures", *Journal of the Engineering Mechanics Division*, **103**(6), 1141-1157.

Howell, J.R., Siegel, R. and Menguc, M.P., (2011), "*Thermal Radiation Heat Transfer, Fifth Edition*", CRC Press, Taylor & Francis Group.

Jacobson, M.Z., (2005), "*Fundamentals of Atmospheric Modeling*", second edited, Cambridge University Press.

Jayasinghe, M.T.R. and Jayasena, W.M.V.P.K., (2004), "Effect of axial shortening of columns on design and construction of tall reinforced concrete buildings", *Practice Periodical on Structural Design and Construction*, **9**(2), 70-78.

Jeary, A.P. and Ellis, B.R., (1981), "Vibration tests on structures at varied amplitudes", *In Proceedings Specialty Conference on Dynamic Response of Structures: Experimentation, Observation, Prediction and Control*, Atlanta, Georgia, 281-294.

Jin, X.F., Fan, F. and Shen, S.Z., (2008), "Effect of non-uniform temperature field under sunshine on the structure supporting the reflector of a large radio telescope-FAST, *China Civil Engineering Journal*, **41**(11), 73-77. (in Chinese).

Kalman, R.E., (1960), "A new approach to linear filtering and prediction problems", *Journal of Basic Engineering*, **82**(1), 35-46.

Kennedy, J. and Soliman, M., (1987), "Temperature distributions in composite bridges", *Journal of Structural Engineering*, **113**(3), 65-78.

Khan, F.R. and Nassetta, A.F., (1970), "Temperature effects on tall steel framed buildings Part 3 - Design considerations", *National Engineering Conference AISC*, Pittsburgh, USA, **7**(4), 121-131.

Kijewski-Correa, T. and Kareem, A., (2003), "The Chicago monitoring project: a fusion of information technologies and advanced sensing for civil infrastructure", *Structural Health Monitoring and Intelligent Infrastructure*, 2, 1003-1010.

Kijewski-Correa, T., Kareem, A. and Kochly, M., (2006a), "Experimental verification and full-scale deployment of Global Positioning Systems to monitor the dynamic response of tall buildings", *Journal of Structural Engineering*, **132**(8), 1242-1253.

Kijewski-Correa. T., Kilpatrick, J., Bashor, R., Kwon, D.K., Young, B.S., Sinn, R.C., Galsworthy, J., Morrish, D., Isyumov, N. and Kareem, A., (2005), "Full-scale validation of the wind-induced response of tall buildings: updated findings from the Chicago monitoring project", *Structures Congress*, New York, 1-7.

Kijewski-Correa, T., Kilpatrick, J., Kareem, A., Kwon, D.K., Bashor, R., Kochly, M., Young, B.S., Abdelrazaq, A., Galsworthy, J., Isyumov, N., Morrish, D., Sinn, R.C., Baker, W.F., (2006b), "Validating wind-induced response of tall buildings: synopsis of the Chicago full-scale monitoring program", *Journal of Structural Engineering*, **132**(10), 1509-1523.

Kijewski-Correa, T. and Pirnia, J.D., (2007), "Dynamic behavior of tall buildings under wind: insights from full-scale monitoring", *The Structural Design of Tall and Special Buildings*, 16, 471-486.

Ko, J.M. and Ni, Y.Q., (2005), "Technology developments in structural health monitoring of large-scale bridges", *Engineering Structures*, **27**(12), 1715-1725.

Kohler, M.D., Heaton, T.H. and Bradford, S.C., (2007), "Propagating waves in the steel, moment-frame factor building recorded during earthquakes", *Bulletin of the Seismological Society of America*, **97**(4), 1334-1345.

Kreith, F., (1973), "*Principles of Heat Transfer (3rd ed.)*", Intext Educational Publishers, New York, N.Y., USA.

Larson, K.M., (2009), "GPS seismology", Journal of Geodesy, 83, 227-233.

Li, D.N., Maes, M.A. and Dilger, W.H., (2004a), "Thermal design criteria for deep prestressed concrete girders based on data from Confederation Bridge", *Canadian Journal of Civil Engineering*, **31**(5), 813-825.

Li, D.S., Ren, L., Li, H.N. and Song, G.B., (2012), "Structural health monitoring of a tall building during construction with fiber bragg grating sensors", *International Journal of Distributed Sensor Networks*, **2012**, 1-10.

Li, H., Yang, B., Zhang, Q.L. and Xiong, H.B., (2014), "Numerical simulation and monitoring of dynamic property of Shanghai Tower under construction", *Journal of Central South University (Science and Technology)*, **45**(7), 2369-2377.

Li, H., Zhang, D.Y., Bao, Y.Q. and Zhou, F., (2009), "A numerical investigation of temperature effect on modal parameters of the China National Aquatics Center", *The 7th International Workshop on Structural Health Monitoring*, Stanford University, USA.

Li, H.N., Yi, T.H., Yi, X.D. and Wang, G.X., (2007a), "Measurement and analysis of wind-induced response of tall building based on GPS technology", *Advances in Structural Engineering*, **10**(1), 83-93.

Li, Q.S., Fang, J.Q., Jeary, A.P., Wong, C.K. and Liu, D.K., (2000), "Evaluation of wind effects on a supertall building based on full-scale measurements", *Earthquake Engineering and Structural Dynamics*, 29, 1845-1862.

Li, Q.S., Fu, J.Y., Xiao, Y.Q., Li, Z.N., Ni, Z.H., Xie, Z.N. and Gu, M., (2006a), "Wind tunnel and full-scale study of wind effects on China's tallest building", *Engineering Structures*, 28, 1745-1758.

Li, Q.S. and Wu, J.R., (2007), "Time-frequency analysis of typhoon effects on a 79-storey tall building", *Journal of Wind Engineering and Industrial Aerodynamics*, **95**(12), 1648-1666.

Li, Q.S., Wu, J.R., Liang, S.G., Xiao, Y.Q. and Wong, C.K., (2004b), "Full-scale measurements and numerical evaluation of wind induced vibration of a 63-story reinforced concrete tall building", *Engineering Structures*, **26**(12), 1779-1794.

Li, Q.S., Xiao, Y.Q., Fu, J.Y. and Li, Z.N., (2007b), "Full-scale measurements of wind effects on Jin Mao building", *Journal of Wind Engineering and Industrial*

Aerodynamics, **95**(6), 445-466.

Li, Q.S., Xiao, Y.Q., Wong, C.K. and Jeary, A.P., (2004c), "Field measurements of typhoon effects on a super tall building", *Engineering Structures*, 26, 233-244.

Li, Q.S., Yang, K., Wong, C.K. and Jeary, A.P., (2003), "The effect of amplitude-dependent damping on wind-induced vibrations of a super tall building", *Journal of Wind Engineering and Industrial Aerodynamics*, 91, 1175-1198.

Li, X.J., Ge, L.L., Ambikairajah, E., Rizos, C., Tamura, Y. and Yoshida, A., (2006b), "Full-scale structural monitoring using an integrated GPS and accelerometer system", *GPS Solutions*, **10**(4), 233-247.

Lienhard, J.H. and Lienhard, J.H., (2003), "*A Heat Transfer Textbook*", third edited, Phlogiston Press, Cambridge, Massachusetts, USA.

Lin, C.C., Wang, C.E., Wu, H.W. and Wang, J.F., (2005), "On-line building damage assessment based on earthquake records", *Smart Materials and Structures*, **14**(3), 137-153.

Lin, Y.P., (1983), "The application of Kalman filter at cable-stayed bridge construction", *Journal of Civil Engineering*, **6**(3), 7-14.

Littler, J.D. and Ellis, B.R., (1990), "Interim findings from full-scale measurements at Hume Point", *Journal of Wind Engineering and Industrial Aerodynamics*, 36, 1181-1190.

Liu, Z.Y., (2010), "Thermal Research on Concrete Filled Steel Tubular Truss Arch", Fuzhou University, PhD thesis. (in Chinese).

Lovse, J.W., Teskey, W.F., Lachapelle, G. and Cannon, M.E., (1995), "Dynamic deformation monitoring of tall structure using GPS technology", *Journal of*

Survey Engineering, **121**(1), 35-40.

Lynch, J.P., (2005), "Design of a wireless active sensing unit for localized structural health monitoring", *Structural Control Health Monitoring*, **12**(3-4), 405-423.

Lynch J.P., Law K.H., Kiremidjian A.S., Carryer E., Farrar C.R., Sohn H., Allen, D.W., Nadler, B. and Wait, J.R., (2004), "Design and performance validation of a wireless sensing unit for structural monitoring applications", *Structural Engineering and Mechanics*, **17**(3-4), 393-408.

Ma, Q.F., Fang, R.S. and Xiang, L.C., (1986), "Handbook of Thermo Physical Properties of Material", Beijing: Agricultural Press. (in Chinese).

Malla, R., Nash, W. and Lardner, T., (1988), "Thermal effects on very large space structures", *Journal of Aerospace Engineering*, **1**(3), 171-188.

McLaughlin, E.R., (1970), "Temperature effects on tall steel framed buildings Part 1 - Response of steel columns to temperature exposure", *National Engineering Conference AISC*, Pittsburgh, USA, **7**(4), 105-109.

MIDAS GEN, (2012), "*Analysis Manual for MIDAS/GEN*", MIDAS Information Technology Co. Ltd., Seoul, Korea.

Mirambell, E., Aguado, A., Mendes, P.A. and Branco, F.A., (1991), "Design temperature differences for concrete bridges", *Structural Engineering International*, **1**(3), 36-40.

Mita, A., (1999), "Emerging needs in Japan for health monitoring technologies in civil and building structures", *In Proceeding of 2nd International Workshop on Structural Health Monitoring*, Stanford University.

Moragaspitiya, P., Thambiratnam, D., Perera, N. and Chan, T., (2010), "A numerical method to quantify differential axial shortening in concrete buildings", *Engineering Structures*, **32**(8), 2310-2317.

Nayeri, R.D., Masri, S.F., Ghanem, R.G. and Nigbor, R.L., (2008), "A novel approach for the structural identification and monitoring of a full-scale 17-story building based on ambient vibration measurements", *Smart Materials and Structures*, **17**(2), 1-19.

Ni, Y.Q., Hua, X.G., Wong, K.Y. and Ko, J.M., (2007), "Assessment of bridge expansion joints using long-term displacement and temperature measurement", *Journal of Performance of Constructed Facilities*, **21**(2), 143-151.

Ni, Y.Q. and Li, W.R., (2013), "*Seismic Response Monitoring and Analysis of a Super-Tall Structure Instrumented with SHM System*", Chapter 11 of the book: Earthquakes and Health Monitoring of Civil Structures, edited by Garevski, M., Springer-Verlag, Heidelberg, Germany, 269-286.

Ni, Y.Q., Li, W.R. and Ko, J.M., (2012), "Monitoring of dynamic responses of a super-tall structure during earthquakes", *Proceedings of the International Conference on Earthquake Research Challenges in the 21st Century*, Harbin, China.

Ni, Y.Q. and Wong, K.Y., (2012), "Integrating bridge structural health monitoring and condition-based maintenance management", *Proceedings of the 4th International Workshop on Civil Structural Health Monitoring*, 6-8 November 2012, Berlin, Germany.

Ni, Y.Q., Wong, K.Y. and Xia, Y., (2011a), "Health checks through landmark bridges to sky-high structures", *Advances in Structural Engineering*, **14**(1), 103-119

Ni, Y.Q., Xia, Y., Chen, W.H., Lu, Z.R., Liao, W.Y. and Ko, J.M., (2009a), "Monitoring of wind properties and dynamic responses of a supertall structure during typhoon periods", *Proceedings of the 4th International Conference on Structural Health Monitoring and Intelligent Infrastructure*, Zurich, Switzerland.

Ni, Y.Q., Xia, Y., Liao, W.Y. and Ko, J.M., (2009b), "Technology innovation in developing the structural health monitoring system for Guangzhou New TV Tower", *Structural Control and Health Monitoring*, **16**(1), 73-98

Ni, Y.Q., Xia, Y., Liao, W.Y. and Zhang, P., (2008), "Development of a structural health monitoring system for Guangzhou New TV Tower", *Advances in Science and Technology*, 56, 414-419.

Ni, Y.Q., Zhang, P., Ye, X.W., Lin, K.C. and Liao, W.Y., (2011b), "Modeling of temperature distribution in a reinforced concrete supertall structure based on structural health monitoring data", *Computers and Concrete*, **8**(3), 293-309.

Nickitopoulou, A., Protopsalti, K. and Stiros, S., (2006), "Monitoring dynamic and quasi-static deformations of large flexible engineering structures with GPS: accuracy, limitations and promises", *Engineering Structures*, **28**(10), 1471-1482.

Nunez, T.R. and Boroschek, R.L., (2010), "Modal properties of a high rise building under construction", *Proceedings of the 28th International Modal Analysis Conference*, February 1-4, 2010, Jacksonville, Florida, USA. Paper No. 242.

Odelson, B.J., Rajamani, M.R. and Rawlings, J.B., (2006), "A new autocovariance leasts-quares method for estimating noise covariances", *Automatica*, **42**(2), 303-308.

Ogaja, C., Rizos, C. and Han, S.W., (2000), "Is GPS good enough for monitoring the dynamics of high-rise buildings?", *Proceedings of the 2nd Trans Tasman Surveyors Congress*, Queenstown, New Zealand.

Ogaja, C., Rizos, C., Wang, J.L. and Brownjohn, J., (2001), "GPS and building monitoring case study: Republic Plaza Building, Singapore", *Proceedings of the International Symposium on Kinematic Systems in Geodesy, Geomatics and Navigation*, Banff, Canada.

Ogaja, C., Wang, J.J. and Rizos, C., (2003), "Detection of wind-induced response by wavelet transformed GPS solutions", *Journal of Surveying Engineering*, **129**(3), 99-104.

Ohkuma, T., Marukawa, H., Niihori, Y. and Kato, N., (1991), "Full-scale measurement of wind pressures and response accelerations of a high-rise building", *Journal of Wind Engineering and Industrial Aerodynamics*, **38**(2-3), 185-196.

Ohtake, K., Mataki, Y., Ohkuma, T., Kanda, J. and Kitamura, H., (1992), "Full-scale measurements of wind actions on Chiba Port Tower", *Journal of Wind Engineering and Industrial Aerodynamics*, **43**(1-3), 2225-2236.

Ou, J.P. and Li, H., (2010), "Structural health monitoring in mainland China: review and future trends", *Structural Health Monitoring*, 9, 219-231.

Pan, T.C., Brownjohn, J.M.W. and You, X.T., (2004), "Correlating measured and simulated dynamic responses of a tall building to long-distance earthquakes", *Earthquake Engineering and Structural Dynamics*, **33**(5), 611-632.

Park, H.S., (2003), "Optimal compensation of differential column shortening in high-rise buildings", *The Structural Design of Tall Special Buildings*, **12**(1), 49-66.

Park, S.W., Choi, S.W. and Park, H.S., (2013), "Moving average correction method for compensation of differential column shortening in high-rise buildings", *The Structural Design of Tall Special Buildings*, **22**(9), 718-728.

Park, H.S., Hong, K.P. and Seo, J.H., (2002), "Drift design of steel-frame shear-wall systems for tall buildings", *The Structural Design of Tall Buildings*, **11**(1), 35-49.

Park, H.S., Shon, H.G., Kim, I.S. and Park, J.H., (2008), "Application of GPS to monitoring of wind-induced responses of high-rise buildings", Structural Design of Tall Special Buildings, **17**(1), 117-32

Pines, D.J. and Aktan, A.E., (2002), "Status of structural health monitoring of long-span bridges in the United States", *Progress in Structural Engineering and Materials*, **4**(4), 372-80.

Pirner, M. and Fischer, O., (1999), "Long-time observation of wind and temperature effects on TV towers", *Journal of Wind Engineering and Industrial Aerodynamics*, **79**(1-2), 1-9.

Priestley, M.J.N., (1976), "Design temperature gradients for concrete bridges", *New Zealand Engineering*, **31**(9), 213-219.

Qian, Y.Y. and Mita, A., (2006), "Time series-based damage evaluation algorithm with application to building structures", *Proceedings of the 1st Asia-Pacific Workshop on Structural Health Monitoring*, Yokohama, Japan.

Quan, Y., Gu, M. and Tamura, Y., (2005), "Experimental evaluation of aerodynamic damping of square super high-rise buildings", *Wind and Structures*, **8**(5), 309-324.

Rajamani, M.R. and Rawlings, J.B., (2009), "Estimation of the disturbance structure from data using semidefinite programming and optimal weighting", *Automatica*, **45**(1), 142-148.

Rao, S.S., (1999), "*The Finite Element Method in Engineering*", Butterworth - Heinemann, Boston.

Rohsenow, W.M., Hartnett, J.P. and Ganic, E.N., (1985), "Handbook of Heat Transfer Applications", New York, McGraw-Hill.

Salawu, O.S., (1997), "Detection of structural damage through changes in frequency: a review", *Engineering Structures*, **19**(9), 718-723.

Safak, E., (1993), "Response of a 42-storey steel-frame building to the Ms = 7.1 Loma Prieta earthquake", *Engineering Structures*, **15**(6), 403-422.

Safak, E. and Celebi, M., (1992), "Recorded seismic response of Pacific Park Plaza. II: system identification", *Journal of Structural Engineering*, **118**(6), 1566-1589.

Satake, N. and Yokota, H., (1996), "Evaluation of vibration properties of high-rise steel buildings using data of vibration tests and earthquake observations", *Journal of Wind Engineering and Industrial Aerodynamics*, **59**(2-3), 265-282.

Seco, A., Tirapu, F., Ramirez, F., Garcia, B. and Cabrejas, J., (2007), "Assessing building displacement with GPS", *Building and Environment*, **42**(1), 393-399.

Sekihara K., (1985), "*Solar Energy Utilization Handbook*", Matsuo Y. (Ed.), Japan Solar Energy Society, Tokyo, Part 1, Chapter 1, 7–9.

Shahawy, M. A. and Arockiasamy, M., (1996), "Field instrumentation to study the time-dependent behavior in sunshine skyway bridge", *Journal of Bridge Engineering*, **1**(2), 76-86.

Shi, C., Lou, Y., Zhang, H., Zhao, Q., Geng, J.,Wang, R., Fang, R. and Liu, J., (2010), "Seismic deformation of the M_w 8.0 Wenchuan earthquake from high-rate GPS observations", Advances in Space Research, **46**(2), 228-235.

Skolnik, D., Lei, Y., Yu, E. and Wallace, J.W., (2006), "Identification, model updating, and response prediction of an instrumented 15-story steel-frame building", *Earthquake Spectra*, **22**(3), 781-802.

Smith, B.S. and Coull, A., (1991), "*Tall Building Structures: Analysis and Design*", Wiley, New York, USA.

SoDa, Solar Energy Services for Professionals, (2014), "Typical values for clear skies: Optical turbidity (Linke turbidity factor)", Retrieved from: http://www.soda-is.com/eng/services/climat_free_eng.php#lin.

Sohn, H., Farrar, C.R., Hemez, F.M., Shunk, D.D., Stinemates, D.W., Nadler, B.R. and Czarnecki, J.J., (2004), "*A Review of Structural Health Monitoring Literature Form 1996-2001*", Los Alamos National Laboratory report LA-13976-MS.

Spencer Jr., B.F., Ruiz-Sandoval, M.E. and Kurata, N., (2004), "Smart sensory technology: opportunities and challenges", *Structural Control and Health Monitoring*, **11**(4), 349-368.

Stivaros, P.C. and Halvorsen, G.T., (1990), "Shoring/reshoring operations for multistory buildings", *ACI Structural Journal*, **87**(5), 589-96.

Su, J.Z., Xia, Y., Chen, L., Zhao, X., Zhang, Q.L., Xu, Y.L., Ding, J.M., Xiong, H.B., Ma, R.J., Lv, X.L. and Chen, A.R., (2013), "Long-term structural performance monitoring system for the Shanghai Tower", *Journal of Civil Structural Health Monitoring*, **3**(1), 49-61.

Sumitro, S. and Wang, M.L., (2005), "Sustainable structural health monitoring system", *Structural Control and Health Monitoring*, **12**(3-4), 445-467.

Sun, H.H., Zhao, X., Li, X.P., Ding, J.M. and Zhou Y., (2011), "Performance analysis of basement fin wall of the Shanghai tower based on the interaction between pile-raft foundation and superstructure", *Procedia Engineering*, 14, 1367-1375.

Tamura, Y., Kohsaka, R., Nakamura, O., Miyashita, K. and Modi, V.J., (1996), “Wind-induced responses of an airport tower — efficiency of tuned liquid damper”, *Journal of Wind Engineering and Industrial Aerodynamics*, **65**(1-3), 121-131.

Tamura, Y., Matsui, M., Pagnini, L.C., Ishibashi, R. and Yoshida, A., (2002), “Measurement of wind-induced response of buildings using RTK-GPS”, *Journal of Wind Engineering and Industrial Aerodynamics*, **90**(12-15), 1783-1793.

Teng, J., Lu, W., Cui, Y. and Zhang, R.G., (2014), “Temperature and displacement monitoring to steel roof construction of Shenzhen Bay Stadium”, *International Journal of Structural Stability and Dynamics*, 16, 1-22.

Tong, M., Tham, L.G., Au, F.T.K. and Lee, P.K.K., (2001), “Numerical modelling for temperature distribution in steel bridges”, *Computers & Structures*, **79**(6), 583-593.

Van der Auweraer, H. and Peeters, B., (2003), “International research projects on structural health monitoring: an overview”, *Structural Health Monitoring*, **2**(4), 341-358.

Welch, G. and Bishop, G., (2001), “An Introduction to the Kalman Filter”, SIGGRAPH Course.

West, H.H. and Kar, A.K., (1970), “Temperature effects on tall steel framed buildings Part 2 - Structural analysis”, *National Engineering Conference AISC*, Pittsburgh, USA, **7**(4), 110-120.

Whitaker, S., (1977), “*Fundamental Principles of Heat Transfer*”, New York: Pergamon Press.

Wong, K.Y., (2004), “Instrumentation and health monitoring of cable-supported bridges”, *Structural Control and Health Monitoring*, **11**(2), 91-124.

Wong, K.Y., (2007), “Design of a structural health monitoring system for long-span bridges”, *Structure and Infrastructure Engineering*, **3**(2), 169-185.

Wong, K.Y. and Ni, Y.Q., (2009), “Modular architecture of structural health monitoring system for cable-supported bridges”, Chapter 123 of the book: *Encyclopedia of Structural Health Monitoring*, edited by Boller, C., Chang, F.K. and Fujino, Y., John Wiley & Sons, Chichester, UK, 2089-2105.

Wu, Z.S., (2003), “Structural health monitoring and intelligent infrastructures in Japan”, *Proceedings of the 1st International Conference on Structural Health Monitoring and Intelligent Infrastructure*, 153-167.

Xia, Y., Chen, B., Zhou, X.Q. and Xu, Y.L., (2013), “Field monitoring and numerical analysis of Tsing Ma suspension bridge temperature behavior”, *Structural Control and Health Monitoring*, **20**(4), 560-575.

Xia, Y., Hao, H., Zanardo, G. and Deeks, A. J. (2006), “Long term vibration monitoring of a RC slab: temperature and humidity effect”, *Engineering Structures*, **28**(3), 441-452

Xia, Y., Ni, Y.Q., Zhang, P, Liao, W.Y. and Ko, J.M., (2011a), “Stress development of a super-tall structure during construction: field monitoring and numerical analysis”, *Computer - Aided Civil and Infrastructure Engineering*, **26**(7), 542-559.

Xia, Y., Xu, Y. L., Wei, Z. L., Zhu, H. P. and Zhou, X. Q., (2011b), “Variation of structural vibration characteristics versus non-uniform temperature distribution”, *Engineering Structures*, **33**(1), 146-153.

Xia, Y., Zhang, P., Ni, Y. Q. and Zhu, H.P., (2014), “Deformation monitoring of a super-tall structure using real-time strain data”, *Engineering Structures*, 67, 29-38.

Xie, Z.N. and Gu, M., (2009), "Across-wind dynamic response of high-rise building under wind action with interference effects from one and two tall buildings", *The Structural Design of Tall Special Buildings*, **18**(1), 37-57.

Xu, Y.L. and Xia, Y., (2012), "*Structural Health Monitoring of Long-Span Suspension Bridges*", Spon Press, London.

Yang, W. J., Lee, J. H. and Yi, W. H., (2012), "Development of the neural network algorithm for the prediction of column shortening in high-rise buildings", *Advances in Structural Engineering*, **15**(3), 509-524.

Ye, X.W., Ni, Y.Q. and Xia, Y.X., (2012), "Distributed strain sensor networks for in-construction monitoring and safety evaluation of a high-rise building", *International Journal of Distributed Sensor Networks*, 2012, 1-13.

Yi, T.H. and Li, H.N., (2009), "*Structural Health Monitoring Based on GPS Technology*", China Architecture & Building Press: Beijing, 2009.

Yi, T.H., Li, H.N. and Gu, M., (2010), "Full-scale measurements of dynamic response of suspension bridge subjected to environmental loads using GPS technology", *Science China Technological Sciences*, **53**(2), 469-479.

Yi, T.H., Li, H.N. and Gu, M., (2011), "Optimal sensor placement for structural health monitoring based on multiple optimization strategies", *The Structural Design of Tall and Special Buildings*, **20**(7), 881-900.

Yi, T.H., Li, H.N. and Gu, M., (2013a), "Experimental assessment of high-rate GPS receivers for deformation monitoring of bridge", *Measurement*, **46**(1), 420-432.

Yi, T.H., Li, H.N. and Gu, M., (2013b), "Recent research and applications of GPS-based monitoring technology for high-rise structures", *Structural Control* *and Health Monitoring*, **20**(5), 649-670.

Yi, T.H., Li, H.N. and Zhao, X.Y. (2012), "Noise smoothing for structural vibration test signals using an improved wavelet thresholding technique", *Sensors*, **12**(8), 11205-11220.

Yoshida, A., Tamura, Y. and Ishibashi (2003), "Measurement of wind-induced response of buildings using RTK-GPS and integrity monitoring", *Journal of structural Construction Engineering*, 571, 39-44.

Yuen, K.V. and Kuok, S.C., (2010), "Ambient interference in long-term monitoring of buildings", *Engineering Structures*, **32**(8), 2379-2386.

Zhang, B., Wang, T.S. and Li, S.S., (2011), "The research of monitoring model for bridge running", *Proceedings of the International Conference on System Science, Engineering Design and Manufacturing Informatization*, 2, 150-153.

Zhang, P., Xia, Y. and Ni, Y.Q., (2012), "Prediction of temperature induced deformation of a supertall structure using structural health monitoring data", *Proceedings of the 6th European Workshop on Structural Health Monitoring*, 3-6 July 2012, Dresden, Germany, 879-885.

Zhang, Q.L., (2013), "Structural performance monitoring system for the Tianjin Goldin Finance 117 Tower", *The ISHMII Monitor*, **8**(2), 15-16.

Zhang, Q.L., Yang, B., Liu, T., Li, H. and Lv, J., (2015), "Structural health monitoring of Shanghai Tower considering time-dependent effects", *International Journal of High-Rise Buildings*, **4**(1), 39-44.

Zhao, X., Ding, J.M. and Sun. H.H., (2011), "Structural design of shanghai tower for wind loads", *Procedia Engineering*, 14, 1759-1767.

Zheng, Y.M., Zhang, P.P., Zhao, X. and Zheng, Y., (2011), "Analysis on sunshine temperature difference effect of Shanghai Center", *Building Structure*, **41**(5), 28-32. (in Chinese).

Zhou, G.D. and Yi, T.H., (2013), "Thermal load in large-scale bridges: a state-of-the-art review", *International Journal of Distributed Sensor Networks*, **2013**, 1-17.

Zhou, H.F., Ni, Y.Q. and Ko, J.M., (2010) "Constructing input to neural networks for modeling temperature-caused modal variability: mean temperatures, effective temperatures, and principal components of temperatures", *Engineering Structures*, **32**(6), 1747-1759.

Zuk, W., (1965), "Thermal behavior of composite bridges - insulated and uninsulated", *Highway Research Record*, 76, 231-253.